# Nonlinear Effects in Ultralong Semiconductor Optical Amplifiers for Optical Communications: Physics and Applications

vorgelegt von
Diplom-Ingenieur
Patrick Runge

von der Fakultät IV für Elektrotechnik und Informatik
der Technischen Universität Berlin
zur Erlangung des akademischen Grades

Doktor der Ingenieurwissenschaften

Dr.-Ing.

genehmigte Dissertation

Promotionsausschuss:

| | |
|---|---|
| Vorsitzender: | Prof. Dr.-Ing. habil. G. Mönich |
| Berichter: | Prof. Dr.-Ing. K. Petermann |
| Berichter: | Prof. Dr. sc. nat. J. Leuthold |

Tag der wissenschaftlichen Aussprache: 19. Oktober 2010

Berlin 2010

D 83

# Contents

**1. Introduction** **1**
1.1. SOAs in Optical Communications . . . 1
1.2. Review on SOA Modeling Approaches . . . 2
1.3. Motivation for This Work . . . 3
1.3.1. UL-SOAs for Wavelength Conversion With Signal Regeneration . . . 3
1.3.2. Supercontinuum Generation with UL-SOAs . . . 4

**2. Optical Properties of UL-SOAs** **6**
2.1. Semiconductors Basics . . . 6
2.1.1. Interband Effects . . . 8
2.1.2. Intraband Effects . . . 10
2.1.3. Gain Dynamics . . . 11
2.1.4. Kramers-Kronig Relation . . . 13
2.2. Optical Wave Propagation in UL-SOAs . . . 15
2.3. Chromatic Dispersion in UL-SOAs . . . 16
2.3.1. Waveguide Dispersion . . . 17
2.3.2. Material Dispersion . . . 17
2.3.3. Total Chromatic Dispersion . . . 18
2.3.4. Dependence on Carrier Density and Temperature . . . 18
2.3.5. Consequences for Applications . . . 20

**3. Nonlinear Optics in UL-SOAs** **22**
3.1. Time-Domain Modelling of UL-SOAs . . . 22
3.1.1. Modelling Concept . . . 22
3.1.2. Spectral Gain Approximation . . . 24
3.2. Properties of UL-SOAs . . . 25
3.3. Nonlinear Optics in UL-SOAs . . . 26
3.3.1. Static Effects . . . 27
3.3.2. Dynamic Effects . . . 27
3.4. Device Optimisation . . . 32

**4. High-Speed Wavelength Conversion With Signal Regeneration in UL-SOAs** **34**
4.1. Investigation of Bit Pattern Effects . . . 35
4.2. Extinction Ratio Improvement in UL-SOAs . . . 37
4.2.1. Operation Conditions for the Extinction Ratio Improvement . . . 37
4.2.2. Reason for the Extinction Ratio Improvement . . . 40
4.2.3. Extinction Ratio Improvement With Wavelength Conversion . . . 43
4.3. High-Speed Signal Regeneration With UL-SOAs . . . 46
4.3.1. Signal Regeneration Due to the Bogatov-like Effect . . . 46
4.3.2. Using a Pulse Reformatting Filter . . . 48

**5. Supercontinuum Generation With UL-SOAs** **51**
5.1. Generation of Short Pulses . . . . . 51
5.1.1. Phase Relation of the FWM Modes . . . . . 51
5.1.2. Locking of the Generated Pulses . . . . . 52
5.1.3. Results . . . . . 52
5.1.4. Tunability of the Pulses Source . . . . . 53
5.1.5. Possible Further Improvements . . . . . 56
5.2. CoWDM Carrier Source . . . . . 56
5.2.1. Generation of Coherent CW Input Signals . . . . . 57
5.2.2. Results . . . . . 58

**6. Conclusion** **60**

**Bibliography** **62**

**A. List of Acronyms** **71**

**B. UL-SOA's Simulation Parameters** **73**
B.1. Physical Constants . . . . . 73
B.2. Material Parameters . . . . . 73
B.3. Simulation Parameters . . . . . 74

**C. Derivation of the Intrabands' Rate Equations** **76**

**D. Calculation of the Refractive Index of InGaAsP** **78**

**E. Derivation of the Simulation Model's FIR Coefficients** **79**

**F. Derivation of the Bogatov-like Effect** **81**

**G. Generation of Critical Bit Sequences** **83**

**H. Author's Publications** **84**

**I. Acknowledgements** **86**

# 1. Introduction

Semiconductor optical amplifiers (SOAs) are active semiconductor waveguides. The word active means that the light propagating through the device interacts with the semiconductor media changing the properties of the light. There are different kinds of waveguide structures the active material can be embedded in. For instance, ridge, v-grove and buried waveguides can be used and the buried waveguide can either be index or gain guiding. Fig. 1.1 illustrates the buried index guiding SOA investigated in this thesis. To

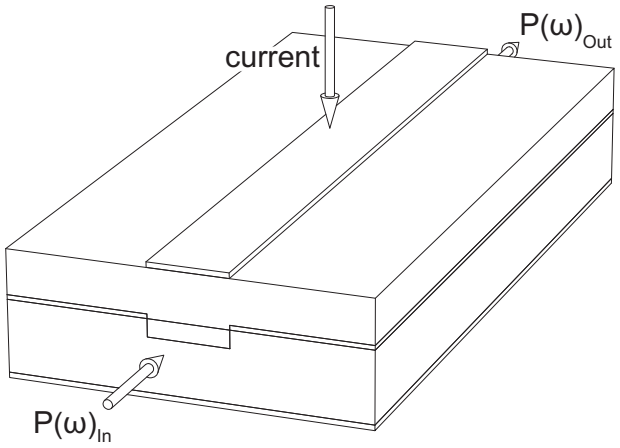


Figure 1.1.: Schematic view of an SOA; the active waveguide is a buried index-guided waveguide structure fabricated using various epitaxy steps; the optical signal is injected at the front facet $\hbar\omega_{\mathrm{In}}$ and exits the device at the rear facet $\hbar\omega_{\mathrm{Out}}$; the active region is pumped by a current in vertical direction being injected via metal contacts

propagate through the active waveguide the optical signal enters the device at the front facet and exits the device at the rear facet. The active region is made of InGaAsP being surrounded by InP. Compared to InP, InGaAsP has a larger refractive index and for this reason the active region is the core of the waveguide. With the help of metal contacts on top and at the bottom of the device a current in vertical direction pumps the active waveguide. To increase the pumping efficiency in the active region, the current is confined in the horizontal direction by a p-n-p blocking layer.

SOAs are travelling-wave amplifiers and their designs are very similar to that of semiconductor lasers. Therefore, the technical developments of SOAs and lasers are often closely related to each other (for further details see Section 2.2 of [1]). For this reason, SOAs were also called semiconductor laser amplifiers (SLAs). However, they are still very different in the sense that the facets of SOAs have anti-reflective coatings while the facets of lasers are semi-reflecting thus generating a standing wave.

## 1.1. SOAs in Optical Communications

As the name implies, in the beginning SOAs were thought for amplification of optical signals. However, with the invention of erbium doped fibre amplifiers (EDFAs) a competitor came into the market. Although SOAs can be integrated, EDFAs are broadband amplifiers with a bandwidth of up to 100 nm, a linear amplification characteristic and a low noise figure. Hence, EDFAs are always used for application if no integrated solution is needed. For this reason, other applications for SOAs had to be taken into account. Due to the highly nonlinear active medium inside of SOAs, applications in the field of all-optical signal processing are possible. E.g., wavelength conversion [2–4] or add-drop multiplexing [5–7] can be

done all-optically with SOAs. In recent years it turned out that for long-haul communication, wavelength division multiplexing (WDM) has a clear advantage over optical time-division multiplexing (OTDM) [1]. For this reason, the community became less interested in add-drop multiplexing while wavelength conversion is still an important issue for WDM systems. Moreover, a trend towards optical packet switched networks can be observed [9] where also signal regeneration [10–12] and logical operations [13–15] are needed. However, these applications can also be done with electric signal processing where first the optical signal is converted into electric domain and than processed before it is converted back into optical domain. In the 1990s, the data rates of optical communication systems was limited by the speed of the processing electronics so all-optical solutions proved superior to electric signal processing. Around the turn of the millennium the speed of optical communication systems stagnated due to the dot-com bubble while the speed of electronics still increased. As a result, nowadays the speed of electronics and optics is about the same [16]. Now cost (production cost, power consumption and size) is the main issue driven by the market where electric signal processing has clear advantages [17]. In order to make all-optical signal processing with SOAs more attractive for the market, SOAs should have a feature reducing the cost compared to electric signal processing. For instance, one feature would be simultaneous wavelength conversion of multiple WDM channels, similar to the simultaneous amplification of WDM channels with EDFAs being one of the few all-optical solutions that are applied in commercial optical communication systems. Since there have been some non-promising preliminary investigations of multichannel operations with SOAs [18, 19], SOAs thus have very limited uses.

One of the uses is high-speed signal processing for future optical communication networks at data rates above these of the processing electronics. Typically, the speed of bulk and multi-quantum well (MQW)-SOAs is limited to approximately 20 Gbaud [20, 21]. To overcome this speed limitation, quantum dot (QD)-SOAs were presented as the cure-all. But there are still problems in the fabrication and with the properties of QD devices resulting in a slow developing progress [22]. Another novel SOA-based concept for high-speed optical signal processing is to increase the length of bulk devices up to several millimetres. Due to the length of these very long SOAs, the main part of the device is not amplifying the propagating signals because the optical power saturates this region. However, in this section fast effects interact with the signals providing the ability for high-speed optical signal processing [23]. These very long SOAs are called ultralong semiconductor optical amplifiers (UL-SOAs) and its interesting properties will be discussed in this thesis.

## 1.2. Review on SOA Modeling Approaches

For designing applications with SOAs, modelling SOAs is an important issue. A better physical knowledge of the device can be obtained from modelling in order to predict optimised operation conditions for applications. For this reason, some of the important modelling approaches of SOAs from the field of optical communication are presented in this subsection.

In [24, 25] theoretical descriptions for modelling the gain and phase dynamics of SOAs are given. Another important theoretical description is the wavelength dependent gain of the active region [26–28]. Most of the analytic and numeric SOA models used for optical communication simulations are based on these descriptions.

In the beginning many theoretical investigations were analytical due to the limited computation capacity [29]. Compared to full numerical simulations, an advantage of analytic computations is a better comprehension of the physical effects being the reason for a variety of applications. However, lots of simplifications have to be made to the analytical computations as the theoretical description of [25] consists

[1] Although hero experiments with data rates in the Tb/s regime have been reported for OTDM-systems [8] the channel bandwidth is e.g., limited by dispersion and polarisation mode dispersion. Moreover, the timing tolerances and the resulting production cost for components of such systems are bigger than for similar WDM systems. Furthermore, another important aspect for the breakthrough of WDM are EDFAs because they simultaneously amplify the whole C-band of a WDM system.

of a set of partial differential equations that cannot be calculated in a closed form, hence, not all effects can be included in the computation. In full numerical models, the input signals are sampled with very short time intervals so the differential equations can be transformed into recurrence relations. As a result, the whole set of partial differential equations can be implemented. Thus full numerical models include more physical effects making the simulations more realistic. Moreover, forward and backward propagating signals can be simulated with full numerical models being very important for the noise characteristic of the device. Nowadays, almost all simulation models are full numerical models.

A very important aspect when modelling SOAs is the implementation of the gain. The material gain of the active region is dependent on both wavelength and intensity of the input signal. If the input signal is a continuous wave (CW) signal, being constant over the time, the simulation model can be a full frequency-domain model [27, 30]. In general, the signals in optical communications are time-dependent (modulated signals) therefore posing the question how to manage the frequency dependent gain and the time dependent data signal in the full numerical simulation model. Advantages of time-domain modelling are the abilities to simulate pseudo random bit sequence (PRBS) signals and the inherent implementation of dynamic nonlinear optical effects. On the other hand the implementation of the wavelength dependent gain is more complicated than for frequency-domain models. A typical solution is to calculate the signal's centre frequency with the help of the Fourier-transformation before the signal enters the SOA. Propagation can then be done in time-domain using the gain coefficient corresponding to the estimated frequency [1, 31–33]. However, when investigating the propagation of short pulses or effects like four-wave mixing (FWM), the spectra of the signals are broad and this modelling concept becomes inaccurate. To reduce the inaccuracy caused by the neglect of the gain's wavelength dependence, full time-domain models have been presented where the field propagates in time-domain and the wavelength dependence of the gain is included with the help of the finite-difference method [34–36]. However, the finite-difference method has a rather complex computational effort being unacceptable for modelling UL-SOAs in optical communication systems. For this reason, the full numerical simulation model used in this thesis is based on a simpler approach. Again, the field propagates in time-domain but this time, adaptive finite impulse response (FIR) filters implement the wavelength dependence of the gain [37–39].

## 1.3. Motivation for This Work

In the field of optical communications there are mainly three possible applications for UL-SOAs: all-optical signal processing, pulse generation and coherent wavelength division multiplexing (CoWDM) carrier source.

### 1.3.1. UL-SOAs for Wavelength Conversion With Signal Regeneration

In Sec. 1.1 it has been emphasised that all-optical high-speed signal processing is of interest in future optical packet switched networks. E.g., all-optical high-speed wavelength conversion will be needed to resolve blocking of coincident packets for the same output port of a network node [40]. There are several possibilities how all-optical wavelength conversion (AOWC) can be done but only SOA-based solutions provide the possibility for monolithic integration. In general, there are three mechanisms in SOAs that can be used to convert the signal: FWM [5, 41], cross-gain modulation (XGM) [2] and cross-phase modulation (XPM). A disadvantage when using FWM and XGM mechanism is the decreased extinction ratio (ER) of the converted output signal compared to the input data signals. Since XPM results from the index change caused by the gain change, XPM is small and can only be used for AOWC when using phase controlled switches. E.g., Mach-Zehnder interferometers (MZIs) are such phase controlled switches [3, 4]. In contrast to single path solutions, these MZIs are inherently narrowband and very sensitive to data rates or wavelengths. For this reason, there have been several approaches to combine single path regeneration concepts and single path AOWC [12, 42]. However, all these schemes are speed limited to approximately 20 Gbaud and cannot be used for high-speed data signals. On the other hand,

there are also possibilities for high-speed single path AOWC [43, 44] but these solutions decrease the quality of the signal. Nevertheless, the demand for high-speed AOWC with signal regeneration has been reported [45].

In [46], a promising novel single path concept for signal regeneration based on UL-SOAs was presented. The scheme has the potential for 2R regeneration and since the regenerator mechanism is based on the fast intraband effects, it should be suitable up to several hundred Gbaud. A first proof of concept for the high-speed potential was presented with an 80 GHz sine modulated signal [47]. Combining this novel scheme with single path wavelength conversion mechanisms could result in a high-speed all-optical wavelength converter with 2R regeneration.

### 1.3.2. Supercontinuum Generation with UL-SOAs

Due to the fast intraband effects, UL-SOAs can generate at their output broad mode combs with a narrow mode spacing. In optical communications these so called supercontinua can be used to generate short pulses or they can be used as a CoWDM carrier source.

#### Pulse Source

Pulse sources are needed for all-optical signal processing in optical packet switched networks. In packet switched networks, the components should be agile, in order to fulfil operations at different wavelengths and different data rates [9]. In general, the Kerr effect in highly nonlinear fibres (HNLFs) is used to generate a supercontinua [48] which in turn can be used to generate short pulses [49, 50]. The Kerr effect describes the depemdemce of the refractive index on the input signal's optical power and therefore causes self-phase modulation (SPM). The additional modulation in combination with a dispersion managing component creates a broader spectrum so in time domain short pulses can be obtained. However, due to the HNLFs, the source cannot be integrated. An alternative device that creates short pulses and can be integrated is the mode-locked laser (MLL) but its possibilities for tuning the repetition rate or the carrier frequency of the pulses are very limited because these properties are defined by the material and the geometry [51]. Compared to the passively MLL, the monolithic fundamental actively MLL can be tuned in the repetition rate of the pulses, but needs a complex electronic driving stage in order to achieve high repetition rates [52]. Furthermore, when reaching with the pulse duration the terahertz regime (0.6-6 THz) also non-telecommunication applications in the field of biomedical or imaging applications are possible [53, 54].

Recently, the capability of UL-SOAs for pulse compression was presented in [55] raising hope that due to their tremendous FWM efficiency UL-SOAs can generate short pulses from two CW input signals. Compared to the previously discussed methods of generating short pulses, this scheme should be widely tuneable and can be integrated.

#### CoWDM Carrier Source

Typical optical long-haul transmission systems use WDM to transmit multiple communication channels over one fibre link. In order to further increase the transmission capacity, CoWDM has been proposed [56]. In CoWDM systems, the phase of the WDM carriers is locked reducing interchannel crosstalk. Recently, it has been demonstrated that CoWDM also improves the transmission capacity for phase modulated signals [57].

The additional complexity of a CoWDM system compared to WDM system is due to the generation of phase locked carrier signals. So far, a setup of cascaded Mach-Zehnder modulator (MZM) has been used to create CoWDM carriers but only few carriers can be obtained [58]. To create more coherent carriers, a MZM was driven as an I/Q modulator in a recirculating frequency shifter in order to create single-sideband modulation of the circulating input mode [59]. A Disadvantage of this setup is that the

modulation of both MZM arms has to be very precise in order to obtain a single-sideband modulation. Also, due to the EDFAs, the scheme cannot be integrated.

Due to FWM, UL-SOAs can generate broad mode combs. These modes have an equidistant frequency spacing and their phase relation is fixed. For this reason, UL-SOAs have the ability as a CoWDM carrier source that can be monolithically integrated.

Recently, coherent optical orthogonal frequency division multiplexing (CO-OFDM) has been presented as a new concept for optical networks [60, 61] as well reducing the bandwidth of the transmitted signal. For CO-OFDM a coherent carrier source is also needed providing a further possible application of UL-SOAs.

This thesis is divided into three main parts. First, in Chap. 2 the fundamental theoretical background for the optical properties of UL-SOAs is provided. Next, Chap. 3 describes the important nonlinear optical effects that contributes to the reason for the various applications of UL-SOAs. Moreover, a simulation model is presented to represent these effects. Finally, Chap. 4 and Chap. 5 present some possible applications of UL-SOAs. Chap. 4 discusses the possibility of UL-SOAs for AOWC with 2R regeneration and Chap. 5 deals with UL-SOAs as a pulse and CoWDM source.

# 2. Optical Properties of UL-SOAs

One important property of semiconductors is the amplification and attenuation of light caused by the transition of electrons between the bands, emitting or absorbing photons. When calculating the material gain as a function of the wavelength, the energy levels of the carriers and their occupation probability with carriers needs to be known.

In general, the SOAs used for optical communication are build of ternary and quaternary III-V semiconductor compounds. The atoms of the semiconductor are located in a periodic lattice structure so the Bloch-equation can be applied to calculate the energy-levels of the carriers in a quantum-mechanical way [62, 63]. As a result the band structure can be obtained as a function of the Brillouin-zone (Fig. 2.1). Normally, the smallest band gap between the conduction and valence band (inset in Fig. 2.1) is of interest

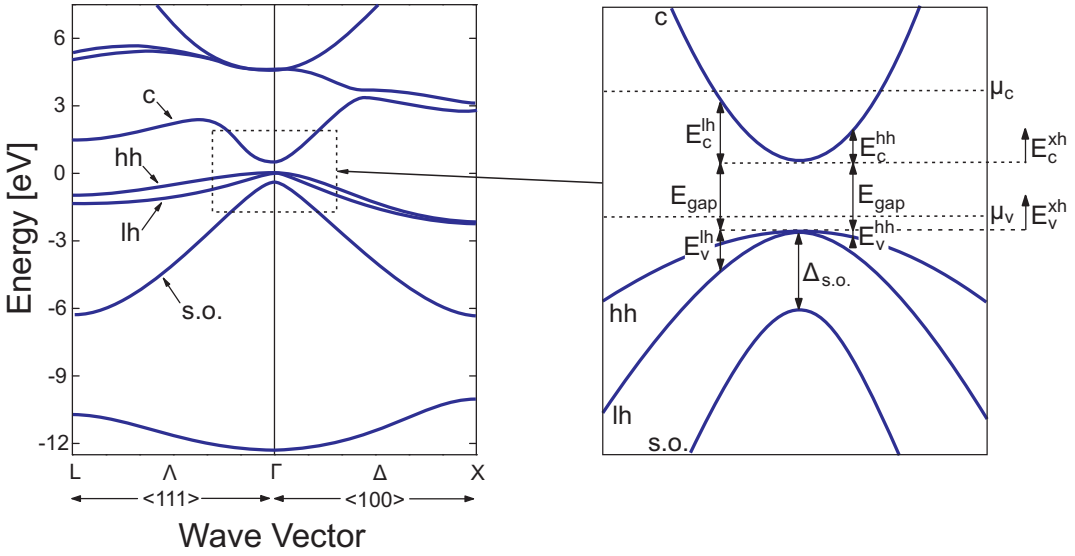


Figure 2.1.: Band structure for InAs where the energy levels are plotted over the wave vector $\vec{k}$; c, hh, lh and s.o. are the conduction band, valence band for light and heavy holes and the split-off band, respectively; L, Λ, Γ, Δ and X are important symmetry points and lines in the lattice structure; the other variables are explained in Sec. 2.1

so the band structure can be reduced to a four-level system. If the semiconductor is neither strained nor a voltage is applied the four-level system can be even reduced to a two-level system (conduction band and heavy holes). The two-level system can be described with the help of the Schrödinger equation from which the density matrix can be derived [64]. The density matrix can be transformed into an equation where the gain is a function of the optical wavelength [65] making the description of the interaction between the material and the light less complex compared to the quantum mechanical calculation.

## 2.1. Semiconductors Basics

In this subsection the gain calculation as a function of the carrier density distribution inside of a band and the therefor needed semiconductor basics are presented.

When a transition of an electron between the valence and the conduction band takes place, the energy and the momentum is conserved

$$\hbar\omega = E_{\text{gap}} + E_c^{xh} - E_v^{xh} \qquad \text{and} \qquad \vec{k}_c^{xh} + \vec{k}_{\hbar\omega} = \vec{k}_v^{xh} \quad \text{where} \quad \left|\vec{k}_{\hbar\omega}\right| \ll \left|\vec{k}_c^{xh}\right|, \left|\vec{k}_v^{xh}\right|. \tag{2.1}$$

The superscript $xh$ is either $lh$ or $hh$ and denotes whether the variable corresponds to a transition related to light holes or heavy holes. For this reason, as illustrated in Fig. 2.1, only vertical transitions of carriers are possible as long as phonon interactions are neglected. Moreover, the energy levels in each band are directly related to a momentum. In bulk materials the dependence can be approximated with a parabolic function

$$E_c^{xh} = \frac{\hbar^2 \left|\vec{k}\right|^2}{2\,m_e} \qquad \text{and} \qquad E_v^{xh} = -\frac{\hbar^2 \left|\vec{k}\right|^2}{2\,m_{xh}}. \tag{2.2}$$

The other variables are given in Sec. B.2. From Eq. 2.1 and 2.2 the energy-level of the carriers in each band corresponding to a photon induced electron transition can be derived

$$E_c^{xh} = \left(\hbar\omega - E_{\text{gap}}\right)\frac{m_{xh}}{m_e + m_{xh}} \qquad \text{and} \qquad E_v^{xh} = \left(E_{\text{gap}} - \hbar\omega\right)\frac{m_e}{m_e + m_{xh}}. \tag{2.3}$$

The number of possible states of each energy-level that can be occupied with carriers is given by the density of state. In bulk devices the dependence of the density of states on the energy is given by the following equations:

$$D_c = \frac{1}{2\pi^2}\sqrt{E_c^{xh}\left(\frac{2\,m_e}{\hbar^2}\right)^3} \quad \text{and} \quad D_v^{xh} = \frac{1}{2\pi^2}\sqrt{-E_v^{xh}\left(\frac{2\,m_{xh}}{\hbar^2}\right)^3} \tag{2.4}$$

Fig. 2.2 shows the density of states of the conduction band. The values of the variables, used for the

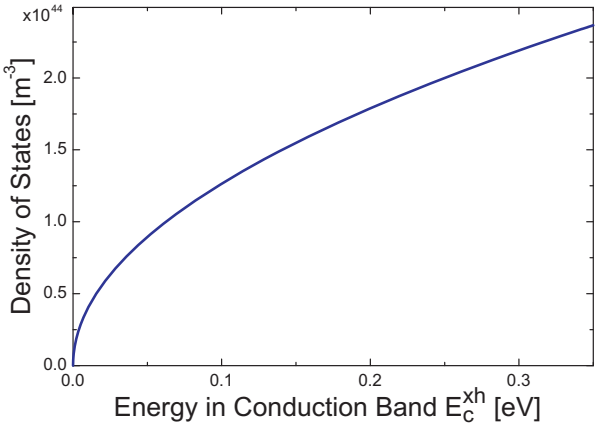


Figure 2.2.: Density of states inside the conduction band as a function of the energy in the conduction band

calculations, are given in Sec. B.1 and Sec. B.2. In equilibrium, the probability of the carrier distribution inside a band is given by the Fermi-Dirac distribution (Fig. 2.3)

$$f_c = \frac{1}{\exp\left(\frac{E_c^{xh} + E_{\text{gap}} - \mu_c}{k_B T}\right) + 1} \quad \text{and} \quad f_v = \frac{1}{\exp\left(\frac{E_v^{xh} - \mu_v}{k_B T}\right) + 1}. \tag{2.5}$$

The calculation of the quasi-fermi levels $\mu_{c,v}$ is presented in Sec. B.2. When multiplying Eq. 2.5 and 2.4 the carrier density distribution of a band can be calculated ($\rho_c = D_c f_c$ and $\rho_v = (D_v^{hh} + D_v^{lh}) f_v$, Fig. 2.4). Furthermore, the overall number of carriers inside each band can be calculated when integrating over all energy-levels:

$$N = \int_0^\infty \rho_c \,\mathrm{d}E_c^{xh} \quad \text{and} \quad P = \int_{-\infty}^0 \rho_v \,\mathrm{d}E_v^{xh}. \tag{2.6}$$

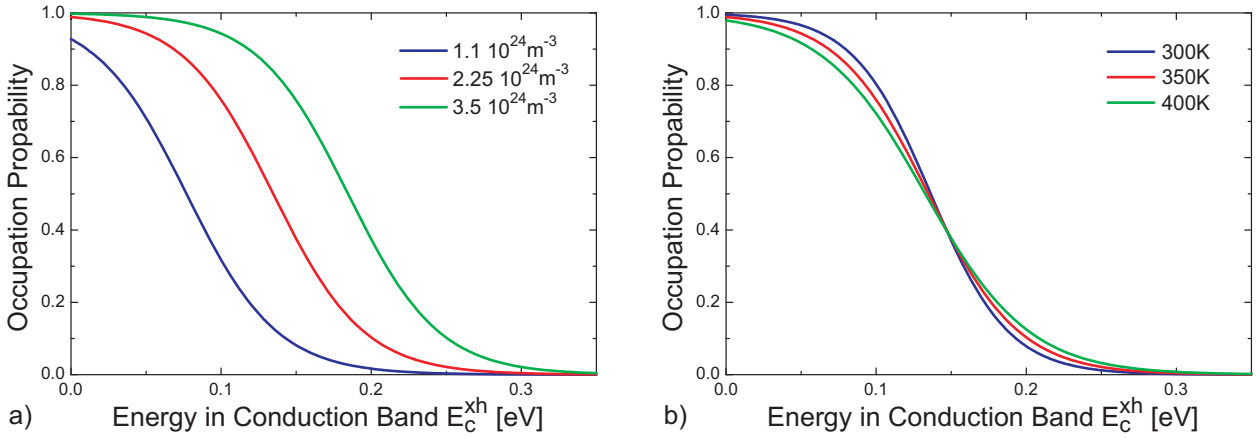


Figure 2.3.: Fermi-Dirac distribution inside the conduction band for different carrier densities and temperatures; for the carrier density variation $T = 350\,\mathrm{K}$ and for the temperature variation $N = 2.2510^{24}\,\mathrm{m}^{-3}$

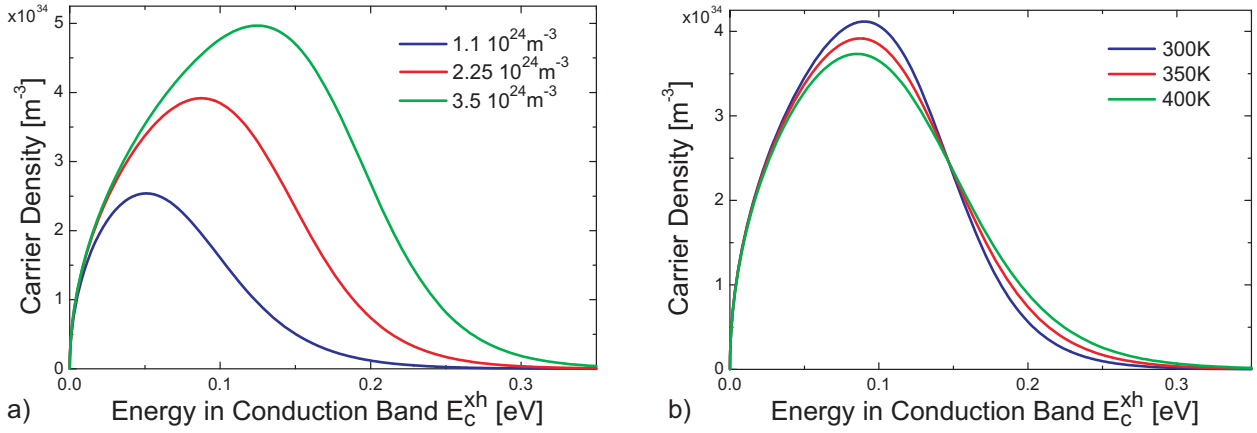


Figure 2.4.: Carrier density distribution inside the conduction band for different carrier densities and temperatures; for the carrier density variation $T = 350\,\mathrm{K}$ and for the temperature variation $N = 2.2510^{24}\,\mathrm{m}^{-3}$

### 2.1.1. Interband Effects

In general, in active semiconductors it is distinguished between three main mechanisms for carrier transitions between the conduction and the valence band: stimulated emission, spontaneous emission and absorption. For all three processes the band gap energy has to be less or equal than the interacting photon energy ($E_{\mathrm{gap}} \leq \hbar\,\omega$).

**Stimulated Emission:** When a photon propagates in a semiconductor medium and passes an electron being located in the conduction band at an energy level corresponding to the photon energy, with a certain probability the photon can cause a transition of the electron from the conduction band to the valence band. Due to the energy conservation a coherent photon is emitted co-propagating with the original photon. From a macroscopic point of view optical signals are amplified in their intensity respectively power.

**Spontaneous Emission:** With a certain probability a transition of an electron from the conduction band to the valence band can take place without any external interaction. The effect is caused by the limited time that an electron can exist in the conduction band (carrier lifetime). Since the transition is nondeterministic and the photon is emitted at a random time, the effect is causing noise in active semiconductors.

**Absorption:** Depending on the occupation probability of carriers in the bands, a photon can be absorbed when propagating through the semiconductor media. As a result an electron is transferred from

an energy level of the valence band into an energy level in the conduction band with an energy difference corresponding to the photon energy. Another variant of absorption is the two-photon absorption (TPA) where two photons are absorbed at the same time and the transition of an electron to an energy level corresponding to the sum of the two photons

$$2 \cdot \hbar\omega = E_{\text{gap}} + E_c^{xh} - E_v^{xh}. \tag{2.7}$$

Latter type of absorption is rare compared to former type. Macroscopically, optical signals are attenuated due to absorption.

The material gain describes how stimulated emission and absorption affect optical signals. With the help of the semiconductor basics (Sec. 2.1), the material gain of semiconductors can be calculated [26, 66]:

$$g_{\text{mat}}^{xh}(\omega) = \begin{cases} \frac{2\pi^2 e^2}{\epsilon_0 n_G c_0 m_0^2 \omega} \left|M_{\text{avg}}\right|^2 \cdot D_{\text{red}}^{xh} \left(f_c + f_v - 1\right) & \text{if} \quad \omega > \omega_{\text{gap}} \\ 0 & \text{if} \quad \omega \leq \omega_{\text{gap}} \end{cases} . \tag{2.8}$$

with $D_{\text{red}}^{xh} = \frac{\sqrt{2}}{\pi^2 \hbar^3} \sqrt{\hbar\omega - E_{\text{gap}}} \left(\frac{m_e m_{xh}}{m_e + m_{xh}}\right)^{3/2}$ being the reduced density of states. The other parameters are explained in Sec. B. $g_{\text{mat}}^{xh}(\omega)$ represents the material gain due to transitions between the conduction and the heavy hole band or the light hole band so $xh$ is either $lh$ or $hh$.

Eq. 2.8 only holds for strict momentum conservation of the carriers. However, also transitions with slight momentum detuning take place because the energy-levels spread out due to temperature broadening mechanisms. Therefore, even the gain energy-levels close by a certain energy-level contribute to the gain. This mechanism can be included when convoluting the gain with a lineshape function

$$g_{\text{mat}}(\omega) = \int_{-\infty}^{\infty} \left(g_{\text{mat}}^{hh}(\omega') + g_{\text{mat}}^{lh}(\omega')\right) L(\omega - \omega') \mathrm{d}\omega'. \tag{2.9}$$

Typically, Lorentzian lineshape functions are used to approximate the mechanism but nowadays investigations show that Sech-functions are more appropriate [26]

$$L(\omega) = \frac{\tau_{\text{SHB}}}{2} \operatorname{sech}^2 \left(\tau_{\text{SHB}} \frac{\omega}{2\pi}\right). \tag{2.10}$$

Fig. 2.5 shows the wavelength dependent material gain as a function of the carrier density and the temperature. Another effect that has been considered for the calculation of the gain is band gap shrinkage due to a variation of the carrier density or the temperature. As the carrier density or the temperature increases the band gap energy decreases [67, 68]. The formulae for the band gap shrinkage are given in Sec. B.2.

The shape of the material gain profile can be related to the probability of absorption and stimulated emission. The gain profile can be divided into three regimes: For wavelengths above the band gap wavelength, the material is transparent and the semiconductor can be regarded as a passive medium. Between the band gap wavelength and the difference Fermi-level wavelength [1], the gain regime can be found. In this regime the occupation probability for an electron in the conduction band is above the occupation probability that there is an electron at the corresponding energy level in the valence band being given by the Fermi-Dirac-distribution. Hence, more stimulated emission than absorption takes place so that light is amplified in this wavelength regime. The last regime is the absorption regime for wavelengths below the difference Fermi-level wavelength. In this regime more electrons are in the valence band than in the conduction band. As a result absorption dominates compared to stimulated emission.

[1] wavelength at which the gain profile becomes negative

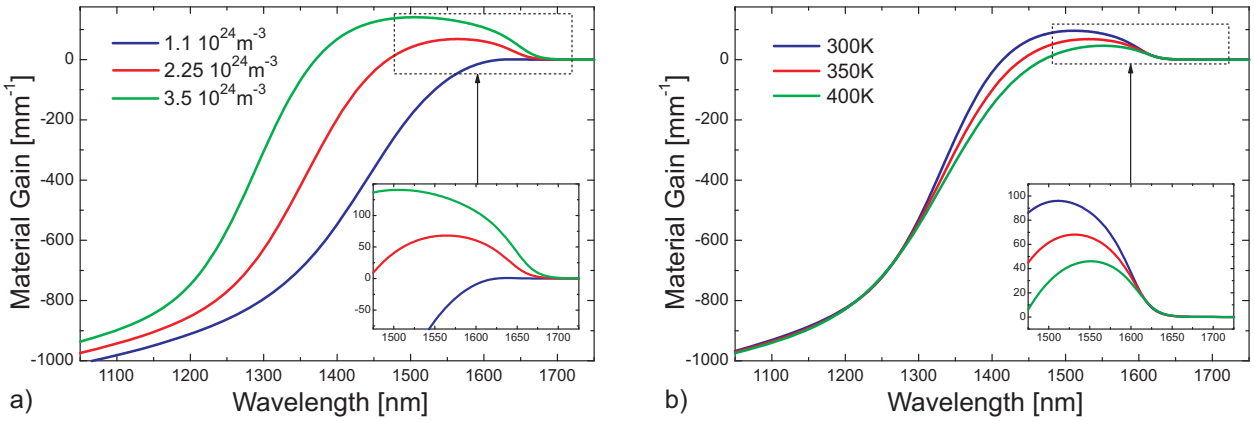


Figure 2.5.: Wavelength dependent gain for different carrier densities and temperatures; the values for the variables used in the calculation are given in Sec. B.1 and Sec. B.2; for the carrier density variation $T = 350\,\mathrm{K}$ and for the temperature variation $N = 2.2510^{24}\,\mathrm{m}^{-3}$

### 2.1.2. Intraband Effects

While in Sec. 2.1.1 the effects for transition between the conduction and valence bands were presented, this section deals with the dynamics inside a band because of carrier transitions.

Fig. 2.6 shows the carrier dynamics inside the conduction band that take place after stimulated emission. In the beginning the semiconductor is in thermal equilibrium. As a photon causes stimulated emission while propagating through the semiconductor, the carrier density depletes at the corresponding energy level. Since at this energy level the carrier density is depleted the gain for the corresponding wavelength is also reduced. This intraband effect is called spectral hole burning (SHB). In the second step, the carrier density distribution relaxes due to carrier-carrier scattering to a fermi-distribution as for a higher temperature. This intraband effect is called carrier heating (CH). Even if the local depletion of carriers is compensated, Fig. 2.5 shows that the gain is reduced for an increased temperature. In the third step, the carrier density distribution reorganises to a fermi-distribution corresponding to the lattice temperature due to carrier-phonon scattering. Since only in the last step the missing carrier density due to the pump current is injected the gain is still reduced after the third step. The relaxation mechanisms do not take place sequently but due to the different time constants of each process (1: immediately, 2: $\sim$125 fs, 3: $\sim$750 fs and 4: $\sim$300 ps [20, 21]), the contributions of slower effects to faster relaxation mechanisms is negligible.

A similar behavior of the carrier density distribution can be observed for an absorption process (Fig. 2.7). Again starting with a semiconductor in thermal equilibrium, a photon is absorbed in the first step. As a result at the corresponding energy level the carrier density is locally increased and compared to the carrier dynamics due to stimulated emission the gain for the corresponding wavelength increases (SHB). In the second step the carriers reorganise, due to carrier-carrier scattering to a fermi-distribution as for a higher temperature (CH), resulting in a decreased gain. Again due to carrier-phonon scattering, the carrier density distribution relaxes to a fermi-distribution corresponding to the lattice temperature. Similar to the carrier dynamics due to stimulated emission, the additional carrier density due to the absorption in the beginning reduces to the original distribution due to stimulated or spontaneous emission in the last step.

The development of the carrier dynamics can be indirectly observed when the power change of a probe signal from a pump-probe measurement [2] is regarded. In Fig. 2.8 the different mechanisms can be

[2]Pump-probe measurement: A strong pulse (pump) and a weak CW signal (probe) enter a semiconductor. While the probe signal has nearly no influence on the carriers, the strong pulse causes carrier depletion or enhancement. At the output of the semiconductor the probe signal is regarded at an oscilloscope indicating the carrier dynamics inside the semiconductor due to its power change

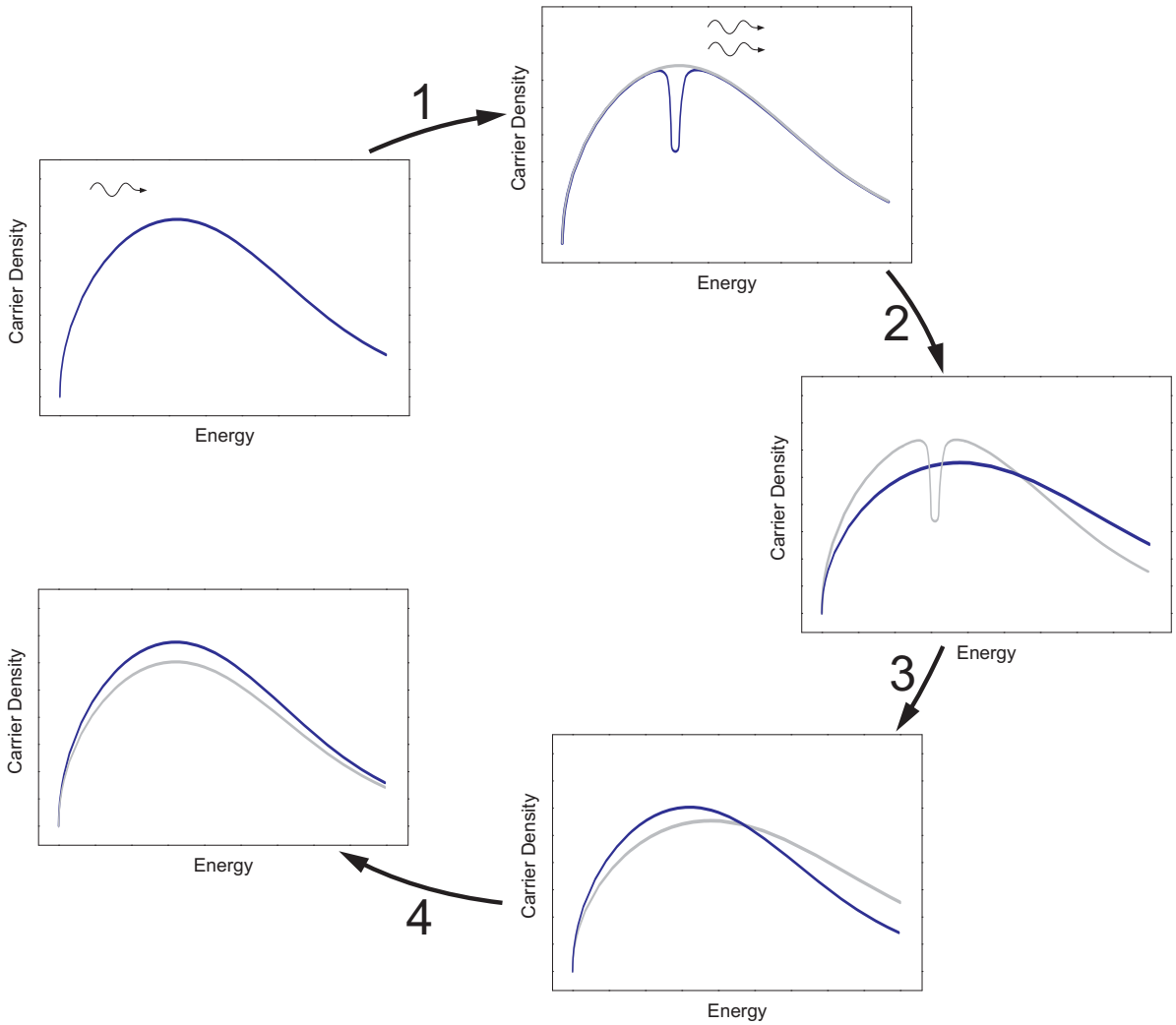


Figure 2.6.: Carrier dynamics inside the conduction band after stimulated recombination (grey line: previous state); 1: spectral hole burning due to stimulated recombination, 2: relaxation to fermi-distribution of the carrier temperature due to carrier-carrier scattering, 3: relaxation to fermi-distribution of the lattice temperature due to carrier-phonon scattering and 4: relaxation to fermi-distribution in equilibrium due to carrier injection

separated due to the different time constants because the contributions of slower effects are negligible to faster effects that take place earlier in time. Moreover, when comparing the two pump-probe characteristics for the gain regime all mechanisms are gain suppressing while in the absorption regime SHB and the interband effects are gain enhancing and CH is still gain suppressing [69,70].

Furthermore, other effects like TPA and free carrier absorption (FCA) contribute to the intraband effects. Typically, the influence of FCA in the valence band is negligeable. Hence, FCA related transitions are as follows: phonon-assisted intraconduction band absorption, phonon-assisted interconduction band absorption and interconduction band absorption [69,71]. For all of these transitions an electron is transfered to a higher energy level increasing the carrier temperatures. For this reason, FCA contributes to CH. Since the carrier temperature also increases due to TPA, TPA contributes to CH too.

### 2.1.3. Gain Dynamics

To calculate the gain dynamics of semiconductors (Fig. 2.8) a mathematical description is needed being presented in this subsection.

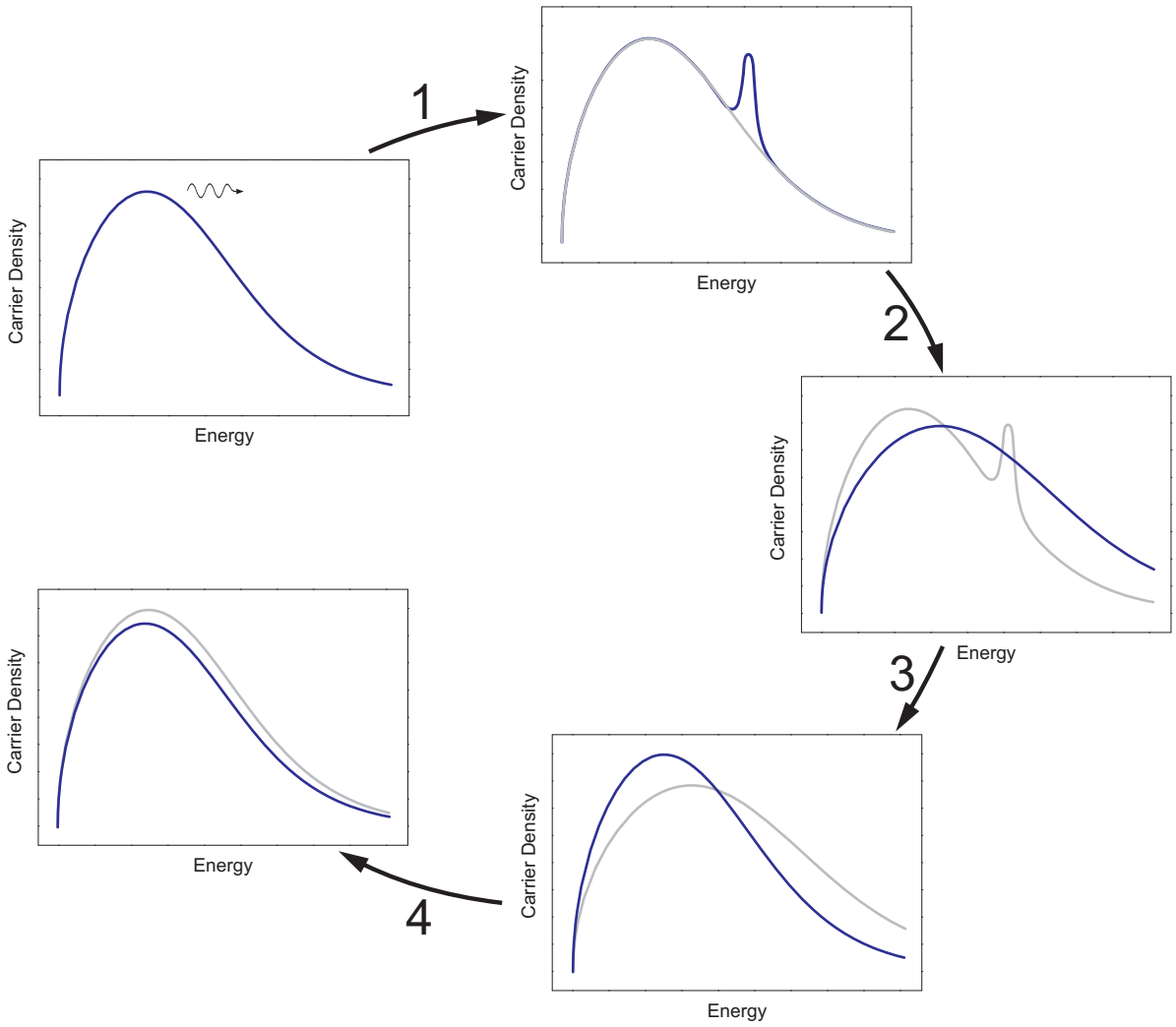


Figure 2.7.: Carrier dynamics inside the conduction band after absorption (grey line: previous state); 1: inverse spectral hole burning due to absorption, 2: relaxation to fermi-distribution of the carrier temperature due to carrier-carrier scattering, 3: relaxation to fermi-distribution of the lattice temperature due to carrier-phonon scattering and 4: relaxation to fermi-distribution in equilibrium due to spontaneous emission

According to [73] the total gain of the semiconductor at the peak of the gain profile is

$$g(\omega_{\text{peak}}) = g_{\text{mat}}(\omega_{\text{peak}}, T) + g_{\text{SHB}} = g_{\text{CDP}} + g_{\text{CH}} + g_{\text{FCA}} + g_{\text{TPA}} + g_{\text{SHB}}. \tag{2.11}$$

The contributions of the interband effects are represented with $g_{\text{CDP}}$ and the contribution of each intraband effect with $g_{\text{SHB}}$, $g_{\text{CH}}$, $g_{\text{FCA}}$ and $g_{\text{TPA}}$.

Stimulated emission, spontaneous emission and absorption are interband effects affecting the carrier density of a band. Due to the carrier lifetime $\tau_{\text{CDP}}$ the carrier density population is not instantaneously in equilibrium if the pump current, the stimulated emission or the absorption changes. For this reason, the interband dynamics are speed limited to the carrier lifetime. This so called carrier density pulsation (CDP) can be described with a rate equation [72]

$$\frac{\partial N}{\partial t} = \underbrace{\frac{I}{eV}}_{\substack{\text{pump}\\ \text{current}}} - \underbrace{\frac{N}{\tau_{\text{CDP}}}}_{\text{spon. emission}} - \underbrace{v_{\text{G}} g S}_{\substack{\text{stim. emission}\\ \text{\& absorption}}} + \underbrace{\frac{\Gamma_{\text{TPA}}}{w d} v_{\text{G}} \kappa \beta_{\text{TPA}} S^2}_{\text{TPA}} \tag{2.12}$$

with $S$ being the photon density, $v_{\text{G}} = c_0/n_{\text{G}}$, $g$ the total gain (Eq. 2.11) and $\tau_{\text{CDP}}^{-1} = A_{\text{nr}} + B_{\text{sp}} N +$

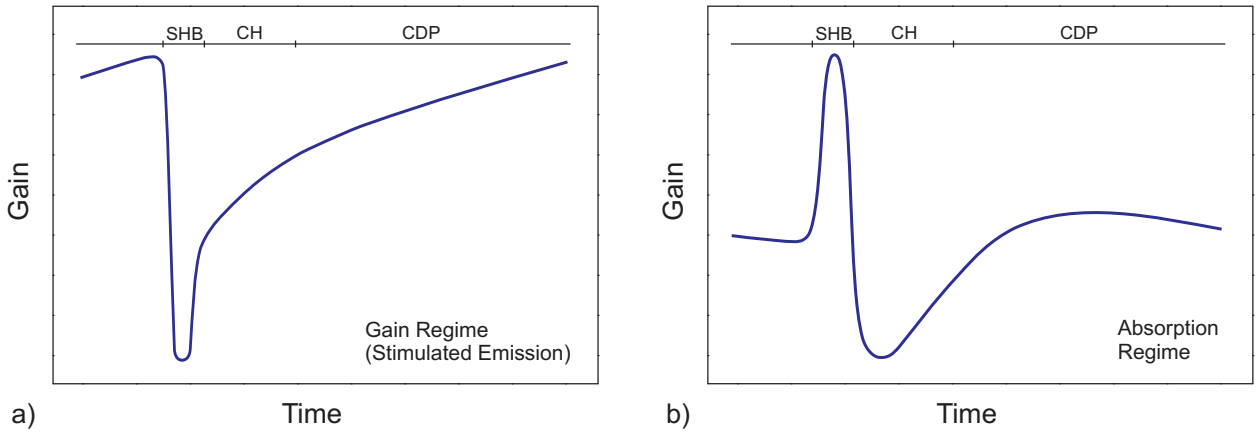


Figure 2.8.: Illustration of the carrier dynamics due to stimulated emission and absorption indicated by the gain of a probe signal from pump probe measurements; the separation is possible due to the different time constants: $\tau_{\mathrm{SHB}} \approx 125\,\mathrm{fs}$, $\tau_{\mathrm{CH}} \approx 750\,\mathrm{fs}$ and $\tau_{\mathrm{CDP}} \approx 300\,\mathrm{ps}$; carrier density pulsation (CDP) represents the interband effects

$C_{\mathrm{Auger}} N^2$. Depending on the carrier density, the carrier lifetime has a value between 200 ps and 400 ps for InGaAsP semiconductors around 1550 nm [20, 21]. Again, the other variables are explained in Tab. B.1 and Tab. B.2. To calculate the gain at the peak wavelength caused by the interband effects directly from Eq. 2.12, Eq. 2.9 can be linearly approximated as a function of the carrier density

$$g_{\mathrm{CDP}}(N) = \frac{\mathrm{d}g}{\mathrm{d}N}(N - N_{\mathrm{tr}}) \tag{2.13}$$

with $\frac{\mathrm{d}g}{\mathrm{d}N}$ being the differential gain coefficient (Tab. B.2).

The intraband effects can also be described with a set of rate equations

$$\frac{\partial g_{\mathrm{CH}}}{\partial t} = -\frac{g_{\mathrm{CH}}}{\tau_{\mathrm{CH}}} - \frac{\epsilon_{\mathrm{CH}}}{\tau_{\mathrm{CH}}} g\, S \tag{2.14a}$$

$$\frac{\partial g_{\mathrm{FCA}}}{\partial t} = -\frac{g_{\mathrm{FCA}}}{\tau_{\mathrm{CH}}} - \frac{\epsilon_{\mathrm{FCA}}}{\tau_{\mathrm{CH}}} \frac{\mathrm{d}g}{\mathrm{d}N} N\, S \tag{2.14b}$$

$$\frac{\partial g_{\mathrm{TPA}}}{\partial t} = -\frac{g_{\mathrm{TPA}}}{\tau_{\mathrm{CH}}} - \frac{\epsilon_{\mathrm{TPA}}}{\tau_{\mathrm{CH}}} \frac{\Gamma_{\mathrm{TPA}}}{w\, d} \kappa \beta_{\mathrm{TPA}}\, S^2 \tag{2.14c}$$

$$\frac{\partial g_{\mathrm{SHB}}}{\partial t} = -\frac{g_{\mathrm{SHB}}}{\tau_{\mathrm{SHB}}} - \frac{\epsilon_{\mathrm{SHB}}}{\tau_{\mathrm{SHB}}} g\, S - \left( \frac{\partial g_{\mathrm{CH}}}{\partial t} + \frac{\partial g_{\mathrm{FCA}}}{\partial t} + \frac{\partial g_{\mathrm{TPA}}}{\partial t} + \frac{\partial g_{\mathrm{CDP}}}{\partial t} \right) \tag{2.14d}$$

These rate equations account for SHB, CH and the contributions of FCA and TPA to CH. For further details of the rate equations' derivation see Sec. C and for the description of the parameters see Tab. B.2.

### 2.1.4. Kramers-Kronig Relation

The Kramers-Kronig relation connects the real and the imaginary parts of complex response functions of physical systems [74]. It is a special case of the Hilbert-transformation and a result of causality in physical systems. In optics the real and the imaginary part of the susceptibility $\chi$ depend on each other. Since the susceptibility is equivalent to the permittivity $\varepsilon = \varepsilon_0(1+\chi)$ which in turn is related to the complex refractive index $\varepsilon = \bar{n}^2$, the real and the imaginary part of the complex refractive index

$$\bar{n}(\omega) = n(\omega) + i\frac{g(\omega)}{k} \tag{2.15}$$

are also related to each other because of the Kramers-Kronig relation [75]

$$n(\omega) = 1 + \frac{c_0}{\pi} \mathscr{P} \int_0^\infty \frac{-g(\Omega)}{\Omega^2 - \omega^2} \, \mathrm{d}\Omega \tag{2.16}$$

where $\mathscr{P}$ denotes the principal value of the integral. A detailed derivation of the Kramers-Kronig relation for the example of the complex refractive index is given in [76]. The integral in Eq. 2.16 has to be calculated over an infinite interval. Hence, the gain model also has to be precise at very high frequencies even if the calculated refractive index is at a frequency close to the band gap. For this reason, in the majority of cases the refractive index change $\Delta n(\omega)$ is calculated with a gain change $\Delta g(\omega)$ that can be obtained from the gain model given in Eq. 2.9 [79, 80]. Fig. 2.9 shows the refractive index change ($\Delta n = n - n_{\mathrm{ref}}$) caused by the gain change calculated from Fig. 2.5 with $n_{\mathrm{ref}}$ being calculated for $T = 300\,\mathrm{K}$ and $N = 1.110^{24}\,\mathrm{m}^{-3}$. The gain change is caused due to a change of the carrier density $\Delta N$ and a change of the temperature $\Delta T$.

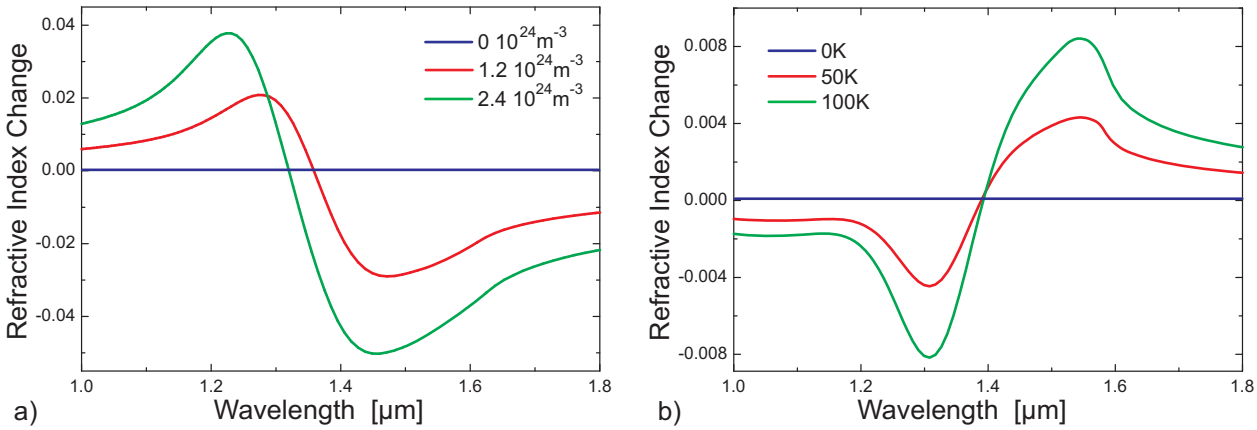


Figure 2.9.: Refractive index change caused by a gain change like in Fig. 2.5 due to a change of the carrier density $\Delta N$ a) and a change of the temperature $\Delta T$ b); $n_{\mathrm{ref}}$ has been calculated for $T = 300\,\mathrm{K}$ and $N = 1.110^{24}\,\mathrm{m}^{-3}$; for the carrier density variation $T = 300\,\mathrm{K}$ and for the temperature variation $N = 1.110^{24}\,\mathrm{m}^{-3}$

In order to provide causality a gain change causes a refractive index change. The ratio between both changes is called $\alpha$-factor [77, 78]

$$\alpha_{\mathrm{CDP}} = \frac{\frac{\partial \mathrm{Re}(\chi)}{\partial N}}{\frac{\partial \mathrm{Im}(\chi)}{\partial N}} \qquad \alpha_{\mathrm{CH}} = \frac{\frac{\partial \mathrm{Re}(\chi)}{\partial T}}{\frac{\partial \mathrm{Im}(\chi)}{\partial T}} \qquad \alpha_{\mathrm{SHB,FCA}} = \frac{\frac{\partial \mathrm{Re}(\chi)}{\partial \rho}}{\frac{\partial \mathrm{Im}(\chi)}{\partial \rho}}. \tag{2.17}$$

With the help of the Kramer-Kronig relation the $\alpha$-factor can be calculated. The results are given in Fig. 2.10 for $\Delta N$ and $\Delta T$. The calculated results are in good agreement with the experimental data in [78, 80].

Similar to Eq. 2.11 for the gain, an equation for the induced phase change due to the carrier dynamics can be given

$$\begin{aligned} \frac{\partial \phi}{\partial z} = \frac{1}{2}\Gamma \big( & \alpha_{\mathrm{CDP}} \left( g_{\mathrm{CDP}}(N) - g_{\mathrm{CDP}}(N_{\mathrm{un}}) \right) \\ & + \alpha_{\mathrm{CH}}\, g_{\mathrm{CH}} + \alpha_{\mathrm{TPA}}\, g_{\mathrm{TPA}} + \alpha_{\mathrm{SHB}}\, g_{\mathrm{SHB}} + \alpha_{\mathrm{FCA}}\, g_{\mathrm{FCA}} \big) \end{aligned} \tag{2.18}$$

with $N_{\mathrm{un}} = \frac{I}{eV}\tau_{\mathrm{CDP}}$ being the unsaturated carrier density that can be obtained from Eq. 2.12 in absence of any stimulated emission or absorption.

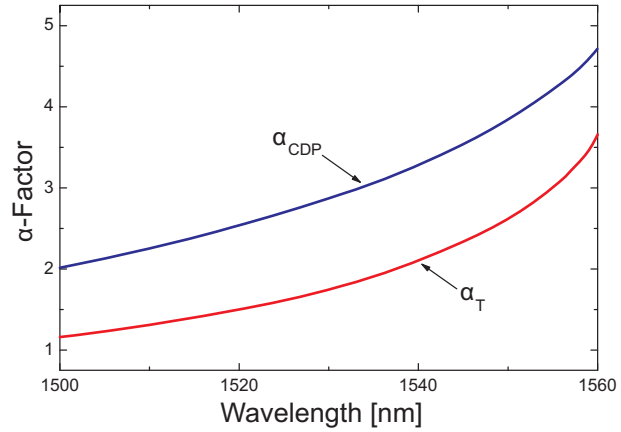


Figure 2.10.: $\alpha_{\mathrm{CDP}}$ and $\alpha_{\mathrm{T}}$ around the gain peak wavelength; the $\alpha$-factors were calculated from the refractive index change of Fig. 2.9 and the corresponding gain change similar to Fig. 2.5; independent from which $\Delta N$ or $\Delta T$ of Fig. 2.9 the corresponding $\alpha$-factors are calculated nearly same results are obtained

## 2.2. Optical Wave Propagation in UL-SOAs

All electromagnetic phenomena are described by the Maxwell equations

$$\nabla \times \vec{H} = \vec{J} + \frac{\partial}{\partial t}\left(\varepsilon_0 \vec{E} + \vec{P}\right) \tag{2.19a}$$

$$\nabla \times \vec{E} = -\frac{\partial}{\partial t}\left(\mu_0 \vec{H} + \vec{M}\right) \tag{2.19b}$$

$$0 = \nabla \cdot \left(\mu_0 \vec{H} + \vec{M}\right) \tag{2.19c}$$

$$\rho = \nabla \cdot \left(\varepsilon_0 \vec{E} + \vec{P}\right) \tag{2.19d}$$

where $\vec{P}$, $\vec{E}$ and $\vec{H}$ are the electric polarisation, the electric and the magnetic field, respectively. Assuming that there is no free charge ($\rho = 0$) and no magnetic polarisation ($\vec{M} = 0$) in the semiconductor, the Helmholtz equation can be derived with the help of the Ohmic law $\vec{J} = \sigma \vec{E}$ [62]

$$\nabla^2 \vec{E} - \frac{\sigma}{\varepsilon_0 c_0^2}\frac{\partial}{\partial t}\vec{E} - \frac{1}{c_0^2}\frac{\partial^2}{\partial t^2}\vec{E} = \frac{1}{\varepsilon_0 c_0^2}\frac{\partial^2}{\partial t^2}\vec{P}. \tag{2.20}$$

The wave equation describes how the electric field and the electric polarisation interact. In this thesis, the investigated nonlinear media are InP and InGaAsP being anisotropic. Hence, the electric polarisation and the electric field are parallel. Furthermore, due to the short polarisation dephasing time (approximately 25 fs), the dependence of the electric polarisation on the electric field can be assumed to be instantaneous [65, 81]. As a result the steady state approximation of the polarisation can be used

$$\vec{P} = \varepsilon_0 \chi \vec{E} \tag{2.21}$$

where the susceptibility couples the optical field and the electric polarisation. The susceptibility can be decomposed into a term for the susceptibility in absence of any external influences $\chi_0$ and a term related to the resonant nonlinearities due to electric pumping and the photon density $\chi_{\mathrm{NL}}$ [82]

$$\chi = \chi_0 + \chi_{\mathrm{NL}} \qquad \text{with} \qquad \chi_{\mathrm{NL}} = \frac{c_0 n}{\omega}\sum_x \left(i - \alpha_x\right) g_x \tag{2.22}$$

where $x$ is CDP, SHB, CH, FCA and TPA.

For the propagation of the optical field inside the SOA an ideal travelling-wave amplifier is assumed only guiding the fundamental mode and conserving the optical polarisation of the field. Hence, the transverse field component $\Psi(x,y)$ can be separated from the longitudinal field component $E(z,t)$ [83]

$$\vec{E} = \frac{1}{2}(\Psi(x,y)E(z,t) + c.c.)\vec{e}_p. \tag{2.23}$$

Since the cladding of the waveguide is a passive material ($\chi_{\text{clad}} \approx \chi_{0,\text{clad}}$) and the core of the waveguide is active ($\chi_{\text{core}} = \chi_{0,\text{core}} + \chi_{\text{NL,core}}$) only a certain part of the transverse field component is affected by $\chi_{\text{NL}}$. For this reason, the mode confinement of the active region is defined:

$$\Gamma = \frac{\int_0^w \int_0^d |\Psi(x,y)|^2 \,\mathrm{d}x\,\mathrm{d}y}{\int_{-\infty}^{\infty} \int_{-\infty}^{\infty} |\Psi(x,y)|^2 \,\mathrm{d}x\,\mathrm{d}y} \tag{2.24}$$

With the help of the mode confinement and the separation approach from Eq. 2.23, Eq. 2.20 can be simplified to a 1D wave equation

$$\nabla^2 E(z,t) - \frac{\sigma}{\varepsilon_0 c_0^2}\frac{\partial}{\partial t}E(z,t) - \frac{n_{0,\text{eff}}^2 + \Gamma\chi_{\text{NL,core}}}{c_0^2}\frac{\partial^2}{\partial t^2}E(z,t) = 0 \tag{2.25}$$

with $n_{0,\text{eff}}$ being the effective refractive index related to the effective susceptibility $\chi_{0,\text{eff}}$ of the waveguide. This wave equation can be further simplified by assuming that the envelope of the propagating light varies slowly in time and space compared to the wavelength of light

$$E(z,t) = A(z,t)\exp(i(\omega t - k z)) \tag{2.26}$$

with $A(z,t)$ being the slowly varying envelope and the wavenumber $k = n_{0,\text{eff}}\frac{\omega}{c_0}$. Due to the slowly varying envelope approximation, two constrains are inherently implied $\left|\frac{\partial^2}{\partial t^2}A(z,t)\right| \ll \left|\omega\frac{\partial}{\partial t}A(z,t)\right|$ and $\left|\frac{\partial^2}{\partial z^2}A(z,t)\right| \ll \left|k\frac{\partial}{\partial z}A(z,t)\right|$ reducing Eq. 2.25 to a first-order wave equation

$$\frac{\partial}{\partial z}A(z,t) + \left(\frac{n_{\text{G}}}{c_0} + \frac{\Gamma\chi_{\text{NL,core}}}{n_{0,\text{eff}}c_0} - i\frac{\alpha_{\text{int}}}{2\omega}\right)\frac{\partial}{\partial t}A(z,t) = -\frac{1}{2}\left(\frac{i\omega}{2n_{0,\text{eff}}c_0}\Gamma\chi_{\text{NL,core}} + \alpha_{\text{int}}\right)A(z,t) \tag{2.27}$$

with $\alpha_{\text{int}} = \frac{\sigma}{c_0\varepsilon_0 n_{0,\text{eff}}}$ accounting for internal losses. Transforming Eq. 2.27 into frequency domain and using Eq. 2.22 the following simple propagation equation for the electric field inside UL-SOAs is obtained:

$$\frac{\partial}{\partial z}A(z,\omega) = \frac{1}{2}\left(\Gamma\sum_x (g_x + i\alpha_x) - \alpha_{\text{int}}\right)A(z,\omega) \tag{2.28}$$

Even if the propagation of an optical field is only related to the electric field, the magnetic field component can be calculated with the help of the Faraday's law of induction (Eq. 2.19b).

## 2.3. Chromatic Dispersion in UL-SOAs

Chromatic dispersion is the phenomenon in which the phase velocity of a wave depends on its wavelength as a result of the refractive index's wavelength dependence. Typical UL-SOAs are buried active single mode waveguides. For this reason, mainly material dispersion and waveguide dispersion contribute to the overall chromatic dispersion.

The chromatic dispersion for the 8 mm-long UL-SOA from Sec. B.3 is calculated in this section. The investigated active waveguide is a buried waveguide with a bulk $In_{1-x}Ga_xAs_yP_{1-y}$ active region with $\lambda_{gap} = 1530$ nm. Since the active layer is surrounded by InP, the molar fractions of the $In_{1-x}Ga_xAs_yP_{1-y}$ layer have to fulfil the lattice matched condition (Eq. B.3). In order to obtain a band gap wavelength of 1530 nm, the molar fractions have to be $y = 0.88$ and $x = 0.31$. The width and the height of the active region are 1.2 µm and 0.2 µm, respectively. Due to a lower refractive index the surrounding InP substrate can be regarded as the cladding of the waveguide. The mode confinement of the active region is about 0.4 around 1550 nm.

### 2.3.1. Waveguide Dispersion

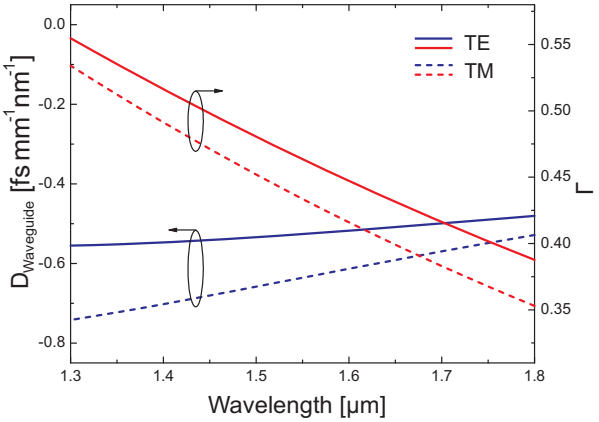


Figure 2.11.: Waveguide dispersion and mode confinement for the TM and TE mode; the mode confinement factor of the cladding can be calculated from the active region's mode confinement ($\Gamma_{cladding} = 1 - \Gamma$)

Fig. 2.11 shows the waveguide dispersion for the transverse magnetic (TM) and transverse electric (TE) mode. The waveguide dispersion is calculated from the second derivation of the propagation constant $\beta = k\,n$

$$D = -\frac{\lambda}{c_0}\frac{\mathrm{d}^2 n}{\mathrm{d}\lambda^2} = -\frac{2\pi\, c_0}{\lambda^2}\frac{\mathrm{d}^2\beta}{\mathrm{d}\omega^2}. \tag{2.29}$$

$\beta$ is obtained from the 1st order wave equation with perturbation approach [84]. To separate the waveguide dispersion from the material dispersion the refractive indices of the active layer and the cladding are kept constant at the values of $\lambda = 1550$ nm. In a wavelength range between 1.3 µm and 1.8 µm, the waveguide dispersion of the TE mode increases by 10 % and for the TM mode by 25 % (Fig. 2.11). The change of the waveguide dispersion is caused by the variation of the mode distribution with the wavelength resulting in a variation of the mode confinement factors with the wavelength. Hence, the effective refractive index also depends on the wavelength. Moreover, the mode confinement of the active region is an important parameter for the dispersion as it is elaborated in Sec. 2.3.3. The mode confinement has been calculated with the method presented in [85]. According to the solution of Eq. 2.28 the TE mode is due to the higher mode confinement the preferred mode for nonlinear applications. For this reason, all further investigations are done for the TE mode.

### 2.3.2. Material Dispersion

The material dispersion of each bulk material can also be calculated from the second derivation of its refractive index that changes due to the material properties with the wavelength (Eq. 2.29). The refractive indices for the two bulk materials, the waveguide is build of, are shown in Fig. 2.12a). In contrast with the refractive index of the active InGaAsP material, the wavelength region of interest for the cladding material is far away from its band gap. Hence, the Sellmeier equation can be used to calculate the dependence of

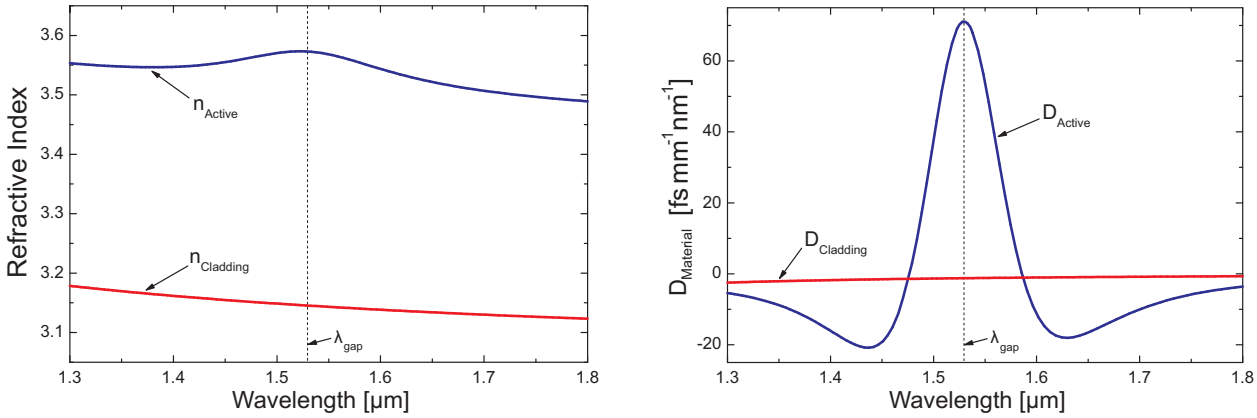


Figure 2.12.: Refractive index a) and material dispersion b) for the two bulk materials, the buried active waveguide is build of; the maximum of the active region's refractive index and the maximum of the active region's material dispersion are located at the band gap wavelength ($\lambda_{gap} = 1530\,\text{nm}$)

the refractive index on the wavelength [86]. For the active InGaAsP material composition of $y = 0.88$ and $x = 0.31$, no measurement or approximation of the refractive index around the band gap could be found in literature. Since InGaAsP is a composition of binary materials and for these binaries, measurements of the refractive index around the band gap are available, the Vegard's rule is used to calculate the refractive index of the active region [87]. For further details concerning the calculation of the refractive index of $In_{1-x}Ga_xAs_yP_{1-y}$, see Sec. D of the appendix.

Fig. 2.12b) shows the material dispersion of each bulk material calculated with the help of Eq. 2.29 from the corresponding refractive indices in Fig. 2.12a). Compared to the cladding layer, the dispersion of the active region dominates in a range of 400 nm around the band gap wavelength.

### 2.3.3. Total Chromatic Dispersion

In a first approximation, mainly material and waveguide dispersion contribute to the overall chromatic dispersion while effects like profile dispersion can be neglected since the considered waveguide is a single mode waveguide with low refractive index contrast.

To determine the contribution of the material dispersion to the overall chromatic dispersion, the composite material dispersion (CMD) is calculated with the help of the mode confinement from each material dispersion. CMD weights the material dispersion of each bulk material used in the waveguide with its mode confinement factor (Eq. 2.24):

$$D_{\text{CMD}} = \Gamma D_{\text{Active}} + (1-\Gamma) D_{\text{Cladding}} \tag{2.30}$$

Since $\Gamma \approx (1-\Gamma)$ and $|D_{\text{Active}}| \gg |D_{\text{Cladding}}|$, CMD is dominated by the contribution of the active region in the wavelength range of 400 nm around the band gap (Fig. 2.13).

When calculating CMD for the investigated active waveguide and adding the simulation results of the waveguide dispersion, an estimation of the overall chromatic dispersion can be obtained. The overall chromatic dispersion ($D_{\text{Total}}$) can also be calculated, when the wavelength dependence of the refractive index due to the material properties is included to the calculation of the waveguide dispersion (1st order wave equation with perturbation approach). The difference between the estimated and the overall chromatic dispersion can be ascribed to the residual dispersion including effects like profile dispersion [88].

### 2.3.4. Dependence on Carrier Density and Temperature

The dependence of the carrier density in the active region and the lattice temperature on the chromatic dispersion is calculated with the help of the Kramers-Kronig relation. As mentioned in Sec. 2.1.4, because

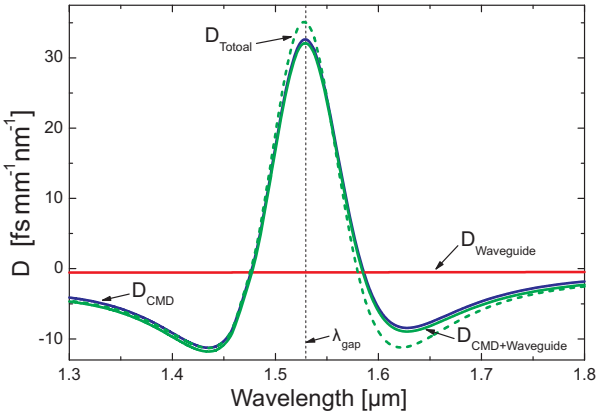


Figure 2.13.: Composite material dispersion (CMD) and waveguide dispersion for the investigated bulk active region waveguide; the sum of both approximates the overall chromatic dispersion ($D_{\mathrm{Total}}$); the maxima of the CMD and the total dispersion are located at the band gap wavelength ($\lambda_{\mathrm{gap}} = 1530\,\mathrm{nm}$)

of the demands on the gain model, the change of the material dispersion due to a carrier density or temperature change is calculated. Since, the derivation in Eq. 2.29 is a linear operation, the change of the material dispersion can be directly calculated from the change of the refractive index that has been calculated in Fig. 2.9. Because CMD is dominated by the contribution of the active region ($D_{\mathrm{CMD}} \approx \Gamma D_{\mathrm{Active}}$), only the change of the material dispersion for the active region is calculated. Assuming that the total dispersion in Fig. 2.13 is estimated for 300 K and a carrier density around the transparency (approximately $1.1\,10^{24}\,\mathrm{m}^{-3}$), the dispersion as a function of the carrier density and the temperature can be approximated with:

$$D(300\,\mathrm{K}+\Delta T, 1.1\,10^{24}\,\mathrm{m}^{-3}+\Delta N) \approx D_{\mathrm{Active}} + \Delta\Gamma\,\Delta D_{\mathrm{Material}}(\Delta T, \Delta N) + D_{\mathrm{Waveguide}}(\Delta T, \Delta N) \quad (2.31)$$

Fig. 2.14 shows the change of the active region's material dispersion due to $\Delta N$ and $\Delta T$. Both figures

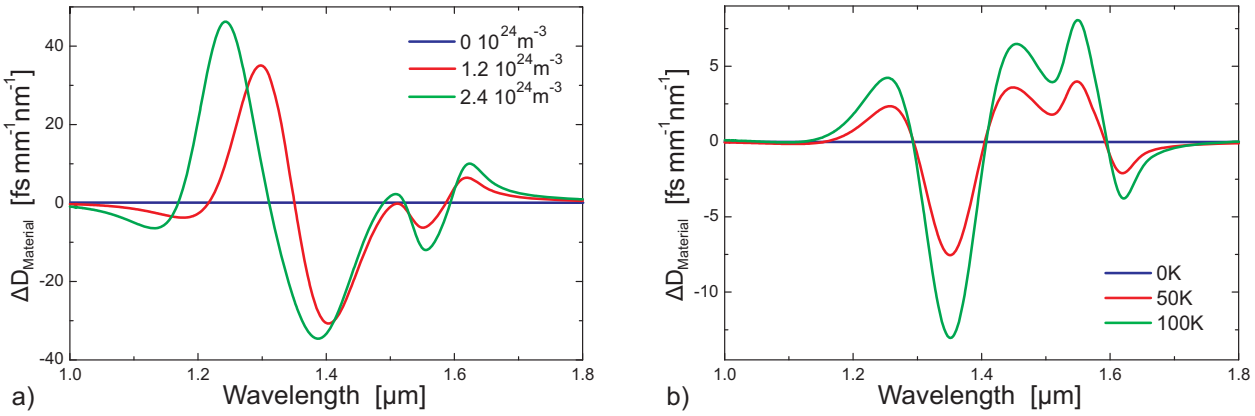


Figure 2.14.: Change of the material dispersion of the active region due to $\Delta N$ a) and $\Delta T$ b); $N_{\mathrm{ref}} = 1.1\,10^{24}\,\mathrm{m}^{-3}$ and $T_{\mathrm{ref}} = 300\,\mathrm{K}$

can be divided into two regimes where the change of the dispersion is due to different reasons. For wavelengths smaller than 1.5 µm, the change of the dispersion can be related to the dependence of the gain peak on $\Delta N$ and $\Delta T$. For wavelengths larger than 1.5 µm, the change of the dispersion is due to band gap shrinkage and the lineshape function. Moreover, this dispersion change strongly depends on the kind of lineshape function used for the gain model. For the calculations, $\Delta N$ and $\Delta T$ are chosen to cover the operation range of UL-SOAs. Due to a smaller gain change with $\Delta T$ than with $\Delta N$, the dependence of the temperature on the material dispersion is also smaller than on the carrier density. Furthermore, the material dispersion over the total wavelength range (integral of the curve) increases with increasing

carrier density and decreases with increasing temperature which can be related to a similar gain behaviour where the gain peak increases for increasing $\Delta N$ and decreases for increasing $\Delta T$. Similar to the shift of the gain peak with a carrier density change, the shift of the material dispersion with a changing carrier density can also be observed. The shift of the gain peak as well as the shift of the material dispersion are over a similar wavelength difference for the same carrier density change.

To calculate the influence of the carrier density and the temperature on the waveguide dispersion, according to [80] the refractive indices have been changed in the simulation. For the carrier density dependence only the refractive index of the active region has been adjusted while for the lattice temperature dependence the refractive index of the cladding has also been adjusted. Although $\Delta n_{\text{active}}(N + 1.2\,10^{24}\,\text{m}^{-3}) \approx \Delta n_{\text{active}}(T + 50\,\text{K})$, the change of the waveguide dispersion is smaller for $\Delta T$ than for $\Delta N$ (Fig. 2.15 a)) because the refractive index contrast remains nearly unchanged for $\Delta T$ while for $\Delta N$ the refractive index contrast increases. Even though the dependence of the temperature and the carrier

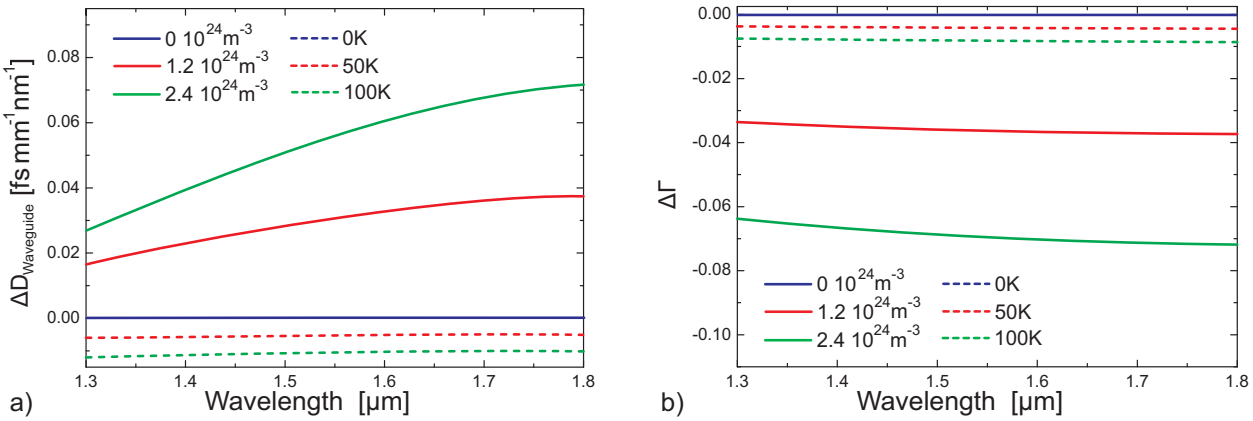


Figure 2.15.: Change of the waveguide dispersion a) and the change of active region's mode confinement b) due to $\Delta N$ and $\Delta T$; with increasing carrier density only the refractive index of the active region decreases while for an increasing temperature, the refractive index in all waveguide regions increases; $N_{\text{ref}} = 1.1\,10^{24}\,\text{m}^{-3}$ and $T_{\text{ref}} = 300\,\text{K}$

density for the waveguide dispersion is negligible compared to the change of the material dispersion, the changing refractive index contrast affects the mode distribution inside the waveguide. As a result the mode confinement changes which in turn influences the CMD. Fig. 2.15 b) shows the change of the mode confinement of the active region due to $\Delta N$ and $\Delta T$.

### 2.3.5. Consequences for Applications

Chromatic dispersion is an important effect when investigating the propagation of short pulses and efficient FWM generation. Due to the different propagation velocities of the wavelengths, pulses blur and the phase walk-off of the FWM seed modes reduces the creation of FWM products.

To estimate the influence on the pulse propagation, a typical rule of thumb for telecommunication applications is the dispersion length. The dispersion length is the length of propagation up to which a gaussian pulses broadens to twice of its original pulsewidth

$$L_D = \frac{2\pi c_0}{\lambda^2}\frac{\tau_0^2}{|D|} \tag{2.32}$$

where $\tau_0$ is half of the pulsewidth. For the 8 mm-long UL-SOA (Sec. B.3), the dispersion length becomes longer than 8 mm for pulsewidth shorter than 1.1 ps. Hence, baud rate of approximately 1 T sample/s could be used for transmitting data without intra-channel crosstalk.

For efficient FWM, the phase-matching condition of the two seed signals has to be fulfilled [89]

$$c_0 |D| \frac{\Omega^2}{\omega^2_{\text{center}}} L \ll 1 \tag{2.33}$$

where $L$ is the waveguide length and $\Omega$ the frequency detuning of the seed signals. Assuming that 0.1 is the limit for being much less than 1, a value for the input signals' detuning of 250 GHz around a input wavelength of 1550 nm can be appraised for the same device.

# 3. Nonlinear Optics in UL-SOAs

When considering the propagation of light inside an UL-SOA, it is important to note that UL-SOAs are nonlinear devices. In linear optics, only the photons are influenced by the medium of the device they are propagating in. However, in nonlinear optics, the material is also affected by the photons and this feedback is what causes the nonlinear properties of the UL-SOAs.

## 3.1. Time-Domain Modelling of UL-SOAs

In Sec. 2.1.3 and Sec. 2.1.4, it has been presented that the gain and phase dynamics are important effects in active semiconductors that provide several applications with UL-SOAs. In Sec. 2.3.5, it has been demonstrated, that chromatic dispersion does not seem to be relevant for applications being presented in Chap. 4 and Chap. 5. For this reason, chromatic dispersion is not implemented in the model. The model presented in this section is implemented in such a way that it accounts for the gain and phase dynamics and represents their influences on the optical signals precisely. Moreover, the carrier density inside the UL-SOA varies over a broad range also being an important aspect when modelling UL-SOAs. For this reason, the gain model used for the simulation also needs to account for carrier density variation.

### 3.1.1. Modelling Concept

The UL-SOA is divided into segments with the length corresponding to the sampling interval of the input signals $\Delta t = \Delta z / v_{\mathrm{G}}$. In these tiny segments the properties of the semiconductor material are assumed to be spatially independent. The flowchart in Fig. 3.1 illustrates the interaction between the electric field and the semiconductor material. To include fibre coupling loss $L_{\mathrm{coup}}$ at the facets, the optical signal is

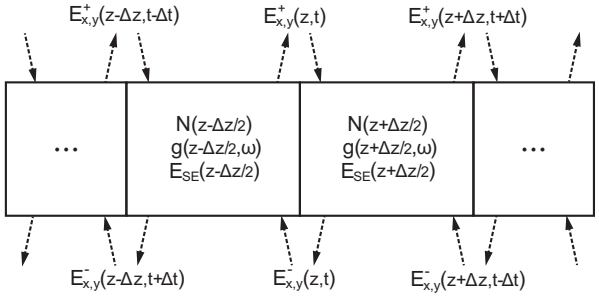


Figure 3.1.: Schematic description of the modelling concept; the SOA is divided into longitudinal segments corresponding to the sampling time of the input signal; the signal $E$ propagates trough the SOA and interacts at each segment with the nonlinear medium represented by the carrier density $N$, the gain $g$ and the spontaneous emission $E_{SE}$, the index $x, y$ denotes the polarisation axis and the superscript $\pm$ denotes the forward and backward travelling field, respectively

attenuated before it enters the first segment and after exiting the last segment.

When using time-domain modelling, the calculation of the wavelength dependent gain is complicated because the frequency components of the signals are unknown. The problem can be solved with adaptive FIR filters modelling the wavelength dependent gain in each segment of the UL-SOA [37, 38]. To update the carrier density and the gain suppressions of each SOA segment after each propagation step, the rate equations Eq. 2.12 and Eqs. 2.14 are used. For this reason, the gain of the signal's wavelength corresponding to the sampling point in the SOA segment is needed. Since the wavelength of the signal wavelength is

unknown when using the FIR concept, the gain corresponding to the wavelength is calculated with the solution of the Eq. 2.28

$$g\left(z+\frac{\Delta z}{2}\right)=\frac{\frac{\ln\left(\frac{S^{+}_{x,y}(z+\Delta z,t+\Delta t)}{S^{+}_{x,y}(z,t)}\right)}{\Delta z}+\alpha_{\text{int}}}{\Gamma}+\frac{\frac{\ln\left(\frac{S^{-}_{x,y}(z,t)}{S^{-}_{x,y}(z+\Delta z,t-\Delta t)}\right)}{\Delta z}+\alpha_{\text{int}}}{\Gamma} \tag{3.1}$$

where the index $x,y$ denotes the polarisation axis and the superscript $\pm$ denotes the forward and backward travelling field. The photon density between two segment is calculated

$$S(z,t)=\frac{1}{\kappa}\left(\left|E^{+}_{x}(z,t)\right|^{2}+\left|E^{-}_{x}(z,t)\right|^{2}+\left|E^{+}_{y}(z,t)\right|^{2}+\left|E^{-}_{y}(z,t)\right|^{2}\right) \tag{3.2}$$

with $\kappa=\hbar\omega\frac{w\cdot d}{\Gamma}v_{G}$ being the conversion factor between the photon density and the optical power.

To avoid under sampling of the signals, difference signals are used for the propagation in the UL-SOA ($\Delta\omega=\omega-\omega_{0}$ with $\omega_{0}$ being the reference frequency). The best approximation of the FIR filters to the gain model will be around the reference frequency. The FIR filters will be of first order so the propagation equation for the signals can be written as [1]:

$$\begin{aligned}E^{\pm}_{x,y}(z\pm\Delta z,t+\Delta t)=\Bigg[&c_{1}\left(z\pm\frac{\Delta z}{2},t\right)E^{\pm}_{x,y}(z,t)+c_{2}\left(z\pm\frac{\Delta z}{2},t\right)\\&\cdot E^{\pm}_{x,y}(z,t-\Delta t)\exp\left(-i\omega_{0}\Delta t\right)\Bigg]\exp\left(i\Delta\phi\right)+E^{\pm}_{\text{SE}\,x,y}\left(z\pm\frac{\Delta z}{2},t\right)\end{aligned} \tag{3.3}$$

$E^{\pm}_{\text{SE}\,x,y}$ is the contribution of the spontaneous emission (SE) of each SOA segment to the propagating field [39, 90]:

$$E^{\pm}_{\text{SE}\,x,y}\left(z\pm\frac{\Delta z}{2},t\right)=\sqrt{\hbar\omega\,\Gamma\,g_{\text{peak}}\,n_{\text{sp}}\frac{\Delta z}{\Delta t}}\,\frac{x_{1}+ix_{2}}{\sqrt{2}} \tag{3.4}$$

with $x_{1}$ and $x_{2}$ being numerically generated independently and uniformly distributed in frequency-domain (white noise) with a standard normal distributed probability. $n_{\text{sp}}$ is the spontaneous emission rate

$$n_{\text{sp}}=\left(1-\exp\left(-\frac{\hbar\,C_{\omega}\left(N-N_{\text{tr}}\right)}{k_{B}T}\right)\right)^{-1} \tag{3.5}$$

with $C_{\omega}$ being the peak frequency shift coefficient (Tab. B.2).

The noise source in this model is a white noise source getting the spectral shape of ASE due to the convolution with the material gain of each SOA segment when propagating with the signal through the UL-SOA.

To model with the FIR filter approach an UL-SOA, the filter coefficients have to be set in order to represent the wavelength dependent gain with the spectral shape of the FIR filter. Since the properties of the UL-SOA vary, which can be implemented with Eq. 2.12, Eqs. 2.14 and Eq. 2.18, the filter coefficients have to be adapted in each segment. The calculation for the filter coefficients is presented in Sec. E. In order to reduce the calculation complexity of the UL-SOA model, the adaption of the filter coefficients should be as simple as possible. Moreover, a closed solution is preferred so the gain model in Sec. 2.1 cannot be used. Instead in the following section a simpler gain model is presented based on a polynomial fit.

[1] It is convenient that the propagating field is a pseudo-electric field which can be directly related to the optical power $|E|^{2}=P$ [25, 33, 38].

### 3.1.2. Spectral Gain Approximation

In [38] the wavelength dependent gain is fitted to a parabolic gain model which is only accurate for high carrier densities around the gain peak. Since in short SOAs the carrier density is nearly constant and the input signals enter the SOA around the gain peak wavelength, the parabolic gain approximation can be used. In UL-SOAs the carrier density is high in the amplifying section and low in the saturated section resulting in a shift of the gain peak by approximately 30 nm. Hence, the parabolic gain approximation cannot be used. A cubic parametrisation was given in [28] accurately describing the material gain over a broad bandwidth for various carrier densities. Unfortunately, this model does not properly represent the gain spectrum for carrier densities close to the material transparency. Fig. 3.2 shows that there is still

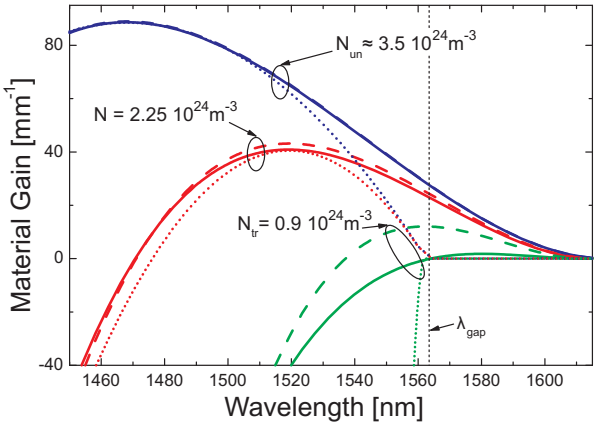


Figure 3.2.: Spectrum of the linear material gain as a function of the wavelength for different carrier densities according to Tab. B.2; dotted lines: parabolic gain approximation [38], dashed lines: cubic gain approximation [28], solid lines: advanced cubic gain approximation; the cubic gain approximation [28] is greater than 0 for $N = N_{tr}$ around $\lambda_{peak}$

positive gain around $\lambda_{gap}$ for the transparency carrier density $N_{tr}$ which can be a problem for modelling UL-SOAs since most of the device is saturated. Since except for this problem, the cubic gain model matches very well with measurements of the material gain of InGaAsP semiconductors with $\lambda_{gap}$ of approximately of 1550 nm [28], only two additional boundary conditions are defined in order to resolve this problem:

$$g_{cub}(\omega_{gap}, N_{tr}) \simeq 0 \qquad \text{and} \qquad \left.\frac{\mathrm{d}\, g_{cub}(N_{tr})}{\mathrm{d}\,\omega}\right|_{\omega<\omega_{gap}} \approx 0 \tag{3.6}$$

These two boundary conditions can be included to the model when creating two additional degrees of freedom by extending the cubic gain model from [28] with two further parameters. The advanced cubic gain model is

$$g_{cub}(\omega) = \begin{cases} 3\, g_{peak\,2}\left(\frac{\omega-\omega_z}{\omega_z-\omega_{peak\,2}}\right)^2 + 2\, g_{peak\,3}\left(\frac{\omega-\omega_z}{\omega_z-\omega_{peak\,3}}\right)^3 & \text{if} \quad \omega > \omega_z \\ 0 & \text{if} \quad \omega \le \omega_z \end{cases} \tag{3.7}$$

with

$$g_{peak\,2} = \frac{\mathrm{d}g}{\mathrm{d}N}\left(N - N_{tr}\right) + \bar{a}\,\frac{\mathrm{d}g}{\mathrm{d}N} N_{tr} \exp\left(-\frac{N}{N_{tr}}\right) \tag{3.8a}$$

$$g_{peak\,3} = \frac{\mathrm{d}g}{\mathrm{d}N}\left(N - N_{tr}\right) + \frac{\mathrm{d}g}{\mathrm{d}N} N_{tr} \exp\left(-\frac{N}{N_{tr}}\right) \tag{3.8b}$$

$$\omega_{peak\,2} = \omega_{gap} + C_\omega\left(N - N_{tr}\right) + \bar{b}\,\omega_{shift} \exp\left(-\frac{N}{N_{tr}}\right) \tag{3.8c}$$

$$\omega_{\text{peak}\,3} = \omega_{\text{gap}} + C_{\omega}\left(N - N_{\text{tr}}\right) + \omega_{\text{shift}} \exp\left(-\frac{N}{N_{\text{tr}}}\right) \tag{3.8d}$$

$$\omega_{z} = \omega_{z0} + z_{0}\left(N - N_{\text{tr}}\right) \tag{3.8e}$$

The explanations of the variables are given in Tab. B.2. For a better understanding Fig. 3.3 illustrates that

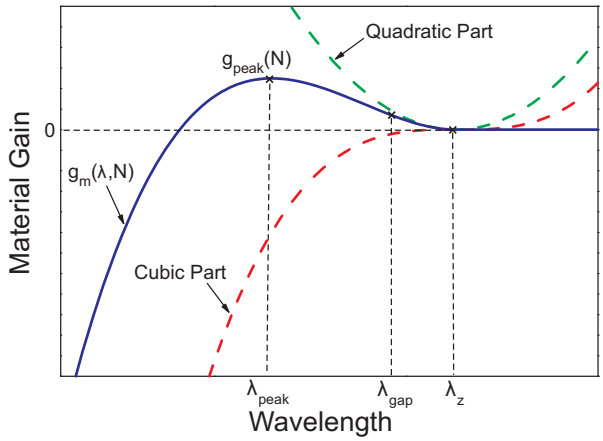


Figure 3.3.: Schematic description of the material gain model constructed by a quadratic and a cubic polynomial term; the gain starts to be zero for $\lambda > \lambda_z > \lambda_{\text{gap}}$ because of the spectral lineshape function caused by the carrier relaxation time

the gain model consists of a parabolic and a cubic polynomial term. The idea behind the modifications of the advanced cubic gain model is to make sure that the cubic part of the polynomial in Eq. 3.7 dominates for low carrier densities. Therefore, the exponential terms in Eq. 3.8a and Eq. 3.8c that dominate for low $N$ are weighted with $\bar{a} < 1$ and $\bar{b} < 1$. For $N \gg N_{\text{tr}}$ the exponential terms of Eqs. 3.8 vanish and the cubic gain model from [28] and the gain model presented here become equal. As a result, the advanced cubic gain model represents the material gain over a broad bandwidth for $N \geq N_{\text{tr}}$ accurately, even at low carrier densities (Fig. 3.2).

How to implement the gain model in the FIR filter simulation model from Sec. 3.1.1 is presented in Sec. E of the appendix.

## 3.2. Properties of UL-SOAs

The purpose of UL-SOAs is to benefit from the semiconductor's fast nonlinear intraband effects while slow interband effects should be suppressed as far as possible, in order to avoid bit pattern effects in applications.

When driving an UL-SOA in the gain regime, the optical input signal is amplified. Eq. 2.12 implies that with increasing photon density, the carrier density is reduced due to stimulated emission. For this reason, the main part of UL-SOAs is saturated by the amplified signals and the amplified spontaneous emission (ASE) noise after a certain length. Hence, UL-SOAs can be regarded as being divided into an amplifying section and a saturated section (blue line in Fig 3.4). For bulk SOAs with typical dimensions the transition between these sections takes place after approximately 1 mm of propagation. If no input signals enter the UL-SOA, the carrier density peaks shifts to the middle of the device because of equal optical power of the forward and backward travelling ASE (red line in Fig 3.4). The amplifying section has the same properties as a short SOA and the saturated section can be regarded as another device with different properties. Because of the high optical power after the amplifying section, the carrier density in the saturated section is fixed to the net transparency level $N_{\text{sat}}$. From the propagation equation (Eq. 2.28) the net transparency level can be obtained as a result of the equilibrium between modal gain and losses

$$0 \stackrel{!}{=} \Gamma g_{\text{sat}} - \alpha_{\text{int}} \approx \Gamma \frac{\mathrm{d}g}{\mathrm{d}N}\left(N_{\text{sat}} - N_{\text{tr}}\right) - \alpha_{\text{int}}. \tag{3.9}$$

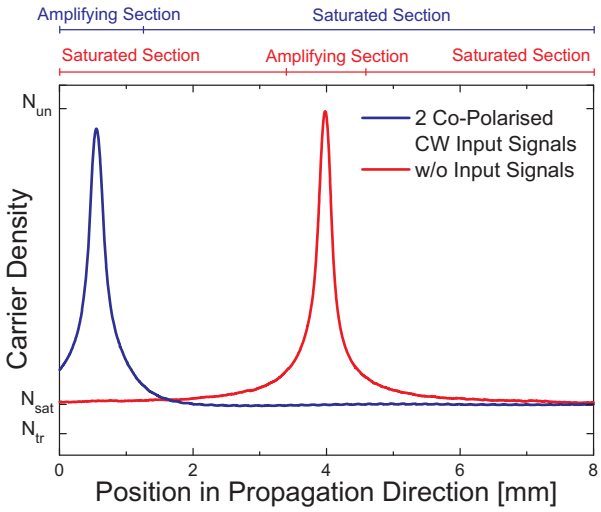


Figure 3.4.: Simulated carrier density of the 8 mm-long UL-SOA (Sec. B.3) along the propagation-direction; due to two co-polarised CW input signals (8.5 dBm at 1555 nm and 8.5 dBm at 1560 nm) the carrier density peak is shifted towards the UL-SOA's front; ($N_{tr}$ = material transparency level, $N_{sat}$ = net transparency level, $N_{un}$ = unsaturated level)

Since the amount of the $g_{CDP}$ is much bigger than the contribution to the gain due to the fast intraband effects (as it will be demonstrated in Sec. 3.3.2 Fig. 3.6a)), the approximation in Eq. 3.9 can be made for some analytic estimations (Sec. 3.4 and Sec. F).

If the signal levels change much faster than the carrier lifetime, the carrier density in the amplifying section is only dependent on the average optical power. If the signal remains at one of the states longer than the carrier lifetime, the length and the gain of the amplifying section changes as it is indicated in Fig. 3.4. As a result bit pattern effects occur in applications. For high data rates with fast changing signal states, the performance is not limited by the slow interband effects. Only the fast nonlinear intraband effects affect the signals in the saturated section. Their response time is about 1000-times shorter compared to the slow interband effects, but their impact is also weaker. For this reason, UL-SOAs have lengths of several millimetres.

## 3.3. Nonlinear Optics in UL-SOAs

Due to the nonlinear optical effects in semiconductors a huge variety of all-optical signal processing applications are possible. This section presents the most important nonlinear optical effects needed for this thesis.

The nonlinear optical effects in UL-SOAs are caused by the variation in the intensities of the propagating signals. If there are multiple signals propagating inside the UL-SOA, the optical polarisation becomes important because beating signals cause further variations in the intensity. The photon density for two parallel polarised CW signals [2] at a fixed spatial position can be written as

$$\begin{aligned} S &= \frac{1}{\kappa}\left|E_{\text{pump}}\exp\left(i\omega_{\text{pump}}t\right)+E_{\text{probe}}\exp\left(i\omega_{\text{probe}}t\right)\right|^2 \\ &= \underbrace{S_{\text{pump}}+S_{\text{probe}}}_{\text{static}}+\underbrace{\frac{1}{\kappa}\left(E_{\text{pump}}E^*_{\text{probe}}\exp\left(i\Omega t\right)+c.c.\right)}_{\text{dynamic}} \end{aligned} \tag{3.10}$$

with $\Omega = \omega_{\text{pump}} - \omega_{\text{probe}}$ being the difference frequency of the CW signals. Hence, the nonlinear optical effects can be separated into two groups: static and dynamic effects (Eq. 3.10). To enable the dynamic effects the polarisation of the signals has to be parallel.

[2] According to Sec. 2.1.2, the stronger CW signal is named pump and the weaker CW signal is the probe.

### 3.3.1. Static Effects

Since the applications in Chap. 4 and Chap. 5 are mainly due to the dynamic effects, the static effects are only briefly presented in this subsection.

There are two main kinds of static effects: effects that are caused by the signal that is affected (self-gain modulation (SGM) and SPM) and effects that are caused by other signals than they are affecting (XGM and XPM). Both categories of static effects are caused due to the dependence of the interband and intraband effects on the photon density. As a result, the gain and the refractive index of the active semiconductor is directly modulated by the amplitude of the signals (Eq. 2.12, Eqs. 2.14 and Eq. 2.17).

With increasing photon density, the slow interband effects as well as the fast intraband effects are gain suppressing (Eq. 2.12 and Eqs. 2.14). The transfer characteristic (Fig. 3.5) of an UL-SOA is nonlinear so

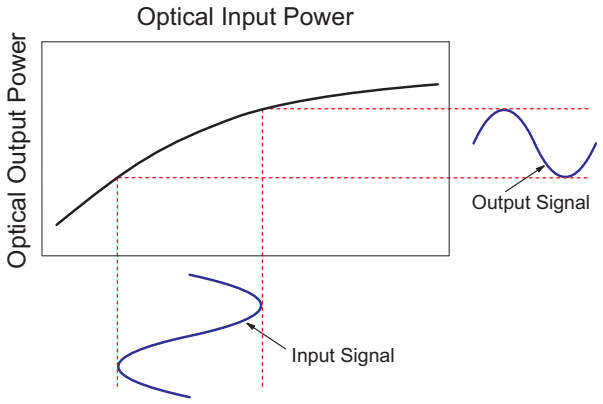


Figure 3.5.: Transfer characteristic ($|E_{out}|^2$ over $|E_{in}|^2$) of an UL-SOA for a single input signal; due to the gain suppressing mechanisms, the optical output power saturates with increasing optical input power

because of SGM e.g., noise compression of a data signal's "1"-level is possible [91, 92]. With the help of XGM another signal can be intensity modulated so e.g., AOWC can be obtained with SOAs [2, 93].

In Sec. 2.1.4, it has been presented that in active semiconductors a gain change always affects the phase of propagating signals. With these phase modulations also all-optical signal processing is possible. For instance an application of SPM is chirp compensation [94] and due to XPM wavelength conversion can be achieved [2, 43].

### 3.3.2. Dynamic Effects

In addition to the static effects, multiple co-polarised signals create dynamic index and gain gratings in the UL-SOA's saturated section due to the signals' beating (Fig. 3.6). These dynamic gratings are also caused by the dependence of the interband and intraband effects on the photon density. At these dynamic gratings, the signals interact and cause dynamic effects like FWM and a Bogatov-like effect. Due to the high signals' power in the saturated section and the short relaxation times of the intraband effects, the dynamic effects can take place over several nanometres. Since there are three main gain and index mechanism (CDP, CH and SHB) and each mechanism has another relaxation time constant, their contribution to the dynamic effects hold for different bandwidths of the detuning frequency [89].

#### Four-Wave Mixing

FWM is a dynamic nonlinear optical effect that creates new sidebands in the spectrum because of the beating signal. In time-domain, the dynamic gratings cause an amplitude and phase modulation thus creating, in frequency-domain, new spectral components with a wavelength spacing corresponding to the beating frequency. These new spectral components are called FWM products.

In order to make the name of this nonlinear optical effect more clear and to give a better understanding for some definitions related to FWM, the electric polarisation has to be investigated more in detail.

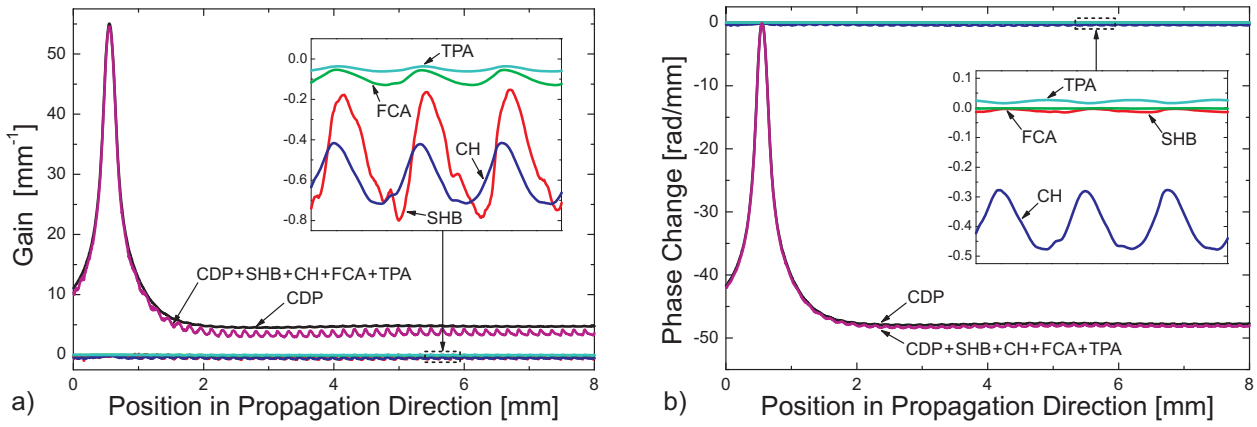


Figure 3.6.: Dynamic gain grating a) and dynamic index grating b) inside the 8 mm-long UL-SOA (Sec. B.3) along the propagation direction due to the beating of the same two co-polarised CW signals from Fig. 3.4; the pulsation frequency is the difference frequency of the two input signals

Equating the susceptibility in Eq.2.21 with Eq. 2.22, the electric polarisation can be separated into a background polarisation $\vec{P}_0$ and a term for the resonant nonlinearities $\vec{P}_{\mathrm{NL}}$. Developing $\chi_{\mathrm{NL}}$ with the Taylor approximation [3] [95] and neglecting the even order terms due to the inversion symmetry of the semiconductor lattice, the nonlinear electric polarisation up to a tensor order of three is

$$\vec{P}_{\mathrm{NL,n}} = \epsilon_0 \left( \chi_n^1 \cdot \vec{E}_n + \sum_{i,j,k} \chi^3_{n,i,j,k}(\omega_n : \omega_i, -\omega_j, \omega_k) \vec{E}_i \vec{E}_j^* \vec{E}_k \right). \tag{3.11}$$

The name FWM is due to the 3rd order susceptibility where up to four signals are involved. The frequency and the phase of the new FWM product can be calculated with

$$\omega_n = \omega_i - \omega_j + \omega_k \qquad \text{and} \qquad \phi_n = \phi_i - \phi_j + \phi_k. \tag{3.12}$$

To obtain a high efficiency of the FWM process, the phase matching condition has to be fulfilled

$$\Delta k = k_i - k_j + k_k - k_n \stackrel{!}{=} 0 \tag{3.13}$$

from which Eq. 2.33 can be obtained. In Sec. 2.3.5 it has been demonstrated that the phase walk-off caused by chromatic dispersion is negligible for the investigated 8 mm-long UL-SOA (Sec. B.3). For this reason, chromatic dispersion has not been implemented in the simulation model so the phase matching condition (Eq. 3.13) is always fulfilled for the simulations.

Typically, it is distinguished between non-degenerated FWM ($i \neq j \neq k$) and degenerated FWM ($i = k \neq j$). As it is demonstrated at the end of this subsection, multi-wave mixing (MWM) also occurs in UL-SOAs where more than four frequencies are involved in the generation of new spectral components. In order to consider these MWM processes, odd higher order tensors have to be included into Eq. 3.11.

### Bogatov-like Effect

The Bogatov-like effect is part of FWM and describes how the new frequency components, generated by the dynamic gain and index gratings, affect the signals at the input frequencies. When describing the effect with the 3rd order nonlinear susceptibility, the indices of the frequencies have to be $i = j \neq k$ [29].

[3] Since active semiconductor media are resonant, the susceptibility is strongly dependent on the electric field and the carrier density distribution $\chi_{\mathrm{NL}}(\vec{E}, \rho)$. For this reason, the expansion can only be done if the input signals are CW signals and the perturbation due to the dynamic part of Eq. 3.10 is small. As a result, the susceptibility can be assumed to be static and the expansion can be used for some principal calculations and explanations [96].

In [97], Bogatov has presented a parametric amplification in nonlinear semiconductor media. Due to the dynamic gain and index gratings, the amplification of the weaker signal (probe) is dependent on the power and the frequency detuning of the stronger signal (pump). Different from [97], in UL-SOAs the effect is dominated by the fast intraband effects in the UL-SOA's saturated section. This so called Bogatov-like effect can be described analytically

$$\Delta g_{\mathrm{SHB}}^{\mathrm{probe}}(\Omega, P_{\mathrm{pump}}) = g_{\mathrm{sat}}\,\epsilon_{\mathrm{SHB}}\frac{P_{\mathrm{pump}}}{\kappa}\,\frac{\alpha_{\mathrm{SHB}}\,\tau_{\mathrm{SHB}}\Omega - 1}{\left(\tau_{\mathrm{SHB}}\Omega\right)^2 + 1} \tag{3.14a}$$

$$\Delta g_{\mathrm{CH}}^{\mathrm{probe}}(\Omega, P_{\mathrm{pump}}) = g_{\mathrm{sat}}\,\epsilon_{\mathrm{CH}}\frac{P_{\mathrm{pump}}}{\kappa}\,\frac{\alpha_{\mathrm{CH}}\,\tau_{\mathrm{CH}}\Omega - 1}{\left(\tau_{\mathrm{CH}}\Omega\right)^2 + 1} \tag{3.14b}$$

$$\Delta g_{\mathrm{FCA}}^{\mathrm{probe}}(\Omega, P_{\mathrm{pump}}) = \frac{\mathrm{d}g}{\mathrm{d}N}\,\epsilon_{\mathrm{FCA}}\,N_{\mathrm{sat}}\frac{P_{\mathrm{pump}}}{\kappa}\,\frac{\alpha_{\mathrm{FCA}}\,\tau_{\mathrm{CH}}\Omega - 1}{\left(\tau_{\mathrm{CH}}\Omega\right)^2 + 1} \tag{3.14c}$$

with $g_{\mathrm{sat}} = \frac{\alpha_{\mathrm{int}}}{\Gamma}$. A detailed derivation of these equations is given in Sec. F. Each type of gain suppression contributes to the amplification asymmetry except TPA as its gain coefficient due to the dynamic gratings only affects frequencies corresponding to the FWM products. The overall gain of the probe signal can be calculated with

$$g^{\mathrm{probe}} = g(\omega_{\mathrm{probe}}) + \Delta g_{\mathrm{SHB}}^{\mathrm{probe}}(\Omega, P_{\mathrm{pump}}) + \Delta g_{\mathrm{CH}}^{\mathrm{probe}}(\Omega, P_{\mathrm{pump}}) + \Delta g_{\mathrm{FCA}}^{\mathrm{probe}}(\Omega, P_{\mathrm{pump}}). \tag{3.15}$$

To estimate the magnitude of the Bogatov-like effect in the UL-SOA's saturated section, it is appropriate to approximate $|E_{\mathrm{pump}}|^2$ with $\kappa\, S_{\mathrm{sat}}$. Fig. 3.7 shows that the probe signal's amplification is asymmetric

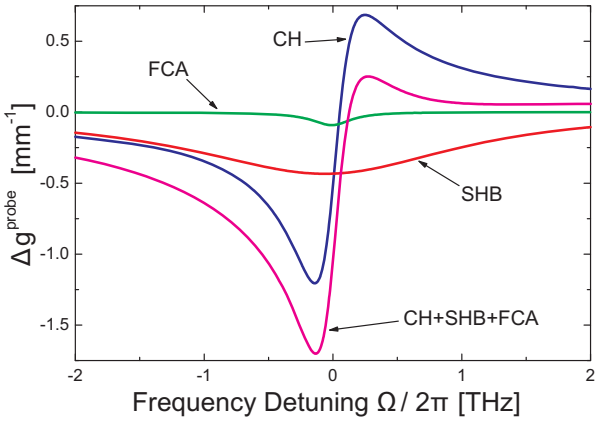


Figure 3.7.: Probe signal's gain in dependence of the frequency detuning to the pump signal due to the Bogatov-like effect in the UL-SOA's saturated section ($P_{\mathrm{pump}} \approx \kappa S_{\mathrm{sat}}$); the values for the variables in Eq. 3.14 are given in Tab. B.2

in dependence of the pump signal's frequency detuning $\Omega$. Unlike the original Bogatov effect, the amplification asymmetry can be observed over several nanometres. The reason for this are the short time constants of the fast intraband effects. With an increasing detuning the effect decreases and becomes zero for an infinite detuning. For a certain detuning a maximum gain asymmetry is observed. Similar results for the nonlinear effects in short SOAs are presented in [89].

Since the $\alpha$-factors in Eqs. 3.14 only contribute to the numerator's linear polynomial terms, they have a major influence on the asymmetry of the probe signal's amplification. E.g., the gain suppressions with a very low $\alpha$-factor (SHB and FCA) result in a nearly symmetric gain profile around the axis of $\Omega = 0$ (Fig. 3.7a)). In general the $\alpha$-factors in SOAs are positive, so due to the dynamic nonlinear gain, the probe signal is amplified for a positive frequency detuning and attenuated for a negative frequency detuning (Fig. 3.7b)).

Not only the gain of the probe signal is affected in dependence of the pump signals power and frequency detuning but also the phase:

$$\Delta\phi^{\text{probe}}_{\text{SHB}}(\Omega, P_{\text{pump}}) = g_{\text{sat}}\,\epsilon_{\text{SHB}}\frac{P_{\text{pump}}}{\kappa}\frac{\alpha_{\text{SHB}}+\tau_{\text{SHB}}\Omega}{(\tau_{\text{SHB}}\Omega)^2+1} \tag{3.16a}$$

$$\Delta\phi^{\text{probe}}_{\text{CH}}(\Omega, P_{\text{pump}}) = g_{\text{sat}}\,\epsilon_{\text{CH}}\frac{P_{\text{pump}}}{\kappa}\frac{\alpha_{\text{CH}}+\tau_{\text{CH}}\Omega}{(\tau_{\text{CH}}\Omega)^2+1} \tag{3.16b}$$

$$\Delta\phi^{\text{probe}}_{\text{FCA}}(\Omega, P_{\text{pump}}) = \frac{\mathrm{d}g}{\mathrm{d}N}\,\epsilon_{\text{FCA}}\,N_{\text{sat}}\frac{P_{\text{pump}}}{\kappa}\frac{\alpha_{\text{FCA}}+\tau_{\text{CH}}\Omega}{(\tau_{\text{CH}}\Omega)^2+1} \tag{3.16c}$$

The equations are also a result of the derivation in Sec. F. Similar to Eq. 3.15, the overall phase change of the probe signal can be calculated with

$$\Delta\phi^{\text{probe}} = \Delta\phi(\omega_{\text{probe}}) + \Delta\phi^{\text{probe}}_{\text{SHB}}(\Omega, P_{\text{pump}}) + \Delta\phi^{\text{probe}}_{\text{CH}}(\Omega, P_{\text{pump}}) + \Delta\phi^{\text{probe}}_{\text{FCA}}(\Omega, P_{\text{pump}}). \tag{3.17}$$

Fig.3.8 shows the phase change of the probe signal due to the dynamic gratings. Similar to the Bogatov-

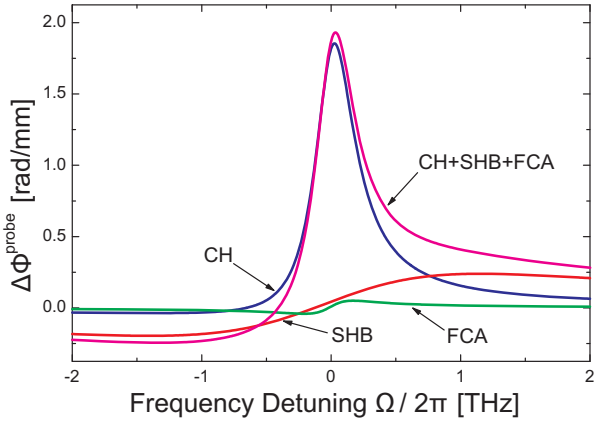


Figure 3.8.: Probe signal's phase change in dependence of the frequency detuning to the pump signal due to the Bogatov-like effect in the UL-SOA's saturated section ($P_{\text{pump}} \approx \kappa S_{\text{sat}}$); the values for the variables in Eq. 3.16 are given in Tab. B.2

like effect affecting the probe signal's gain, the effects on the phase due the SHB and FCA are nearly symmetric to a detuning of 0 because of $\alpha_{\text{SHB}} \approx 0$ and $\alpha_{\text{FCA}} \approx 0$.

### Simulating Four-Wave Mixing and the Bogatov-like effect

Fig. 3.9 shows spectra at the output of the 8 mm-long bulk UL-SOA (Sec. B.3) for two co-polarised CW input signals around three different input wavelengths. The CW input signals had wavelength spacings of 0.2 nm and were injected around 1550 nm, 1560 nm and 1565 nm, respectively.

Although only two co-polarised CW signals enter the UL-SOA, a spectrally broad mode comb can be obtained at the UL-SOA's output. The broad FWM comb is a result of cascaded FWM because the FWM products, again, interact with their neighbour modes due to the high FWM efficiency (Fig. 3.10) so the process repeats multiple times. If the two input signals are injected around the gain peak wavelength and only cascaded FWM would create the mode comb, a strictly decaying smooth shape of the comb's envelope with its maximum at the input signal's wavelength would be obtained. While the low power modes of the mode comb have this smooth decaying shape, the power of the high power modes fluctuates over several dBm compared to the neighbor modes. Moreover, a saddle point on the shorter wavelength side of the high power modes can be observed. No matter where the FWM comb is located in the gain spectrum, the saddle point is always on the shorter wavelength side of the FWM comb. Similarly,

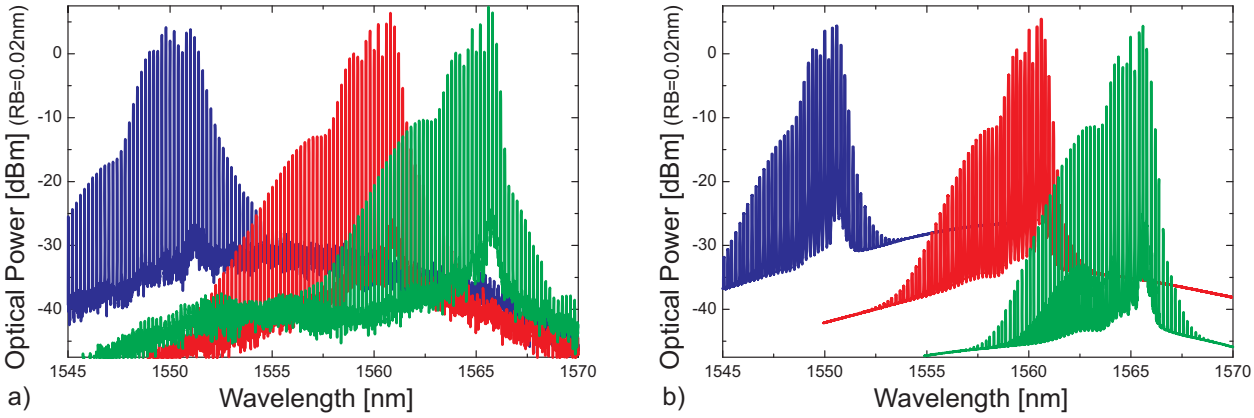


Figure 3.9.: Simulated a) and measured b) output spectra of the 8 mm-long UL-SOA (Sec. B.3), generated from two CW input signals; the two co-polarised CW input signals for the three different spectra were injected with an input power of 8.5 dBm each and a wavelength spacing of 0.2 nm around 1550 nm, 1560 nm and 1565 nm, respectively; the measurements were done by the group of B. Sartorius from the *HHI*

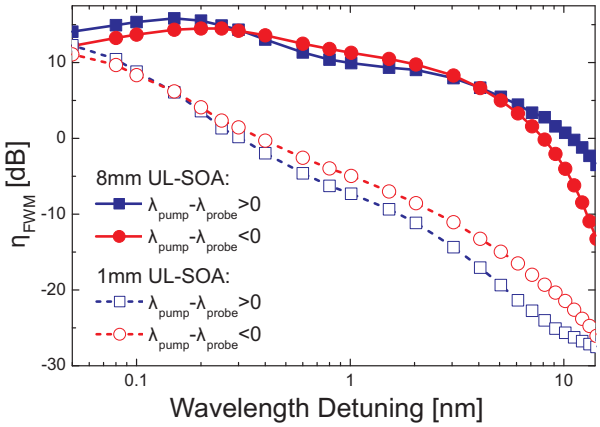


Figure 3.10.: FWM efficiency for a 1 mm-long SOA and a 8 mm-long UL-SOA with the parameters from Tab. B.2; due to the pronounced fast intraband effects, UL-SOAs have tremendous FWM efficiency for wavelength detunings greater than 0.1 nm; the input pump signal had a power of 8.5 dBm at a wavelength of 1560 nm and the probe signal a power of -1.5 dBm; $\eta_{FWM} = P_{FWM}/P_{probe}$ with $P_{FWM}$ being the power of the first FWM product on the side of the pump signal

the Bogatov-like effect attenuates modes on the shorter wavelength side of a stronger signal. For this reason, the saddle point can be ascribed to the Bogatov-like effect causing an attenuation on the shorter wavelength side. The power fluctuations can also be ascribed to the Bogatov-like effect in combination with different FWM processes interacting in opposite direction. While for the low power modes the feedback of the FWM products on the parent modes can be neglected, in the high power mode region also the feedback of the FWM products on the parent modes has to be considered. As a result, irregularities caused by the Bogatov-like effect can be carried on by different FWM processes (degenerated FWM, non-degenerated FWM and MWM) operating in opposite direction. Since the Bogatov-like effect only becomes a significant influence for high optical power, the saddle point and the modes power fluctuation are close by the high power modes.

The influence of the Bogatov-like effect on the phase can also be observed if the phase of the FWM mode is regarded. Fig. 3.11 shows the phase and the amplitude of each generated FWM mode. The phase of the FWM modes is not linear for the regime with high optical power FWM modes while on the shorter wavelength side a region with approximately 40 modes with linear phase relation can be observed. Without any Bogatov-like effect the phase relation of the FWM products would be linear (Eq. 3.12) but Fig. 3.11 depicts that the modes whose power is affected by the Bogatov-like effect also have a distorted

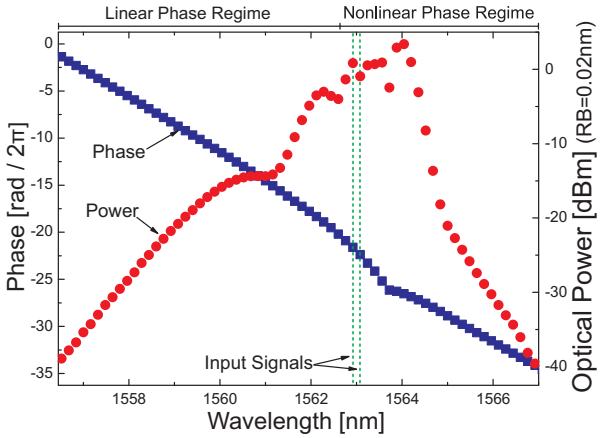


Figure 3.11.: FWM modes phase relation obtained from two co-polarised CW input signals with each 8.5 dBm of input power; the figure shows the phase and the power only at a FWM modes

phase.

Comparing the measurements and the simulations in Fig. 3.9, an excellent match can be observed. Due to the time-domain modelling, the dynamic gain and phase gratings are inherently implemented. Hence, the Bogatov-like effect and FWM in all its variates are calculated automatically. Modelling such complex interactions in frequency-domain is almost impossible, since even simple FWM processes are complicated to calculate [18].

## 3.4. Device Optimisation

In UL-SOAs, nonlinear optics is done due to the fast intraband effects in the saturated section of the UL-SOA. To improve the performance of these effects, the driving conditions and the device parameters have to be optimised. Some appropriate parameters are: the mode confinement, the differential gain, the internal loss and the driving current [4].

To optimise the performance of the UL-SOA, the efficiencies of the fast intraband effects have to be improved. The analytic represation of these intraband effects are rate equations for the gain (Eqs. 2.14). Letting one equation represent all intraband effects

$$\frac{\partial g_{\mathrm{NL}}}{\partial t} = -\frac{g_{\mathrm{NL}}}{\tau_{\mathrm{NL}}} - \frac{\epsilon_{\mathrm{NL}}}{\tau_{\mathrm{NL}}} g\, S \tag{3.18}$$

and making the change instantaneous ($\tau_{\mathrm{NL}} \to 0$), a steady state solution for the gain due to the intraband effects can be obtained [25]

$$g_{\mathrm{NL}} = -\epsilon_{\mathrm{NL}} g\, S. \tag{3.19}$$

The intraband effects affect the optical signal strongly if the interactions of the nonlinear gain $g_{\mathrm{NL}}$ in Eq. 2.28 are maximised. Since $g_{\mathrm{NL}}$ is weighted in Eq. 2.28 with $\Gamma$ and $\epsilon_{\mathrm{NL}}$ is a material constant, $\Gamma g_{\mathrm{sat}} S_{\mathrm{sat}}$ has to be maximised. The saturated photon density $S_{\mathrm{sat}}$ can be obtained from Eq. 2.12 where the contributions of TPA are neglected

$$0 \stackrel{!}{=} \frac{I}{eV} - \frac{N_{\mathrm{sat}}}{\tau_{\mathrm{CDP}}} - v_{\mathrm{G}} g_{\mathrm{sat}} S_{\mathrm{sat}}. \tag{3.20}$$

Fig. 3.12 shows the analytic results of the optimisation for a variation of the appropriate parameters. Compared to the differential gain and the internal losses, the optimisation parameter depends on the

[4] The mode confinement can be changed with the geometry of the waveguide, the differential gain depends on the device type (bulk, MQW, quantum dash or QD active region) and the internal loss can be changed with the waveguide type (ridge, v-grove or buried waveguide)

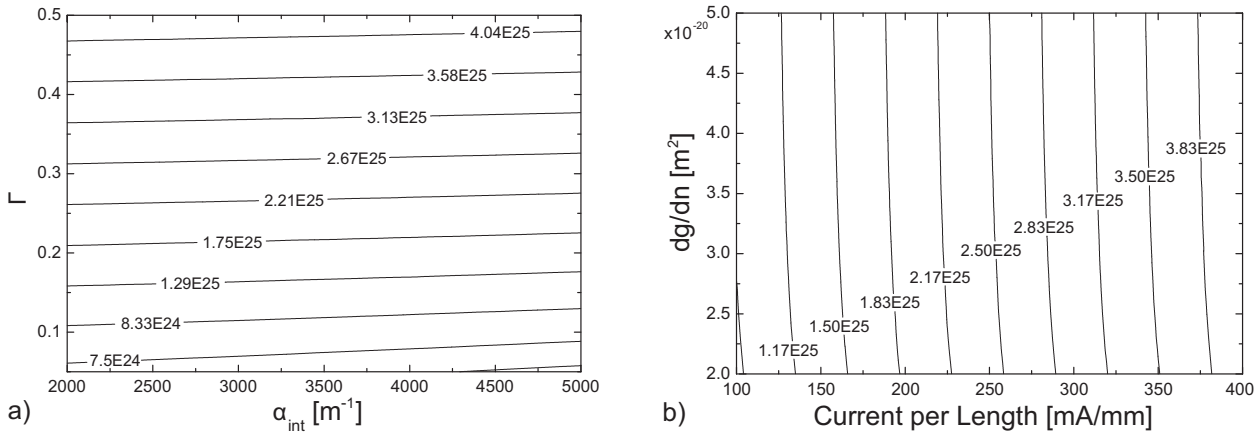


Figure 3.12.: Calculated optimisation parameter ($\Gamma g_{sat} S_{sat}$ in [$m^{-4}$]) as a function of the mode confinement, the differential gain, the internal losses and the driving current per length; the parameters are taken from Tab. B.2

mode confinement and the current per length, significantly. Hence, to improve the performance of the device, the current per length and the mode confinement should be increased. To cross-check the analytic results, full numerical simulations have been performed. As a figure of merit the number of generated modes of a FWM comb has been taken. The dependence of the number of modes on the wavelength

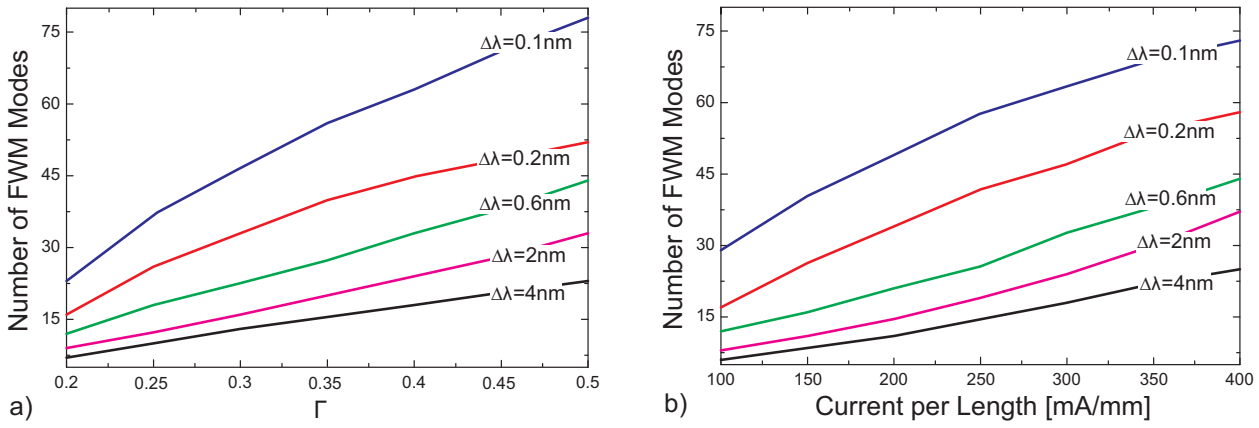


Figure 3.13.: Number of FWM modes at the output of an 8 mm-long UL-SOA in dependence of the wavelength spacing and the confinement factor a) or the current per length b); $P_{pump} = P_{probe} = 8.5$ dBm and $\lambda_{pump} = 1560$ nm; OSA resolution bandwidth = 0.02 nm

spacing and the confinement factor or the current per length is shown in Fig. 3.13. Only the modes with a minimum optical signal to noise ratio (OSNR) of 10 dB have been taken into account. As expected, the number of modes increases with increasing confinement factor and increasing current per length showing that these are important parameters for the device optimisation. Since in bulk devices larger confinement factors can be realised bulk UL-SOAs provide a better performance concerning nonlinear signal processing compared to MQW UL-SOAs. With increasing wavelength spacing, the number of modes decreases since the FWM efficiency decreases (Fig. 3.10) due to the time constants of the intraband effects (Eqs. 2.14) decreasing the amplitude of the dynamic gain and index gratings.

While the mode confinement for the 8 mm-long bulk UL-SOA (Sec. B.3) can still be increased, the driving current with 300 mA/mm is already at its maximum because of thermal heating caused by the current. Furthermore, the coupling loss at the facet should be as low as possible to saturate the UL-SOA mainly by the signal and not by ASE.

# 4. High-Speed Wavelength Conversion With Signal Regeneration in UL-SOAs

As emphasised in Sec. 1.3.1, high-speed AOWC with signal regeneration is of interest in future optical packet switched networks. A typical scenario in such a network could be that a data signal is transmitted over several spans of a long-haul transmission fibre link. During the transmission, the signal quality decreases and should be regenerated at the network access node before the signal is transmitted to the next node. When arriving at a metro-network access node, all WDM channels will be optically amplified with an EDFA before the WDM channel of interest will be converted to the new wavelength of the channel being available in the metro-network or on the next long-haul fibre link.

A combination of a typical SOA single path wavelength converter with the signal regeneration concept of UL-SOAs [46] leads to the conceptual setup in Fig. 4.1. The investigated device is a 4 mm-long bulk

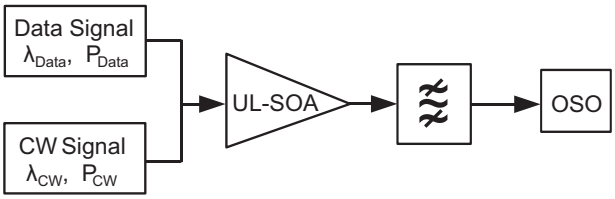


Figure 4.1.: Conceptual setup of the wavelength converter including the ER improvement; optical sampling oscilloscope (OSO)

UL-SOA with the parameters from Tab. B.2. According to the result in Sec. 3.4, the geometric structure of the device has been optimised in order to increase the efficiency of the nonlinear effects ($\Gamma = 0.5$ and $L_{\mathrm{coup}} = 3$ dB). As mentioned in the paragraph above, an appropriate position for the wavelength converter could be after an EDFA. For this reason, the parameters in Tab. 4.1 are assumed for the input data signal. The data signals being investigated are 100 Gbit/s on-off keying (OOK) return to zero (RZ)-50% modulated

| Symbol | Value | Description |
|---|---|---|
| $\lambda_{\mathrm{Data}}$ | 1560 nm | Wavelength of the data signal |
| $\bar{P}_{\mathrm{Data}}$ | 1 dBm | Average power of the data signal |
| $\mathrm{ER}_{\mathrm{Data}}$ | 6 dB | Extinction ratio of the data signal |
| $\lambda_{\mathrm{CW}}$ | 1564 nm | Wavelength of the CW signal |
| $P_{\mathrm{CW}}$ | 2 dBm | Power of the CW signal |

Table 4.1.: Default parameters of the input signals

PRBSs of orders up to 25. The bandpass filter after the UL-SOA is a second-order Gaussian filter with a 3 dB-bandwidth of 275 GHz.

Limited computation capacity made it impossible to simulate complete PRBSs longer than $2^8$-1. Critical bit sequences were taken instead to estimate the impact of bit pattern effects on the regeneration scheme. As mentioned in Sec. 3.2, bit pattern effects occur if the data signal remains long at one of the signal states. Therefore, the critical bit sequences contain various combinations of the following bit sequences: constant signal states, one inverted bit within a constant signal state and alternating bit sequences. These combinations of bit sequences are expected to create worst-case bit pattern effects. A detailed description of the critical bit sequence is given in Sec. G of the appendix.

## 4.1. Investigation of Bit Pattern Effects

In general the speed of bulk and MQW-SOAs for all-optical signal processing is limited to approximately 20 Gbaud due to the carrier lifetime [20, 21]. In contrast, bulk and MQW UL-SOAs should be usable for signal processing of data signals with symbol rates fairly above the carrier lifetime (Sec. 3.2). For SOAs under usual driving conditions, bit pattern effects are expected for a 100 Gbaud data signal. Therefore, 100 Gbit/s OOK RZ-50% data signals (Tab. 4.1) seem to be appropriate to investigate the high-speed feasibility of UL-SOAs.

Fig. 4.2 shows the eye diagram of a 100 Gbit/s data signal before and after the UL-SOA that has been exclusively injected into the UL-SOA. As expected, the eye diagram at the output of the UL-SOA is

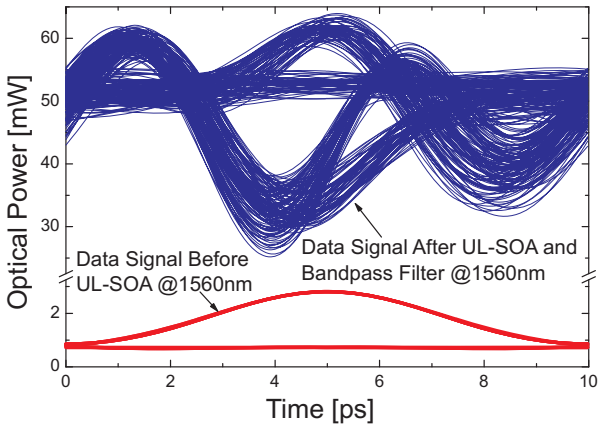


Figure 4.2.: Eye diagram for a PRBS with the length of $2^8$-1 after the bandpass filter at $\lambda_{Data}$ without additional CW signal at the input; the signal is totally distorted due to bit pattern effects, SGM, SPM and ASE

totally distorted due to multiple effects: bit pattern effects, SGM, SPM and ASE. Since 100 Gbit/s are not clearly above the carrier lifetime, it is not clear how significant the contribution to the distortions due to bit pattern effects are. For this reason, the standard deviation of the signal levels at the maximum eye opening (measured at the centre time of 5 ps) as a function of the equivalent PRBS order is evaluated (Fig 4.3). For the PRBS orders up to 6, the standard deviation of the signal states increases resulting in a

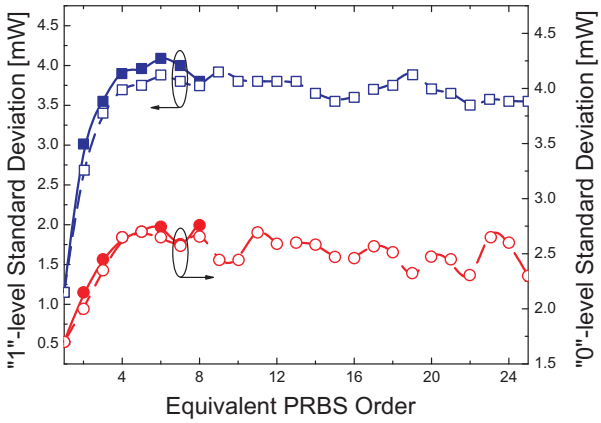


Figure 4.3.: Standard deviation of the signal levels measured at 5 ps in Fig. 4.2 as a function of an equivalent PRBS order after the bandpass filter without additional CW signal; solid lines: true PRBS and dashed lines: critical sequence

decreasing signal quality. The tremendous increase of the standard deviation's "1"-level between the first and fourth equivalent PRBS order can be ascribed to the growing overshoot on top of the eye opening. Moreover, the simulation shows that after a PRBS order of 4 the distortions due to bit pattern effects saturate.

When injecting the data signal with an orthogonally polarised additional CW signal into the UL-SOA, a clearly opened eye diagram can be observed at the output of the UL-SOA (Fig. 4.4). Also, the data

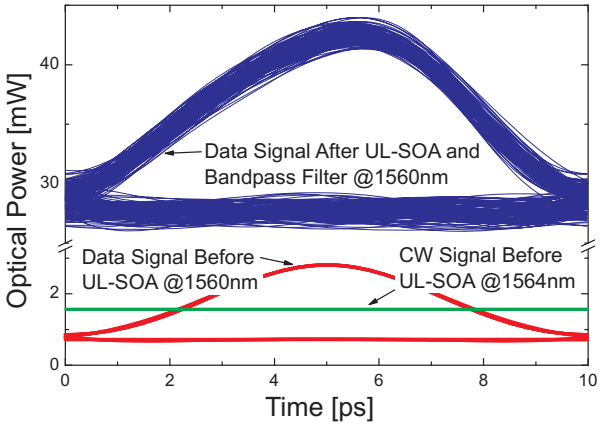


Figure 4.4.: Eye diagram for a PRBS with the length of $2^8$-1 after the bandpass filter at $\lambda_{Data}$ with additional orthogonally polarised CW at the input; compared to the input signal, the output signal has been amplified but the ER has been decreased to 1.9 dB

signal has been amplified by 12 dB. The amplification is about half as much as the amplification for the case with the exclusive transmission of the data signal through the UL-SOA because the gain distributes equally to the data signal and the CW signal. Furthermore, the ER [1] of the data signal has been reduced from 6 dB to 1.9 dB. The investigation of the signal levels' standard deviation shows that for the case with the orthogonally polarised additional CW, nearly no bit pattern effects can be observed (Fig. 4.5). Only a very slight increase between a PRBS order of 1 and 2 can be observed so that the influence of bit

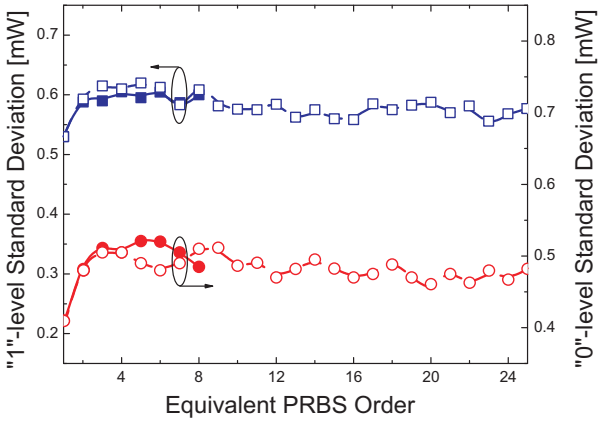


Figure 4.5.: Standard deviation of the optical signal levels measured at 5 ps in Fig. 4.4 as a function of an equivalent PRBS order after the bandpass filter with co-polarised additional CW signal; solid lines: true PRBS and dashed lines: critical sequence

pattern effects is negligible. For this reason, the additional CW signal can be regarded as a holding beam successfully suppressing the bit pattern effects.

To prove the efficiency of the CW signal as a holding beam, the carrier density distribution inside the UL-SOA along the propagation direction has to be regarded. Fig. 4.6 shows the steady-state carrier density for infinitely long constant signal levels. For the case with an additional CW signal, the carrier density peak shifts by 1.5 % of the device length when a worst-case transition after a very long constant signal state appears. For the case without additional CW signal, the carrier density peak shifts by 9.5 % of the device length resulting in a mentionable change of the operation point. Moreover, the small shifts

[1] The ER is defined as the power ratio of the "1"-level to the "0"-level of a data signal. In this thesis the ER is measured at the time of 5 ps of an eye diagram for the minimum "1"-level and the maximum "0"-level of the signal.

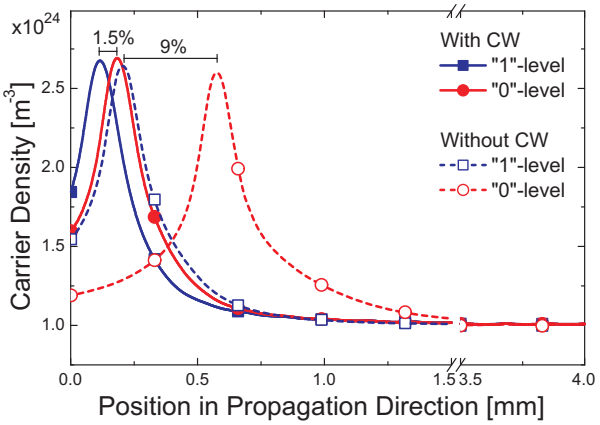


Figure 4.6.: Carrier density distribution along the propagation direction for infinite long constant signal levels of the data signal

of the carrier density peak also have to be related to the UL-SOA's driving conditions and the optimised device. First of all, the low coupling losses and the high optical input power deeply saturate the UL-SOA even for a data signal's "0"-level. Moreover, the small input extinction ratio only results in a small shift of the carrier density peak for a worst case transition. Another aspect is the optimised geometry of the device, increasing the efficiency of the nonlinear intraband effects. Hence, the UL-SOA can be shortened compared to the 8 mm-long device in Sec. B.3. As a result, there is less back-propagating ASE, shifting the carrier density peak towards the front of the UL-SOA contributing to a stable operation point.

In the eye diagram of Fig. 4.4 a broadening of the data signal's traces at the UL-SOA's output can still be seen although the bit pattern effects are negligible. The trace broadening can also be observed for sine modulated signals where no bit pattern effects are expected at all because half the sine's time period is much shorter than the carrier life time. When investigating the distribution of the field intensity's relative standard deviation of the "0"-level and the "1"-level, for both signal levels a Gaussian distribution with an equal relative standard deviation can be observed. As a result, the trace broadening can be ascribed to ASE.

## 4.2. Extinction Ratio Improvement in UL-SOAs

With two input signals, a parametric amplification of the data signal in dependence of the CW signal can be obtained inside the UL-SOA, resulting in a nonlinear transfer characteristic $P_{\mathrm{Out}}(\lambda_{\mathrm{Data}})$ over $P_{\mathrm{In}}(\lambda_{\mathrm{Data}}, \lambda_{\mathrm{CW}})$. With the help of the nonlinear gain characteristic, the ER of the data signal can be improved [46].

### 4.2.1. Operation Conditions for the Extinction Ratio Improvement

Since the ER improvement is caused by a parametric amplification, the input power ratio of the CW signal and the data signal has a major influence on the ER improvement. When plotting the data signal's ER at the UL-SOA's output over the input power ratio, an ER improvement characteristic can be obtained. For a particular input power ratio the data signal's ER after the UL-SOA has increased being of interest for signal regeneration applications with UL-SOAs. In this subsection a systematic study of the UL-SOA's operating conditions for the ER improvement is done. The investigated parameters are: polarisation dependence, relative wavelength alignment, wavelength detuning of the input signals, data signal's input power and ER and the UL-SOA's $\alpha$-factor. The investigations are done with the setup presented in Fig. 4.1. The UL-SOA is the 4 mm-long optimised device and the input signals are the default signals from Tab. 4.1. The centre wavelength of the bandpass filter has been set to the wavelength of the data signal.

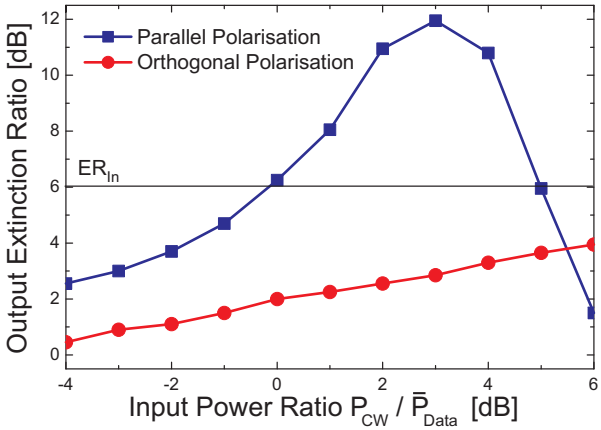


Figure 4.7.: Output ER in dependence of the input signals' polarisation; the signals need to be co-polarised in order to to achieve an ER improvement

The first test series investigates the ER improvement depending on the input signals' polarisation (Fig. 4.7). The input signals need to be co-polarised in order to obtain an ER improvement. The polarisation dependence indicates that dynamic nonlinear effects from Sec. 3.3.2 cause the ER improvement. If the signals are orthogonally polarised, there are no dynamic gain and index gratings, resulting in a decreased ER due to SGM (Sec. 4.1).

The following two investigations should figure out if the Bogatov-like effect is the reason for the ER improvement. Since the Bogatov-like effect depends on the wavelength detuning, the input signals' relative wavelength alignment on the ER improvement is analysed in Fig. 4.8. Having the CW signal located

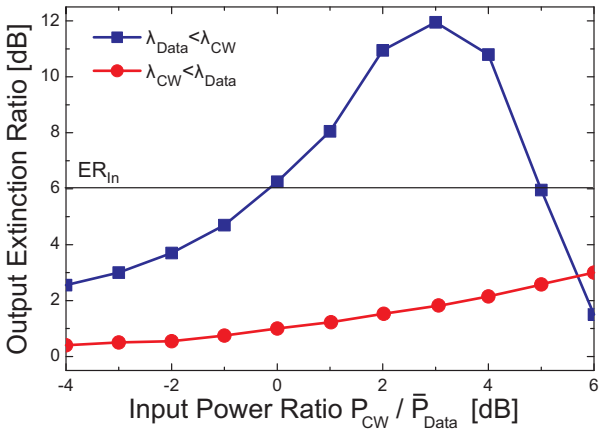


Figure 4.8.: Output ER in dependence of the relative wavelength alignment of the data signal to the CW signal; the data signal has to be located on the shorter wavelength side in order to achieve an ER improvement

on the shorter wavelength side, the data signal's ER after the UL-SOA decreased more than it is conventionally expected (compare to the ER in Fig. 4.7 for orthogonal polarised input signals). The CW signal has to be located on the longer wavelength side in order to obtain an ER improvement. This asymmetry regarding the wavelength detuning is a consequence of the asymmetric probe amplification due to the Bogatov-like effect as presented in Sec. 3.3.2. Similar to the ER improvement the probe is amplified for an alignment on the pump's longer wavelength side while for the shorter wavelength side it is attenuated.

If the Bogatov-like effect truly causes the ER improvement, the $\alpha$-factors of the UL-SOA should have a major influence on the ER improvement. Inverting the $\alpha$-factors results in an inverse behaviour of the ER development (Fig 4.9). For this reason, the alignment of the data signal to the CW signal also has to be changed if the $\alpha$-factors are inverted in order to obtain an increasing ER. In the same manner the Bogatov-like asymmetry flips over with a negative $\alpha$-factor intensifying the indications that the Bogatov-like effect

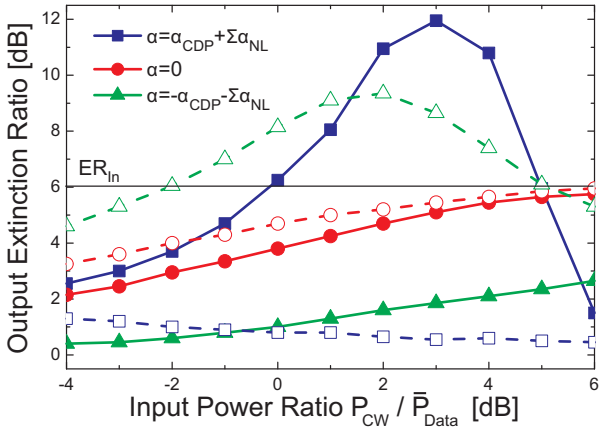


Figure 4.9.: Output ER in dependence of the UL-SOA's $\alpha$-factor; the data signal has to be located on the shorter wavelength side in order to achieve an ER improvement; inverting the $\alpha$-factor leads to an inverse behaviour of the ER improvement (solid lines - $\lambda_{\mathrm{Data}} < \lambda_{\mathrm{CW}}$, dashed lines - $\lambda_{\mathrm{Data}} > \lambda_{\mathrm{CW}}$)

causes the ER improvement.

So far the studied driving conditions enable and disable the ER improvement. Furthermore, they indicate that the Bogatov-like effect causes the ER improvement. The other driving conditions that are investigated in the following part of this subsection should only affect the efficiency of the ER improvement because the efficiency of the Bogatov-like effect is only affected by these driving conditions.

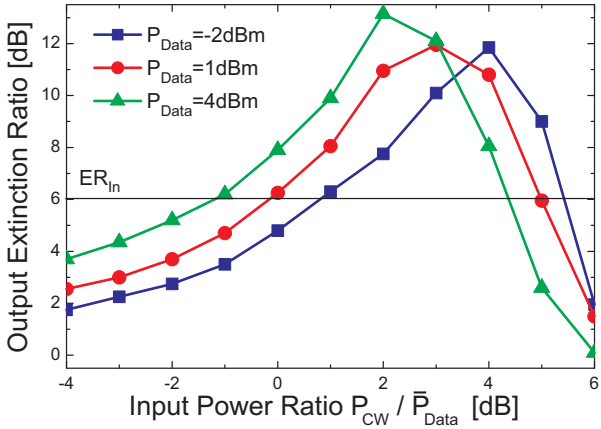


Figure 4.10.: Output ER in dependence of the data signal's input power

Fig. 4.10 demonstrates the dependence of the ER improvement on the input power of the data signal. As long as the input power of the CW signal is readjusted (same input power ratio) only a small influence of the data signal's input power on the ER improvement efficiency can be observed.

The impact of the data signal's input ER on the ER improvement is investigated in Fig. 4.11. Up to an input ER of approximately 7.5 dB of the data signal's ER, the ER improvement efficiency increases with increasing ER of the data signal at the UL-SOA's input being indicated by a slope of the plot being $> 1$. Above an input ER of 7.5 dB the ER improvement saturates.

Lastly the dependence of the ER improvement on the wavelength detuning of the two input signals is studied. Fig. 4.12 only shows, that with increasing wavelength detuning the ER improvement decreases. In [101] has been demonstrated that the ER improvement also decreases for wavelength detunings less than 4 nm. Due to the bandwidth consumption of the 100 Gbit/s data signal, the wavelength detuning could not be reduced below 4 nm so the ER reduction could not be demonstrated.

A detailed discussion of this subsection's results is given at the end of Sec. 4.2.2 when the reason for the ER improvement has been revealed. Moreover, in [101] a comparison between measurements and

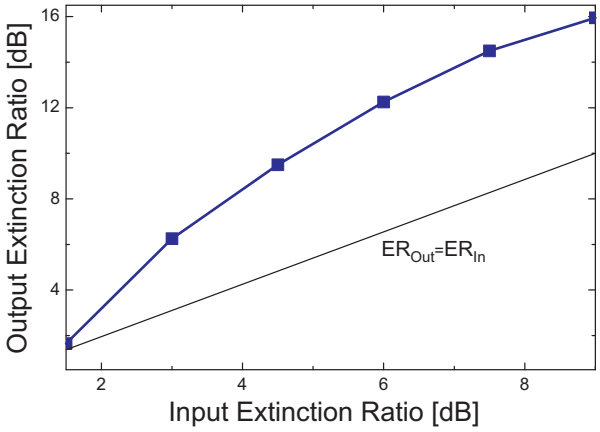


Figure 4.11.: ER after passing the UL-SOA over the data signal's input ER; ER taken from the optimised input power ratio

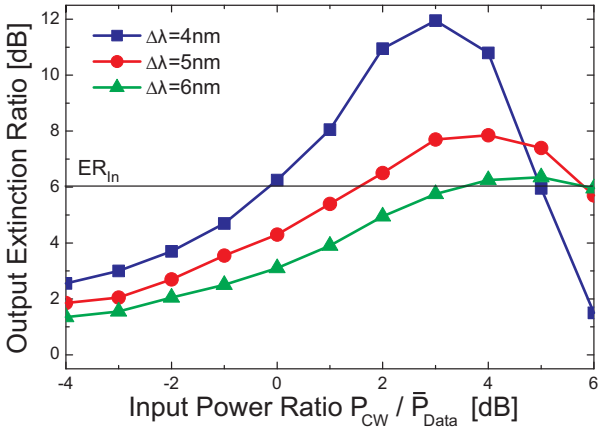


Figure 4.12.: Output ER in dependence of the wavelength detuning; $\lambda_{\mathrm{Data}}$ has been kept constant for this investigation

simulations of this subsection's investigations has been done for the 8 mm-long UL-SOA of Sec. B.3.

### 4.2.2. Reason for the Extinction Ratio Improvement

In the previous subsection, it is shown that the Bogatov-like effect causes the ER improvement in UL-SOAs. In this subsection, the ER development inside the UL-SOA is investigated numerically and with the help of Eqs. 3.14 for the Bogatov-like effect, an explanation is given for the ER improvement. To simplify the explanation, only the data signal's "1"-level ($P_1 = \max(P_{\mathrm{Data}})$) and "0"-level ($P_0 = \min(P_{\mathrm{Data}})$) were investigated because the ER is the power ratio between the data signal's "1"-level and "0"-level ($\mathrm{ER} = P_1/P_0$). As shown in Fig. 4.8, the ER development is dependent on the relative wavelength alignment of the data and the CW signal. Therefore, the case for the ER enhancement will be discussed ($\lambda_{\mathrm{Data}} < \lambda_{\mathrm{CW}}$) first, followed by the same line of arguments applied to the degenerating case ($\lambda_{\mathrm{Data}} > \lambda_{\mathrm{CW}}$).

#### Explanation of the Extinction Ratio Improvement ($\lambda_{\mathrm{Data}} < \lambda_{\mathrm{CW}}$)

The ER improvement will be explained at the example of the 4 mm-long UL-SOA with the optimised input power ratio of 3 dB (Fig. 4.8). Fig. 4.13a) shows the ER development inside the UL-SOA. For the first 1.5 mm of the device the ER decreases. As mentioned in Sec. 3.2, the UL-SOA behaves in this part like a short SOA where the "1"-level is less amplified than the "0"-level because of SGM. However, after 1.5 mm the signals' power are large enough to fully saturate the UL-SOA and the regenerative effect influences the signals.

Following the notation in Sec. 3.3.2, we will now refer to the CW signal as the pump and to the data

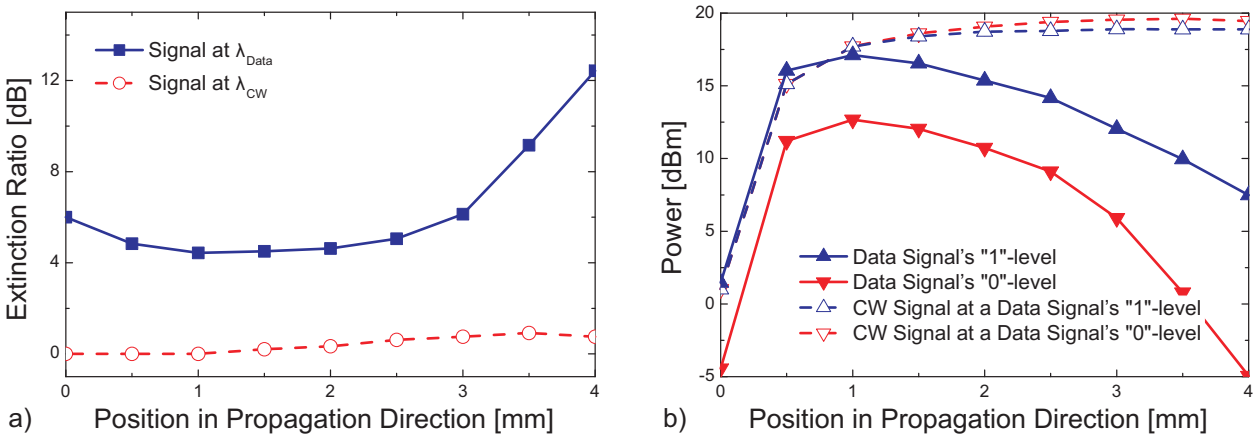


Figure 4.13.: Development of the ER a) and the optical power b) inside the UL-SOA along the amplifier axis for a input power ratio of $P_{CW}/\bar{P}_{Data}$=3 dB and $\lambda_{Data} < \lambda_{CW}$; the major part of the regenerative effect takes place on the last 1.5 mm of the device

signal as the probe. This convention is verified by Fig. 4.13b) showing that the CW signal is always the stronger signal of the two signals.

When regarding Fig. 4.13 it becomes noticeable, that the ER improvement in the saturated section is a two-step process: Firstly, the pump signal is cross-gain modulated by the probe signal (ER≈1 dB). This inverse modulation results in two different pump power levels for the ”0” and the ”1”-state of the probe signal. Secondly, as it was shown in Eqs. 3.14, the gain coefficients related to the Bogatov-like effect are dependent on the pump power. For a probe signal's ”0”-level the power of the pump is maximal, resulting in a stronger attenuation due to the Bogatov-like effect than for a probe signal's ”1”-level. As a result the ER increases. The attenuation of the data signal can mainly be ascribed to the Bogatov-like effect and not to an unbalanced amplification because of the wavelength dependent material gain. The latter is negligible because the wavelength detuning is only 4 nm and the signals are located symmetrically to the gain peak.

The reason why the ER mainly increases on the last 1.5 mm of the device, can also be explained with the dependence of the Bogatov-like effect on the pump signal's power. Fig. 4.13a) shows that the pump signal's modulation depth, affecting the efficiency of the Bogatov-like effect, is maximal on the last 1.5 mm of the device. Another reason for pronounced ER improvement after 2.5 mm is the pump signal's power. Between the position of 1.5 mm and 2.5 mm the pump signal is still amplified by 1.5 dB. This corresponds to a 40% increased gain coefficient in Eqs. 3.14. The effect is even boosted because of the exponential dependence of the probe power on the gain coefficients (solution of the propagation equation Eq. 2.28).

Since the Bogatov-like effect can be easily applied to CW signals, the ER improvement inside the UL-SOA's saturated section has been considered by regarding the ”0”-level and ”1”-level separately. This approach is truly justified because the relaxation times of the fast intraband effects are much shorter than half a bit length. Hence, similar to that of CW signals, a steady-state behaviour of the Bogatov-like effect for modulated signals can be assumed. Furthermore, the effect is usable for high-speed data signals due to the short time constants of the intraband effects.

### Explanation of the Extinction Ratio Degeneration ($\lambda_{Data} > \lambda_{CW}$)

Comparing Fig. 4.7 and Fig. 4.8, for positive frequency detuning ($\lambda_{Data} > \lambda_{CW}$), the ER decreases more drastically in UL-SOAs than conventionally expected. The conventionally decreased ER can be obtained for orthogonally polarised input signals and simply occurs due to SGM. The main additional degeneration takes place on the last 1.5 mm of the device (Fig 4.14a)) and can also be explained with the help of the Bogatov-like effect.

As the wavelength alignment of the signals change, the frequency detuning becomes positive. There-

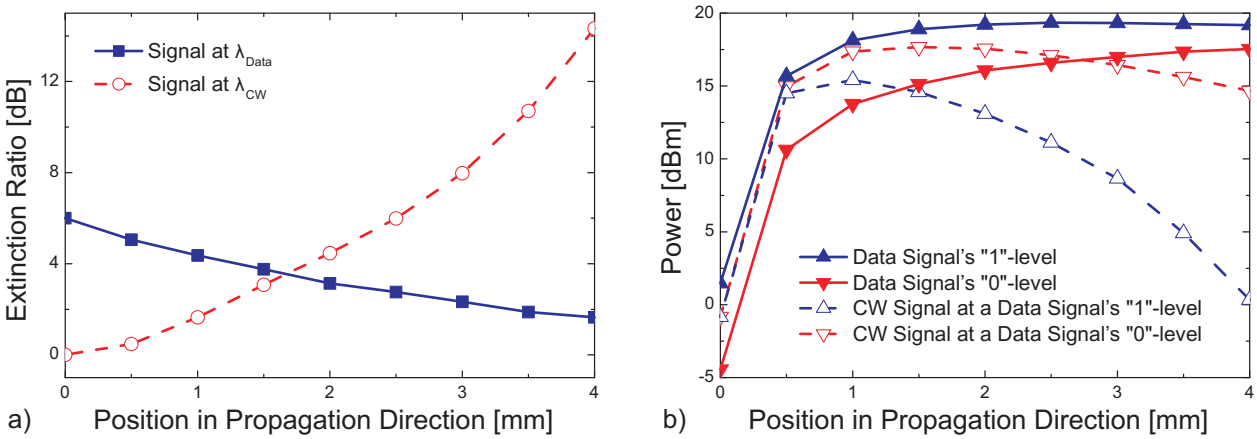


Figure 4.14.: Development of the ER a) and the optical power b) inside the UL-SOA along the amplifier axis for a input power ratio of $P_{CW}/\bar{P}_{Data} = 0$ dB and $\lambda_{Data} > \lambda_{CW}$; in the first part of the UL-SOA's saturated section the amplitude modulation of the CW signal is mainly due to XGM while in the second part the Bogatov-like effect improves the ER of the converted signal at the wavelength of the CW

fore, the Bogatov-like effect results in an additional amplification. Again, the pump signal is inversely modulated to the probe signal (Fig 4.14b)). As a result, a probe signal's "1"-level is less amplified than the "0"-level and the ER decreases. For this frequency detuning, the pump power is smaller than for the negative frequency detuning ($|E_{pump}|^2 < P_{sat}$), resulting in a decreased efficiency of the Bogatov-like effect.

### Detailed Discussion of the Results in Sec. 4.2.1

With the knowledge how the Bogatov-like effect improves the ER in UL-SOAs, in this subsection the results of Sec. 4.2.1 are discussed more in detail.

The ER improvement characteristic showed a strong dependence on the input power ratio (Fig. 4.8, 4.10, 4.11 and 4.12). The dependence on the input power ratio can be explained with the help of Eqs. 3.14 where the efficiency of the Bogatov-like effect increases with increasing power of the pump (CW signal). Therefore, it is advantageous to launch the CW signal with increased power (higher power ratio) into the UL-SOA, to increase the efficiency of the Bogatov-like effect sooner. Hence, the effective length, in which the ER improvement mainly takes place, will be increased for the same device with higher input power ratios. For input power ratios above the optimum ($P_{CW}/\bar{P}_{Data} > 3$ dB in Fig. 4.8) the ER improvement decreases because of two effects. Firstly, for higher input power ratios, proportionally less optical power is modulated in the first part of the saturated section and can therefore cross-gain modulate the CW signal being essential for the ER improvement. Secondly, the more the Bogatov-like effect improves the ER due to asymmetric attenuation, the whole signal is more suppressed causing an increased OSNR because of SE in the saturated section of UL-SOAs and therefore reducing the ER.

While the enabling and disabling functionality of the optical polarisation, the wavelength alignment and the $\alpha$-factor have been already explained in the previous subsections, the ER improvement dependence on the $\alpha$-factor shows another interesting behaviour. In Fig. 4.9 even for $\alpha = 0$ an ER improvement could be observed, which at least compensates the degeneration due to SGM. The previous discussion has shown, that for the ER improvement an unbalanced attenuation of the signal states due to the Bogatov-like effect (parametric amplification) is necessary. As shown in Fig. 4.15, this can also be achieved by the Bogatov-like effect without any $\alpha$-factors although the effect is not as strong as for devices with $\alpha$-factors. For devices like highly nonlinear quantum dash SOAs with a decreased $\alpha$-factor the ER improvement might also be observable, since the fast nonlinear intraband effects are more pronounced than in bulk devices. First investigations of these devices have shown similar Bogatov-like effects [100].

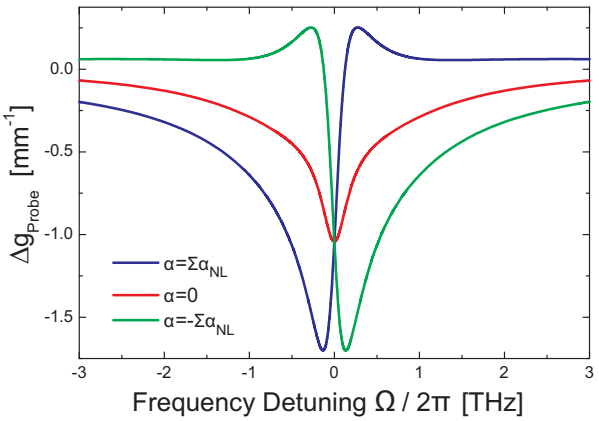


Figure 4.15.: Probe signal's amplification asymmetry in dependence of the $\alpha$-factor; for a device without an $\alpha$-factor the probe signal's amplification is symmetric; for a negative $\alpha$-factor the amplification profile flips over.

The dependence of the ER improvement's efficiency on the input power, the wavelength detuning and the input ER can also be explained more in detail. E.g., for higher input power of the data signal less ASE is generated by the back propagating wave, shifting the carrier density peak to the front of the device. Therefore, the length of the saturated section increases resulting in an increased ER improvement. The shift of the peak towards higher input power ratios in the ER improvement characteristic can also be ascribed to the ratio between ASE and the signals. For the dependence of the ER improvement on the data signal's input ER a saturation can be observed (Fig. 4.11). The saturation is due to SGM of the cross-gain modulated CW signal limiting the ER of the CW signal. At the end the dependence of the ER improvement on the wavelength detuning can also be explained more in detail with the Bogatov-like effect (Fig. 3.7). With increasing wavelength detuning the efficiency of the Bogatov-like effect also decreases because of the fast intraband effects' relaxation time constants.

### 4.2.3. Extinction Ratio Improvement With Wavelength Conversion

In Sec. 4.1, it has been demonstrated that transmission rates faster than the carrier lifetime are also possible due to an additional CW signal. Unfortunately, saturation effects decrease the ER of the data signal significantly (Fig. 4.4). Furthermore, with the help of the additional CW signal the data signal can be wavelength converted due to XGM or FWM. But at the UL-SOA's output the ER of these converted signals is also reduced making them useless for further transmission. If both input signals are co-polarised the ER improvement mechanism from Sec. 4.2.2 can be applied to the wavelength converted signals, improving the ER of these wavelength converted signals.

Since the ER improvement is sensitive to the input power ratio ($P_{\mathrm{CW}}/\bar{P}_{\mathrm{Data}}$), Fig. 4.16 shows the output signal's ER after the UL-SOA and the bandpass filter at different wavelengths (Fig. 4.17) for two different relative wavelength alignments of the input signals. The results illustrate that wavelength conversion with ER improvement due to XGM or FWM as wavelength conversion mechanism is achievable. In order to select the AOWC mechanism that should be used, the wavelength alignment and the CW signal's power have to be set correctly.

#### Wavelength Conversion due to XGM

In Sec. 4.2.1, it has been demonstrated that the data signal has to be located on the shorter wavelength side of the CW signal in order to obtain an ER improvement for the data signal (circle-symbol line of Fig. 4.16b)). For AOWC with ER improvement due to XGM the wavelength of the converted output signal is $\lambda_{\mathrm{CW}}$. For this reason, the wavelength alignment has to be swapped $\lambda_{\mathrm{CW}} < \lambda_{\mathrm{Data}}$ (up-triangle-symbol line of Fig. 4.16a)) which can be explained with the help of Fig. 3.7. Similar to the solo ER improvement case (without AOWC) described in Sec. 4.2.2, the gain-suppressing part of the probe signal's

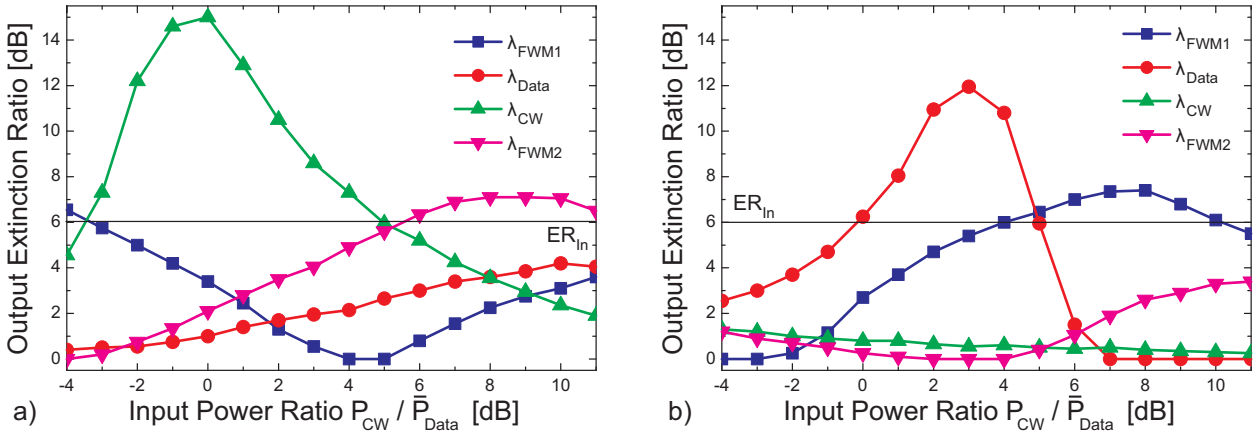


Figure 4.16.: Extinction ratio measured at different wavelength in dependence of the input signals' power ratio; $\lambda_{CW} < \lambda_{Data}$ a) and $\lambda_{Data} < \lambda_{CW}$ b); $\lambda_{FWM1}$ is the first FWM product on the shorter wavelength side of the input signals and $\lambda_{FWM2}$ is the first FWM product on the longer wavelength side of the input signals (wavelengths according to Fig. 4.17)

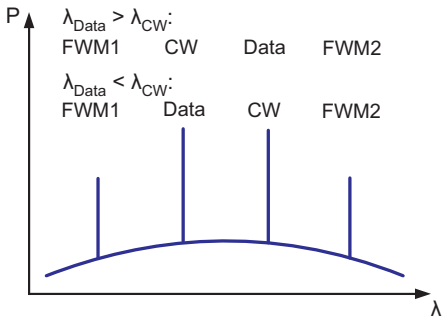


Figure 4.17.: Nomenclature of the spectral components; $\lambda_{FWM1}$ is the first FWM product on the shorter wavelength side of the input signals and $\lambda_{FWM2}$ is the first FWM product on the longer wavelength side of the input signals; the mapping of the input signals is dependent on the wavelength alignment ($\lambda_{Data} > \lambda_{CW}$ or $\lambda_{Data} < \lambda_{CW}$)

amplification asymmetry (negative frequency detuning) is used to achieve the ER improvement. When investigating how the power of the signals develops inside the UL-SOA (Fig. 4.14b)), the data signal is the stronger pump signal and its modulation affects the weaker probe (CW signal). Since the CW signal has been cross-gain modulated in the first part of the UL-SOA's saturated section, its modulation is inverse to the data signal's modulation. Furthermore, the intensity of the Bogatov-like effect is dependent on the pump signal's power (data signal's power). For this reason, the CW's "1"-level is less suppressed than the "0"-level resulting in an increasing ER.

Fig. 4.16 shows that the ER improvement efficiency for the wavelength conversion case is approximately 3 dB better than for the solo ER improvement case. In both cases, the ER improved signal is the probe and for this reason the ER improvement efficiency is dependent on the pump's modulation depth (ER). In the second part of the UL-SOA's saturated section, where the ER improvement mainly takes place, the pump's modulation is stronger for the wavelength conversion case. For the solo ER improvement case, the pump signal's (CW's) modulation is also dependent on the XGM efficiency in the first part of the UL-SOA's saturated section. For the wavelength conversion case the pump (data signal) is already modulated from the beginning and therefore independent of the XGM efficiency.

Fig. 4.18 shows an eye diagram of a 100 Gbit/s RZ-data signal which has been wavelength converted and ER improved. After the bandpass filter where the signal has been filtered from ASE and the original data signal, the converted signal's "1"-level has been amplified by 7.5 dB and the ER has been increased from 6 dB to 13 dB.

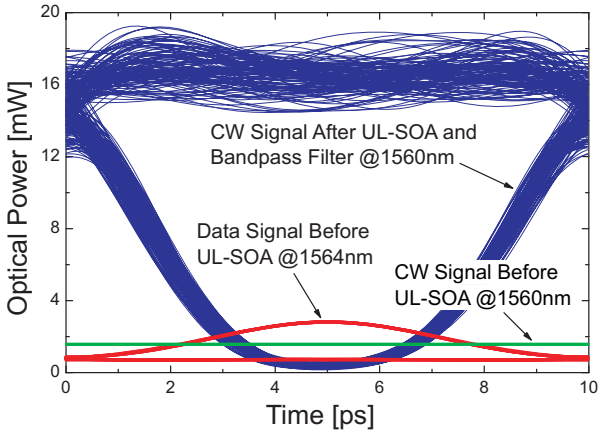


Figure 4.18.: Eye diagram for a PRBS with the length of $2^8$-1 after the bandpass filter; the mechanism for the wavelength conversion is XGM so the data signal is converted to $\lambda_{CW}$ and is inversely modulated; $P_{CW}/\bar{P}_{Data} = 1\,dB$

### Wavelength Conversion due to FWM

AOWC with ER improvement due to XGM from the previous subsection has the ability to convert only to a shorter wavelength. When using FWM as wavelength conversion mechanism instead, up and down conversion with ER improvement can be realised. Moreover, the converted signal is not inversely modulated to the original input data signal.

**Conversion to Longer Wavelengths:** When increasing the input power of the CW signal to 9 dBm and setting the wavelength alignment to $\lambda_{CW} < \lambda_{Data}$, AOWC to longer wavelengths ($\lambda_{FWM2}$) with ER improvement can be achieved. The power of the signal after the UL-SOA and the bandpass filter is approximately equal compared to the data signal's input power and the ER slightly increased from 6 dB to 7 dB. Hence, the ER improvement mainly compensates the ER degeneration due to the saturation effects. The reason for the worse ER improvement compared to the AOWC with ER improvement due to XGM and the solo ER improvement can be figured out when the mechanism of the ER improvement is further investigated. In the saturated section of the UL-SOA the signal is wavelength converted to $\lambda_{Data} + \Delta\lambda$ because of FWM. Since the data signal's ER decreases while propagating through the UL-SOA the ER of the wavelength converted signal is also low. In the second part of the UL-SOA's saturated section, the ER of the wavelength converted signal is improved by the Bogatov-like effect. In contrast to the previously discussed ER improvement mechanisms, the amplifying part of the probe's amplification asymmetry of Fig. 3.7 (positive frequency detuning) is used to achieve the ER improvement (Fig. 4.19a)). During the whole conversion, the converted signal has less power than the original data signal. For this reason, the converted signal will be refereed to as the probe and to the original data signal as the pump. Since the probe and the pump have the same modulation and the efficiency of the Bogatov-like effect is dependent on the pump's power, the probe's "1"-level is more strongly amplified than the "0"-level resulting in an increasing ER. Compared to the negative frequency detuning, the Bogatov-like effect is small for a positive frequency detuning thus decreasing the efficiency of the ER improvement. Although, the CW signal in Fig. 4.19a) has more power than the data signal, its Bogatov-like effect does not cause the ER improvement. First of all, the Bogatov-like effect is negligible over such a large positive frequency detuning and secondly the CW signal is inversely modulated to the converted signal resulting in a decreasing ER of the FWM converted signal in combination with a positive frequency detuning.

**Conversion to Shorter Wavelengths:** Keeping the input power of the CW signal at 9 dBm but changing the wavelength alignment to $\lambda_{Data} < \lambda_{CW}$, AOWC to shorter wavelengths ($\lambda_{FWM1}$) with ER improvement is achieved. The power of the signal after the UL-SOA and the bandpass filter has been decreased by about 1 dB compared to the data signal's input power and the ER also slightly increased from 6 dB to 7 dB. Hence, the ER improvement mainly compensates the ER degeneration due to SGM. Again, the small ER improvement efficiency can be revealed when a closer look is taken on how the Bogatov-like

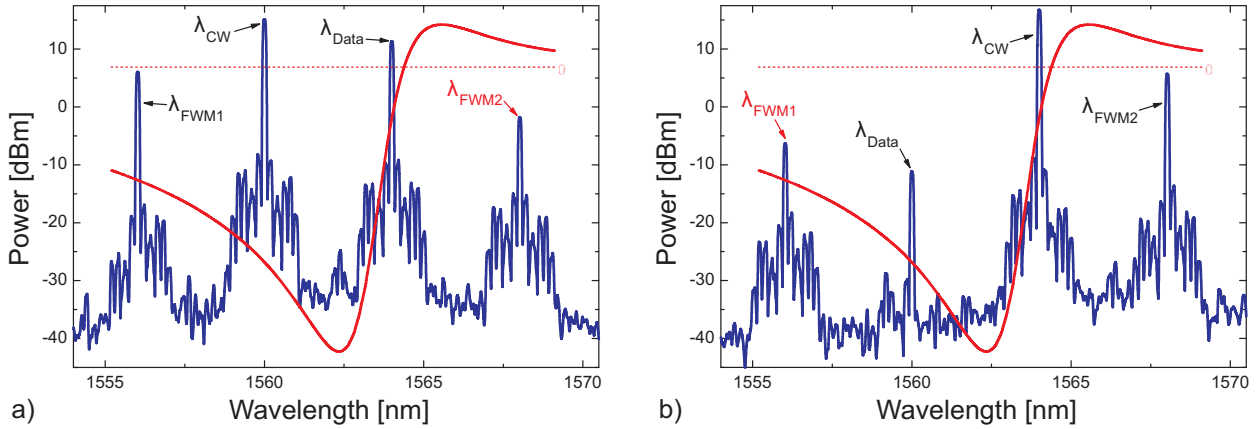


Figure 4.19.: Output spectra of the UL-SOA for a 100 Gbit/s OOK RZ-50% signal which has been wavelength converted due to FWM; conversion to longer wavelengths ($\lambda_{FWM2}$) a) and conversion to shorter wavelengths ($\lambda_{FWM1}$) b); $P_{CW}/\bar{P}_{Data} = 8$ dB; the red graph illustrates the gain of the relevant Bogatov-like effect causing the ER improvement

effect affects the converted signal. Similar to the other FWM case, the signal is wavelength converted to $\lambda_{Data} - \Delta\lambda$ with a decreased ER in the UL-SOA's saturated section while the ER improvement only takes place in the second part of the saturated section. In general, one would expect the converted signal with low power (probe) to be influenced by the stronger data signal but due to the high input power ratio, the data signal is strongly suppressed by the CW signal (Fig. 4.19b)). Therefore, the influence of the data signal on the converted signal due to the Bogatov-like effect is negligible because of the data signal's low power. Instead, the cross-gain modulated and strong CW signal can be regarded as the pump causing the ER improvement. Similar to the solo ER improvement case, the attenuating part of the Bogatov-like effect in combination with the inversely modulated pump increases the ER of the converted signal. So far, the Bogatov-like effect was only discussed for a signals' detuning of $\Delta\lambda$ but in this case the Bogatov-like effect interacts over $2\,\Delta\lambda$ decreasing the efficiency of the ER improvement.

Bit pattern effects are also negligible for the presented AOWC with ER improvement schemes in this section. As emphasised in Sec. 4.1, the inexistence of bit pattern effects is caused by the high optical power of the input signals and the low ER of the data signal. For the XGM case none of these parameters has changed (only the CW signal is parallelly polarised to the data signal) and for the FWM case the optical power of the holding beam (CW signal) had to be increased by 7 dB reducing bit pattern effects even better.

## 4.3. High-Speed Signal Regeneration With UL-SOAs

When considering 2R regeneration, a regenerator has to re-amplify and re-shape the data signal. To achieve this functionality an ideal regenerator has a s-shaped transfer characteristic (Fig. 4.20).

### 4.3.1. Signal Regeneration Due to the Bogatov-like Effect

Compared to the input signal, the output signal in Fig. 4.18 has been amplified (re-amplification) and its ER has been improved (a step towards re-shaping). For this reason, the presented scheme has the potential for 2R regeneration. However, compared to the input signal, the traces of the output signal have been broadened. Hence, the re-shaping condition has not been met completely because of missing noise compression. Comparing the traces of Fig. 4.4 and Fig. 4.18 an additional broadening of the "1"-level in Fig. 4.18 can be observed being not caused by ASE. The additional broadening in Fig. 4.18 can be ascribed to the operating point of the UL-SOA being at a steep slope of the transfer characteristic in

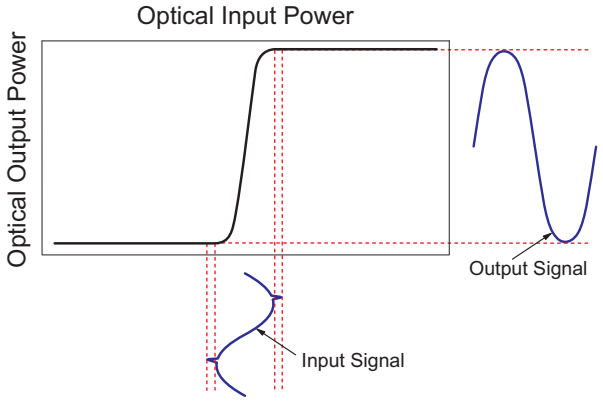


Figure 4.20.: Ideal transfer characteristic ($|E_{out}|^2$ over $|E_{in}|^2$) for a 2R regenerator; fluctuations of the input signal are suppressed due to the clipping functionality of the transfer characteristic

order to obtain a maximum ER improvement. As a result, small fluctuations of the optical power due to ASE, as they are typical for UL-SOAs (Fig. 4.4), will be increased at the output. Fig. 4.21 shows how the

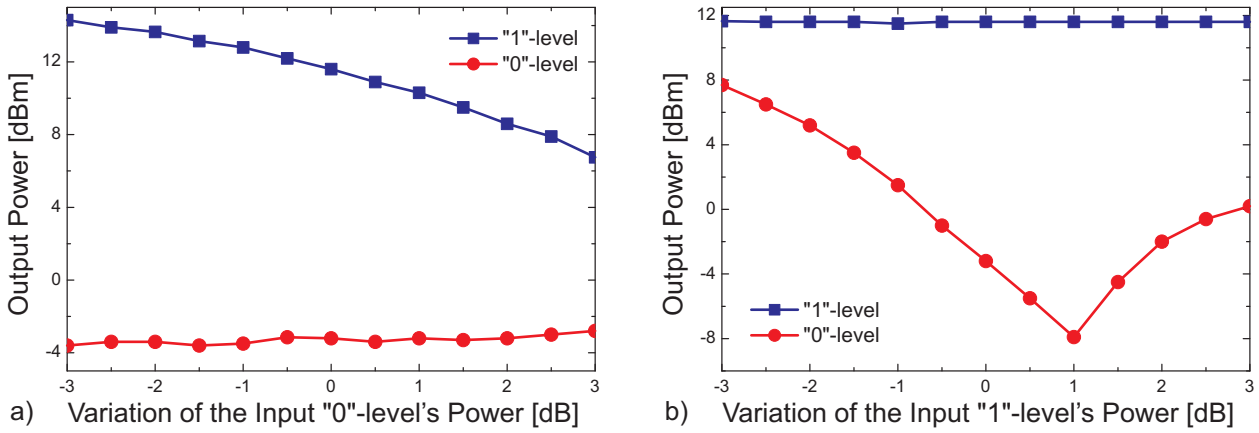


Figure 4.21.: Power of the signal levels after the UL-SOA as a function of a change of the input data signal's levels' power; for the variation of the "1"-level a), the input power of the "0"-level has been set fixed and for the variation of the "0"-level b), the input power of the "1"-level has been set fixed; for no power variation of the input data signal's levels (0 dB), the results from Fig. 4.18 are obtained

power levels of the wavelength converted signal from Fig. 4.18 depend on variations of the power levels of the input data signal. Since the wavelength converted signal is inverse modulated to the data signal, the power of the output signal's "0"-level varies with a change of the input signal's power of the "1"-level and vice versa. Again, the investigation validate that small variations of the input signal are increased at the output of the UL-SOA. Fig. 4.21b) shows a saturation in the power change of the output "0"-level for a variation of a input "1"-level (> 1 dB). The saturation is caused by a deformation of the output eye diagram being a result of XPM due to the increased peak power of the data signal's "1"-level. The results are in good agreement with the simulation of the output ER as a function of the input ER (Fig. 4.11) also indicating that small variations of the input signal are increased at the output of the UL-SOA. A solution for this problem would be clipping of the signal levels, being typically obtained for the "1"-level due to SGM in SOAs. The inexistence of the gain saturation for the presented scheme is also indicated by the signals' output power levels in Fig. 4.18 and Fig. 4.4 being about 6 dB less for the parallel polarised case where the Bogatov-like effect is enabled. Since the attenuating part of the Bogatov-like effect is used for the ER improvement, the output signal's "1"-level for the AOWC cases with conversion to shorter wavelengths and for the solo ER improvement case do not saturate.

For the conversion to longer wavelengths, the amplifying part of the Bogatov-like effect is used to

achieve the ER improvement so in general a saturation should be possible. Unfortunately this ER improvement mechanism is very inefficient (Sec. 4.2.3) so the UL-SOA's length needs to be increased. Moreover, in MQW-devices with a decreased $\alpha$-factor the probe's gain asymmetry becomes more and more symmetric and will also lead to attenuation for a positive frequency detuning (Fig. 4.15). Hence, the ER improvement mechanism for conversion to longer wavelengths might not be observable. In such a case, the wavelength alignment must be $\lambda_{\text{Data}} < \lambda_{\text{CW}}$ in order that the inverse modulated CW also improves the ER of the wavelength converted signal. Furthermore, in MQW-devices the mode confinement is much smaller, decreasing the efficiency of the effects due to the nonlinear gain (Sec. 3.4). Therefore, an ER improvement might not be observable in MQW-devices at all.

### 4.3.2. Using a Pulse Reformatting Filter

Another single path technique for wavelength conversion with the potential for signal regeneration has been presented in [102]. In contrast to other earlier discussed wavelength conversion mechanisms with ER improvement, the nonlinear effect causing the functionality of the wavelength conversion and the regeneration mechanism is XPM. The scheme can also be applied on high-speed data signals but due to bit pattern effects in short SOAs [43], signal regeneration cannot be achieved. Since in Sec. 4.1 it has been demonstrated that bit pattern free high-speed signal processing with UL-SOAs is possible but the signal has been distorted because of SPM, UL-SOA should provide the ability for high-speed wavelength conversion with signal regeneration with this technique being investigated in this subsection.

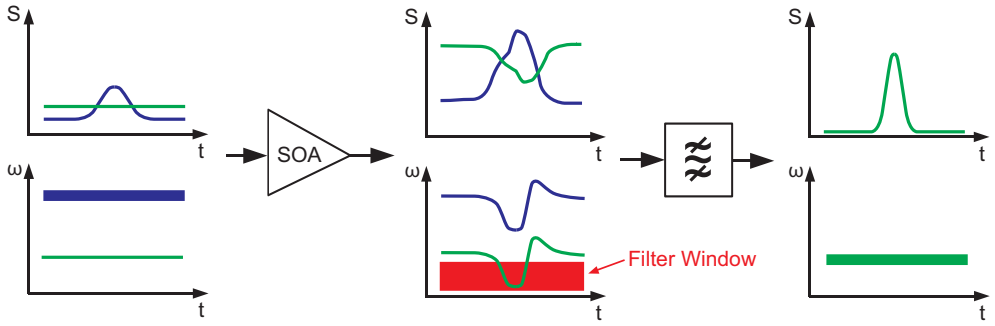


Figure 4.22.: Conceptual mode of operation for wavelength conversion with signal regeneration due to a pulse reformatting filter; the upper three plots show the photon density over the time before and after the UL-SOA and after the bandpass filter respectively and the lower plots the corresponding spectra over the time

Fig. 4.22 shows the conceptual mode of operation for wavelength conversion with signal regeneration with a pulse reformatting filter. A data signal and a CW signal enter an SOA. While propagating through

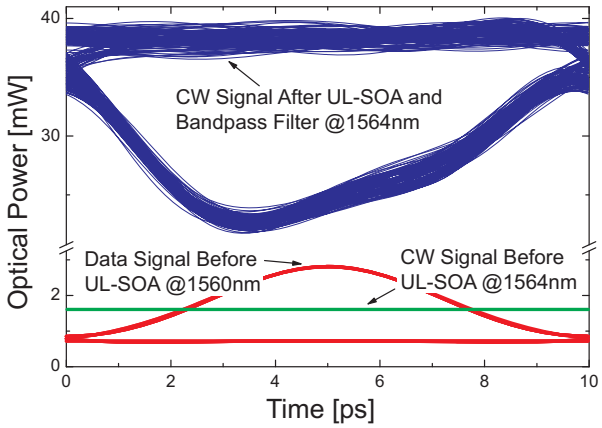


Figure 4.23.: Eye diagram of a wavelength converted data signal after the bandpass filter at $\lambda_{\text{CW}}$; compared to the input signal, the output signal has an asymmetric shape due to XPM

the SOA the data signal's intensity modulation modulates the phase of the CW signal because of the $\alpha$-factors (Eqs. 2.17). The phase modulation can be considered as a frequency shift (chirp) for a certain moment in time. Shifting the centre frequency of the bandpass filter to smaller frequencies than the CW signal's frequency, the filter will only pass light of the CW signal at the moment of the chirp resulting in a wavelength converted output signal with an ER improvement.

Using the same principal setup as for the simulations in Fig.4.4 but regarding the cross-gain modulated signal at the CW signal's wavelength after the bandpass filter (Fig. 4.23), a clearly opened eye diagram with distortions due to XPM can be observed. When readjusting the centre wavelength and the bandwidth of the bandpass filter according to the concept of Fig. 4.22, the eye diagram and spectra in Fig. 4.24 can be obtained. Compared to the input signal, the power of the converted signal remained nearly unchanged

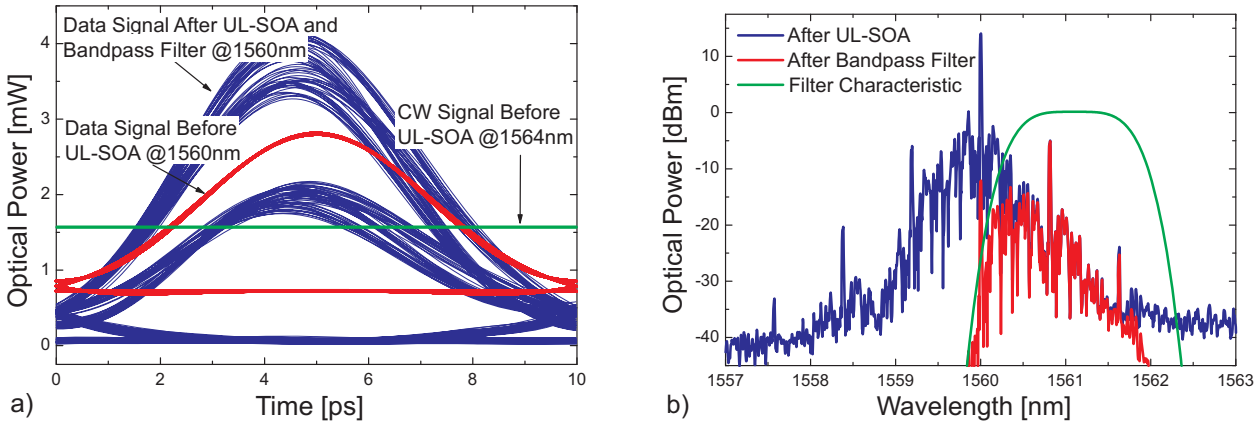


Figure 4.24.: Eye diagram for a PRBS with the length of $2^8$-1 after the bandpass filter a) and spectra of the signal before and after the bandpass filter; the bandpass filter has a 3 dB-bandwidth of 160 GHz and an offset of 1.1 nm to the centre wavelength of the CW signal; the signals are polarised orthogonal in order to avoid the influence of dynamic nonlinear effects

but the ER improved from 6 dB to 13 dB. Moreover, the eye diagram shows a double trace for the "1"-level indicating bit pattern effects.

Although the setup has not been changed, compared to the results in Fig. 4.4, the eye diagram in Fig. 4.24a) shows bit pattern effects. When investigating the phase of the CW signal after the UL-SOA (Fig. 4.25), patterns with the same timing as the power patterns can be observed. Fig. 4.25 shows that the CW signal has been cross-gain modulated and its phase is cross-phase modulated by the data signal. Furthermore, the results show that the optical power is nearly free of bit pattern effects while for the phase slight bit pattern effects can be observed. In spite of the holding beam there is still slight CDP due

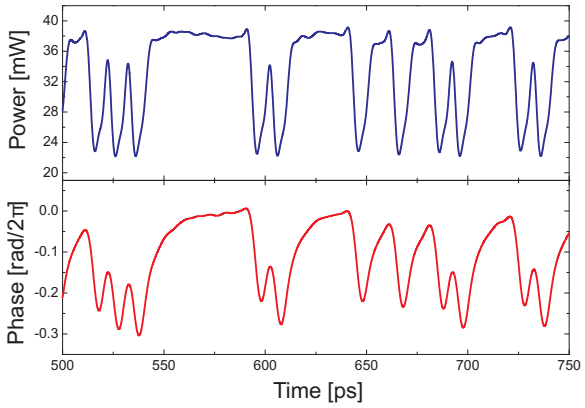


Figure 4.25.: Power and phase after an UL-SOA at the wavelength of the CW signal; the CW signal's power has been cross-gain modulated and its phase cross-phase modulated due to the data signal

to the power variation of the input data signal. For the gain variation this contribution is negligible since the other nonlinear gain suppressions are much stronger. However, due to the $\alpha$-factor the contribution of CDP to the phase change gets boosted because $|\alpha_{\mathrm{CDP}}| > |\alpha_{\mathrm{CH}}|$ and $\alpha_{\mathrm{SHB,FCA}} \approx 0$. Even if $|\Delta\phi_{\mathrm{CDP}}| < |\Delta\phi_{\mathrm{CH}}| + |\Delta\phi_{\mathrm{TPA}}|$ they are still in the same range so $\Delta\phi_{\mathrm{CDP}}$ causes bit pattern effects in the signal's phase. For this reason, the scheme with an optical reformatting filter is not bit pattern free for high-speed data signals in UL-SOAs. On top of that the small phase modulations, due to the fast intraband effects, are too inefficient to provide noise compression and therefore to reduce bit pattern effects.

# 5. Supercontinuum Generation With UL-SOAs

Sec. 1.3.2 emphasised that the tunability of components is important in future optical communication networks. Similarly, in present networks the devices need to be tuneable in order to compensate production tolerances. Typically, MLLs are used as integrated supercontinuum sources but the wavelengths of these devices depends on the devices' geometry depending on the tolerances of the production processes. In contrast with UL-SOAs where the tunability is defined by the gain bandwidth and the tunability of the input signals, e.g., the investigation in Fig. 3.9 showed that broad mode combs can be obtained over a range of 15 nm.

Since the simulation results in this chapter are compared with measurements, the unoptimised 8 mm-long UL-SOA from Sec. B.3 is used again. The default values for the two co-polarised CW input signals are: 8.5 dBm at 1562.92 nm and 8.5 dBm at 1563.08 nm.

## 5.1. Generation of Short Pulses

Applying the Fourier transformation on a signal with a broad spectrum and linear phase relation of the frequency components yields a single short pulse in time-domain. In order to obtain a pulse train in time-domain, the spectrum has to be sampled with equidistant frequency steps [103]. Such a non-continuous spectrum can be generated with FWM when two co-polarised CW signals enter an UL-SOA (Eqs. 3.12). Fig. 5.1 shows the conceptual setup for such a pulse source. Since the CW signals can be tuned, the output

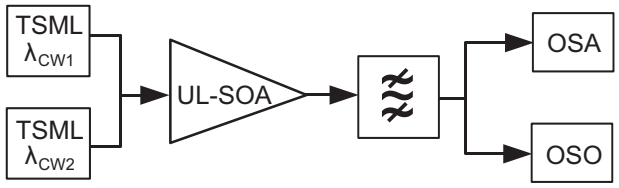


Figure 5.1.: Conceptual setup for investigating the generation of short pulses; tuneable single mode laser (TSML), optical spectrum analyser (OSA), optical sampling oscilloscope (OSO)

pulses can also be tuned. When shifting both signals and keeping the detuning constant, the wavelength of the pulses can be tuned. The detuning of the CW signals adjusts the repetition rate of the pulses.

### 5.1.1. Phase Relation of the FWM Modes

In order to create short pulses, the phase relation between the FWM modes has to be linear. The simulation in Fig. 3.11 shows that the phase relation of the FWM modes is not linear for the regime with high optical power FWM modes while on the shorter wavelength side, a region with approximately 40 modes with linear phase relation can be found. For this reason, it is advantageous to make use of the low power FWM modes from the linear phase regime for generating short pulses even if the output power is reduced. If all FWM modes are to be used for the pulse generation, an additional element with wavelength dependent chromatic dispersion is needed in order to correct the phase. Since the phase signature of the FWM modes cannot be fitted with a second-order polynomial, dispersion compensation fibres cannot be used for the phase correction. An individual phase correction of each FWM mode can be done with distributed Bragg gratings, but this device would limit the tunability of the presented scheme significantly. In order to improve the tunability, novel devices like a double arrayed waveguide grating (AWG) with a thermal lens could resolve the problem [104] but would increase the complexity of the setup drastically.

### 5.1.2. Locking of the Generated Pulses

The mechanism causing the pulse generation in UL-SOA is FWM. For this reason, phase fluctuations of the input signals will affect all generated FWM modes due to the phase relation of the FWM mechanism (Eq. 3.12). When using two separate external cavity lasers (ECLs) similar to what was done for the investigations in Fig. 3.9, the phase of the input CW signals vary randomly due to phase noise or variation of the operation points. As a result, the generated pulses jitter. Moreover, for investigating the generated pulses with an optical sampling oscilloscope (OSO), the OSO needs to be triggered to the repetition rate of the pulses. Due to the phase noise, triggering with the generated pulses would not be stable enough to obtain results from the OSO. A solution to synchronise the OSO and the pulse timing is to generate the optical input signals from a stable electrical signal that can also be used for triggering the OSO. Moreover, the optical signal should only consist of two spectral modes. These demands can be achieved if an electrical signal drives a MZI in the quadrature point generating a carrier-suppressed sine-modulated signal [105].

In contrast with simulations, the triggering is only a problem for measurements since in simulations, the phase relation of the CW lasers can be easily set to be fixed. For this reason, the input signal of all further measurements in this section is created with a MZI driven in the quadrature point while the simulation are done with two CW input signals.

### 5.1.3. Results

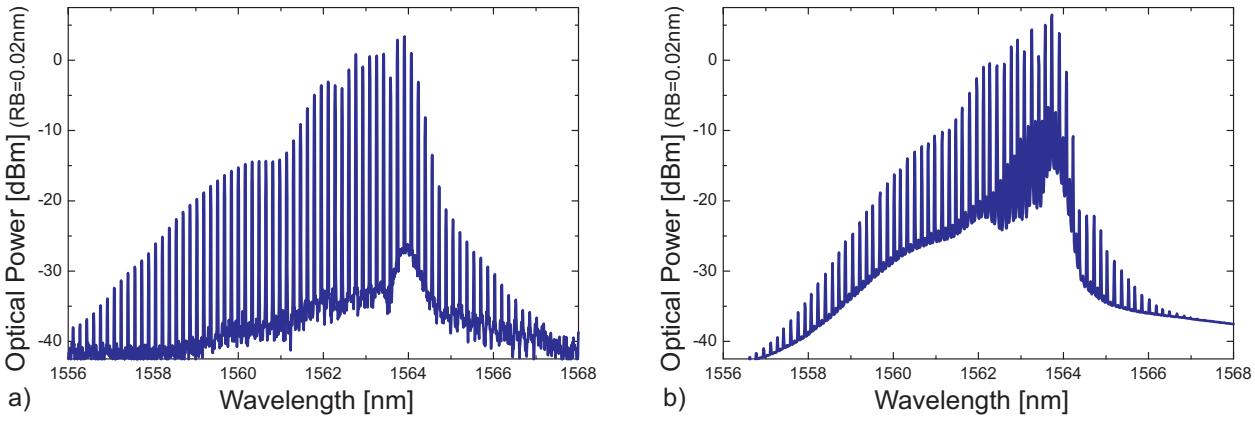


Figure 5.2.: Simulated a) and measured b) output spectrum after the UL-SOA for all FWM modes; the simulation results corresponds to Fig. 3.11; the measurements were done by the group of B. Sartorius from the *HHI*

Based on the result presented in Fig. 3.11 (simulation results of Fig. 5.3 correspond to Fig. 3.11) and regarding the time-domain signal for the whole FWM comb from Fig. 5.2, the simulations and the measurements show a spike followed by an inverted spike, both with a constant power offset. The repetition rate is 20 GHz corresponding to the input mode spacing of 0.16 nm. As predicted in Sec. 5.1.1, no useable pulses can be obtained due to the phase distortion of some FWM modes. In frequency-domain the differences between simulation and measurements can be ascribed to the slightly different input signals as mentioned in Sec. 5.1.2. For the measurements the carrier signal of the carrier-suppressed sine-modulated signal is not totally suppressed and therefore it is also contributing to the FWM processes. As a result, an increased noise floor can be observed in the spectra. Moreover, the measured output signal is amplified with an EDFA and transmitted with a fibre to the OSO creating additional phase distortion due to chromatic dispersion while the simulation shows the output signal directly after the UL-SOA resulting in additional differences in time-domain.

When filtering the FWM modes of the linear phase regime (4 nm from the comb's shorter wavelength side Fig. 3.11), mainly FWM modes with a linear phase signature are used for the pulse generation

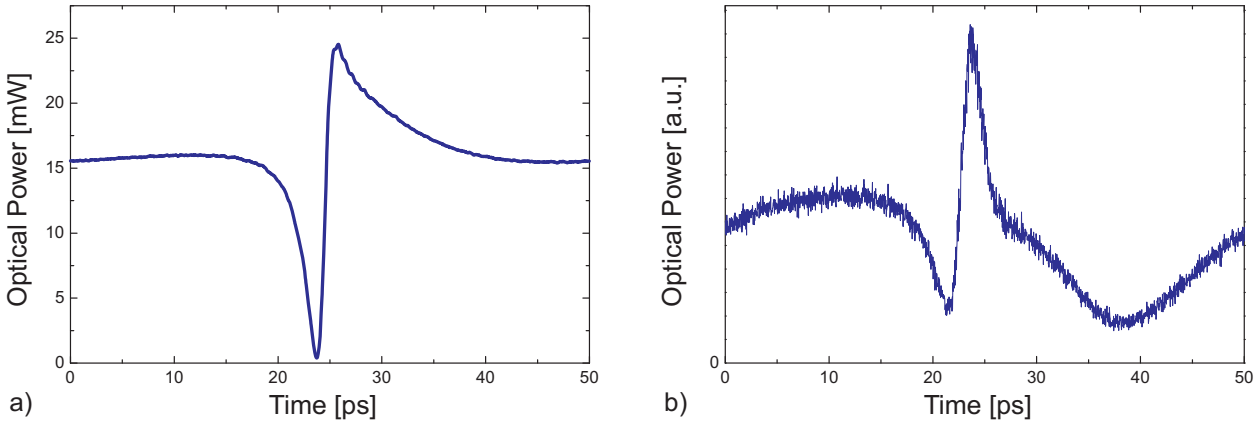


Figure 5.3.: Simulated a) and measured b) output signal after the UL-SOA for all FWM modes; the measurements were done by the group of B. Sartorius from the *HHI*

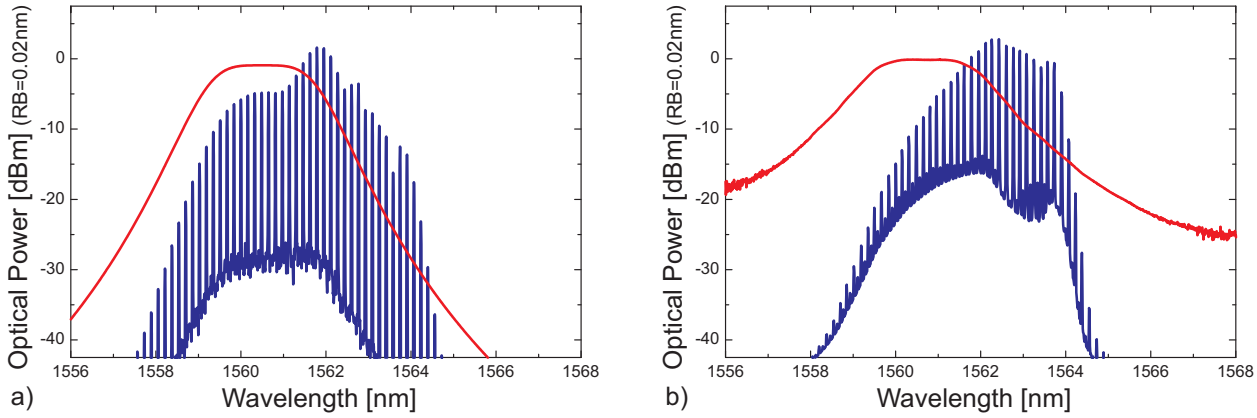


Figure 5.4.: Simulated a) and measured b) output spectrum after the UL-SOA and the bandpass filter when only taking FWM modes with linear phase relation; the red line shows the frequency characteristic of the bandpass filter; the measurements were done by the group of B. Sartorius from the *HHI*

(Fig. 5.4). As a result, the time-domain signal has a clear and slightly nonsymmetric pulse shape and pulses with full width half maximum (FWHM) of approximately 5 ps and a repetition rate of 20 GHz could be obtained from simulations and measurements (Fig. 5.5).

To further shorten the generated pulses, the influence of the FWM modes from the linear phase regime has to be improved. For the results in Fig. 5.2 and Fig. 5.4 the high power FWM modes with a nonlinear phase signature dominated or had a non-negligible contribution to the pulse generation. For the next approach the centre wavelength of the filter is located at the very short wavelength side of the FWM mode comb, so the filter's slope is used to equalise the amplitudes of the FWM modes. Regarding the spectra in Fig. 5.6, the FWM modes from the linear phase regime became more dominant due to this filtering technique. Hence, the main part of the optical power is now located in the linear phase regime. Regarding the output signal in the time-domain (Fig. 5.7), pulses with only slight distortions and a FWHM of less than 2 ps can be observed.

### 5.1.4. Tunability of the Pulses Source

As mentioned at the beginning of Sec. 5.1, the presented scheme should also provide a tunability of the pulses' repetition rate depending on the mode spacing of the input CW signals. Furthermore, the bandwidth of the generated FWM mode comb strongly depends on the mode spacing of the input CW

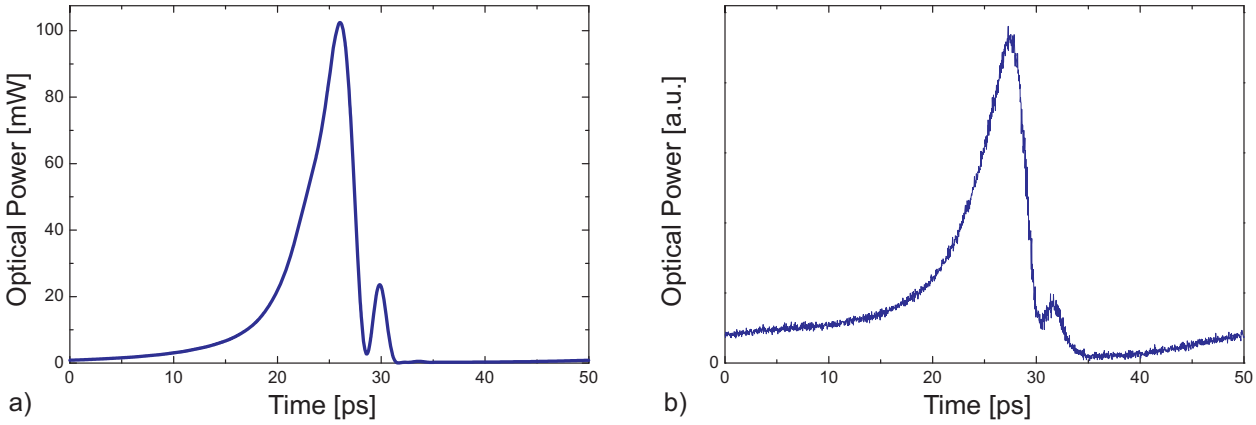


Figure 5.5.: Simulated a) and measured b) output signal after the UL-SOA and the bandpass filter when only taking FWM modes with linear phase; the measurements were done by the group of B. Sartorius from the *HHI*

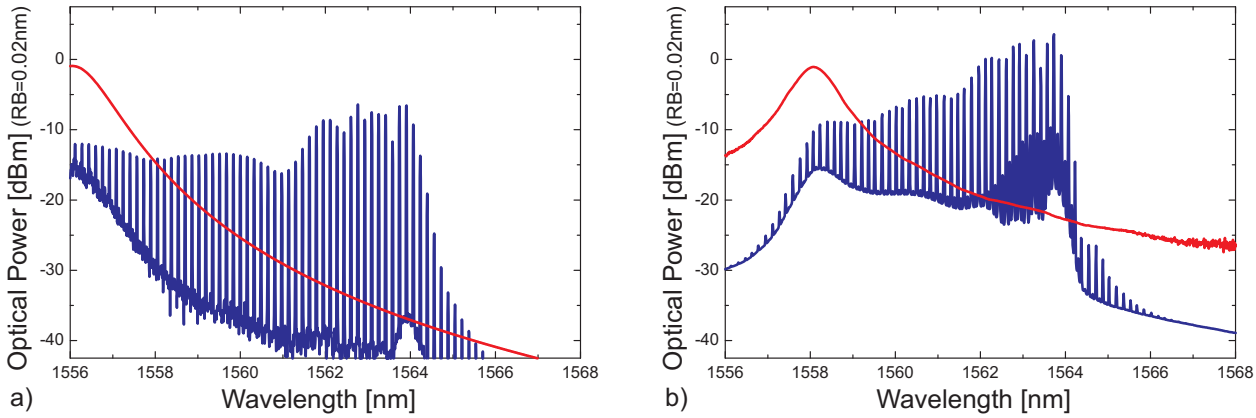


Figure 5.6.: Simulated a) and measured b) output spectrum after the UL-SOA and the bandpass filter when equalising the FWM modes with the help of the filter's slope; the red line shows the frequency characteristic of the bandpass filter; the measurements were done by the group of B. Sartorius from the *HHI*

signals. For this reason, the pulsewidth of the generated pulses also depends on the mode spacing of the input CW signals (Fig. 5.8). The simulations show that for all filtering techniques, the pulsewidth decreases with increasing mode spacing. Hence, with increasing repetition rate of the pulses, shorter pulses can be obtained. Moreover, assuming that an ideal phase correction, as discussed in Sec. 5.1.1, limits the bound for generating short pulses with this UL-SOA device, the investigation shows that the equalising filtering technique yields nearly optimal results. Therefore, the pulse generation should be done without an additional phase correcting device since such a device only limits the tunability and creates unnecessary complexity for the pulse source.

Another interesting point from the investigation in Fig. 5.8 is that the generated pulsewidth is limited to about 400 fs. For the equalising filtering technique and the case with ideal phase correction, the pulsewidth saturates for a mode spacings greater than 400 GHz due to the gain bandwidth of the UL-SOA's saturated section (400 fs corresponding to approximately 20 nm). Considering the tunability of the pulses' carrier wavelength, Fig. 3.9 showed that the FWM mode comb can be generated over a range of 15 nm by two input CW signals that have also been varied over the same range. Hence, the generated pulses can be tuned over the same range. However, with increasing mode spacing the tunability of the carrier wavelength reduces because of the UL-SOA's gain bandwidth. E.g., pulses with a mode spacing greater than 400 GHz cannot be tuned in the centre wavelength.

Furthermore, the figure shows that around 200 GHz of mode spacing, the pulsewidth for the case with

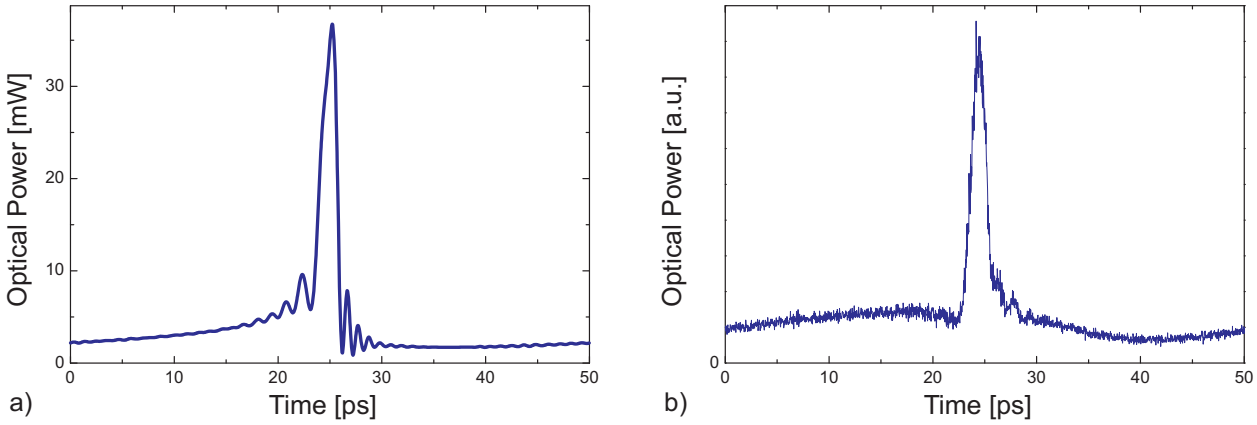


Figure 5.7.: Simulated a) and measured b) output signal after the UL-SOA and the bandpass filter when equalising the FWM modes with the help of the filter's slope; the measurements were done by the group of B. Sartorius from the *HHI*

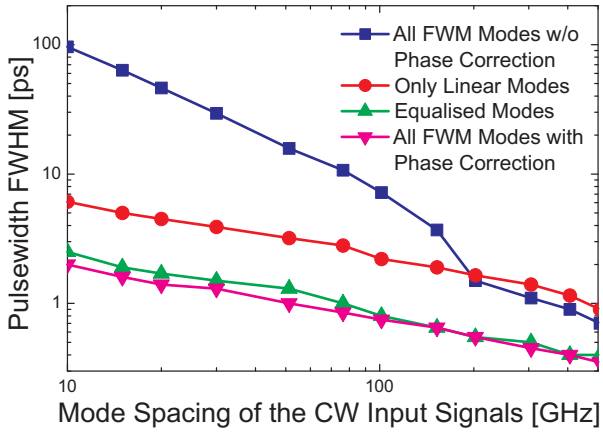


Figure 5.8.: Simulated pulsewidth of the generated pulses for different filtering techniques as a function of the input CW signals' mode spacing

all FWM modes becomes shorter than for the case where only modes of the linear phase regime are used for the pulse generation. The reason for this effect can be ascribed to the Bogatov-like effects decaying with increasing mode spacing. As a result, the phase distortion cannot be carried over multiple modes. Therefore, the distortion only affects one mode for larger modes spacings. In addition, the power of the mode with the distorted phase is reduced by the Bogatov-like effect reducing its contribution to the pulse generation. Hence, the few modes with linear phase on the longer wavelength side also efficiently contribute to the pulse generation making no-filtering technique more efficient than filtering only the modes with linear phase relation.

In order to comment on the efficiency of the generated pulses with the presented scheme here, the time-bandwidth product can be defined as the product of the pulsewidth and the spectral width (both measured at FWHM). Fig. 5.9 illustrates that the spectral efficiency of the generated pulses with ideal phase recovery is optimal since the value of the time-bandwidth product corresponds to the value of $\mathrm{sech}^2$-pulses. For small mode spacings the value of the time-bandwidth product for the case where the filter slope is used to equalise the FWM modes is close to the value of sinc-pulses underlining the equalisation process because sinc functions in time-domain corresponds to rectangular functions in frequency-domain [103].

Again, it has to be mentioned that chromatic dispersion is not considered in the simulations. In Sec. 2.3.5, it has been estimated that up to approximately 250 GHz of mode spacing, the influence of the input CW signals' phase walk-off for an 8 mm-long UL-SOA is negligible. For this reason, chromatic dispersion should not significantly influence the results in Fig. 5.8 and Fig. 5.9 for high mode spacings.

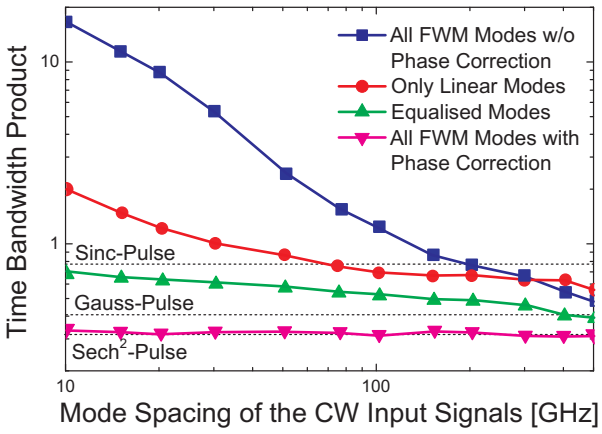


Figure 5.9.: Simulated time-bandwidth product of the generated pulses for different filtering techniques as a function of the input CW signals' mode spacing

### 5.1.5. Possible Further Improvements

To further improve the efficiency of creating short pulses with this UL-SOA device, modulated input signals could be used as a FWM seed, already having a linear mode comb in frequency-domain. In contrast with HNLFs where usually modulated input signals are used and the SPM, due to the Kerr effect, causes the pulsewidth reduction, in UL-SOAs the pulse shortening is due to dynamic gain and index gratings creating FWM products. The most efficient FWM mode creation can be obtained from modes with equal power [1] but for amplitude modulated signals, the carrier mode always dominates reducing the efficiency of creating FWM modes. Furthermore, when using short pulses as FWM seed having a very broad mode comb in frequency-domain and the time between the two pulses is in the range of the carrier lifetime, the UL-SOA is not driven in a stable operation point and slow interband effects distort the pulse generation. The usage of phase modulated input signals does not improve the performance either. Although phase modulated signals have a broad spectral mode comb, they cannot create the dynamic gratings for the FWM processes because the nonlinear effects, producing the dynamic gratings, are dependent on the photon density (Eq. 2.14) and for phase modulated signals, the photon densities are constant.

Another possibility for improving the generation of short pulses could be device optimisation. In Sec. 3.4 it has been presented, that the mode confinement plays an important role for the creation of FWM mode combs. For this reason, bulk devices should have clear advantages over MQW devices. On the other hand, MQW devices have a slightly smaller $\alpha$-factor resulting in slightly less phase distortion due to the Bogatov-like effect. Nevertheless, the phase distortion only has a minor effect on the pulse generation due to the equalising filtering technique. Hence, bulk devices with a high mode confinement should be the number one choice for pulse generation.

## 5.2. CoWDM Carrier Source

In this section the feasibility of UL-SOAs is investigated for generating a coherent carrier comb useable as carrier source for CoWDM and CO-OFDM networks.

For the pulse generation in Sec. 5.1 the phase relation of the generated FWM mode comb has to be linear while for a CoWDM carrier source the FWM modes' phase relation only have to be fixed (coherent). Since the generation of the supercontinuum is caused by cascaded FWM, the phase relation of the generated mode comb is fixed as long as the input signals are coherent. When using two separate

[1] In Sec. 3.3.2 has been mentioned that FWM is caused by the dynamic part of the total photon density (Eq. 3.10). Since the total photon density in the saturated section is always $S_{sat}$, the ratio between the dynamic part and the static part of the total photon density has to be maximised. An photon density, optimised in terms to maximise the dynamic gratings, is obtained if the power of both input signals is equal.

ECLs, similar to what was done for the investigations in Fig. 3.9 the generated mode comb would only be a WDM carrier source.

### 5.2.1. Generation of Coherent CW Input Signals

In Sec. 5.1.2 a method for generating two coherent CW signals with a MZM has been presented. However, there are also other possibilities to generate two coherent CW input signals for the UL-SOA. E.g., with the help of a self pulsating (SP) 3-section distributed feedback (DFB) laser [106] where one of the DFB sections is driven electrically with a radio frequency (RF) sine signal (Fig. 5.10). If the frequency of

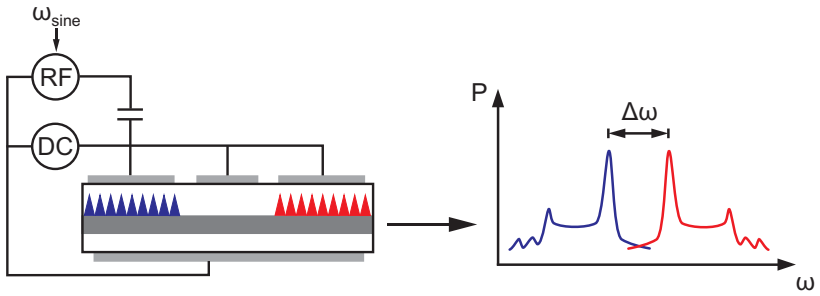


Figure 5.10.: Conceptual setup for generating two coherent modes; the RF-sine has to fulfil the condition $x\,\omega_{\text{sine}} = \Delta\omega$ with $x \in \mathbb{N}$ in order to obtain phase-locking of the two modes

the RF signal corresponds to the frequency detuning of the two DFB laser modes, the generated modes are phase locked. The laser can be even driven with a sub-harmonic of the modes' frequency detuning similar to [107]. Due to the concept with the sub-harmonics, also coherent frequency components with a frequency detuning corresponding to the frequency of the subharmonic are obtained at the output of the SP-laser. Hence, the channel spacing of the carrier source is tuneable in frequency steps corresponding to the frequency detuning of the SP-laser's modes divided by whole-numbers.

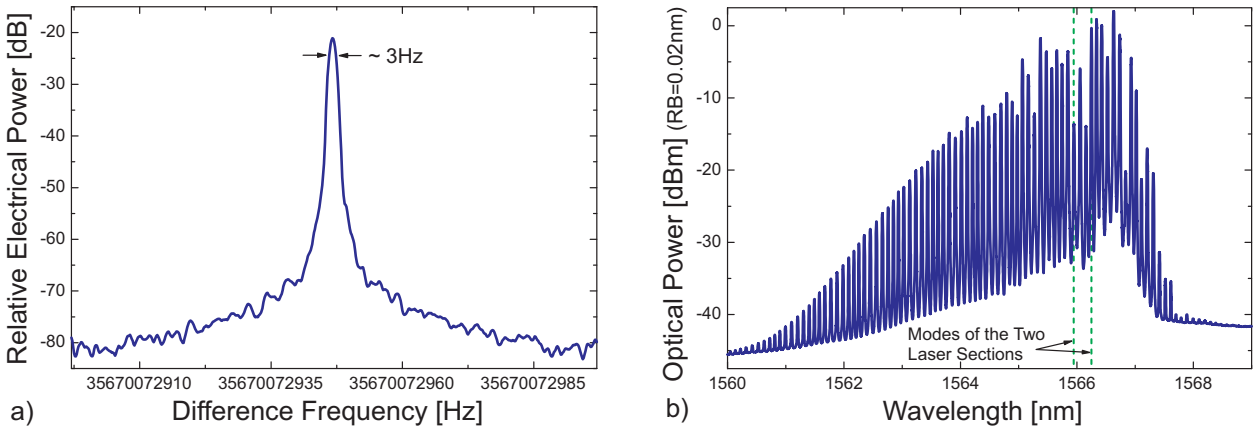


Figure 5.11.: Measured relative linewidth of the two modes' beating frequency generated by the SP-laser a) and spectrum at the UL-SOA's output b); the SP-laser has been driven with the 3rd sub-harmonic of the modes' detuning (modes' detuning = 35.67 GHz and driving frequency = 11.89 GHz); the measurements were done by the group of B. Sartorius from the *HHI*

To demonstrate the coherence of the two generated modes, Fig. 5.11a) shows a measured relative linewidth of 3 Hz for the beating frequency of the two modes generated by the RF-locked SP-laser. The linewidth of 3 Hz are due to the accuracy of the measurement equipment. For this reason, the signal to noise ratio (SNR) of the two modes' beating frequency spectrum is typically used to define the coherence of the two signals being approximately 50 dB. The laser was driven by a RF sine signal with the 3rd sub-harmonic. Fig. 5.11b) demonstrates that compared to Fig. 3.9 even with the sub-harmonic scheme similar mode combs at the UL-SOA's output with a mode spacing of the sub-harmonic can be obtained.

### 5.2.2. Results

In the following subsection, the quality of the generated mode comb at the UL-SOA's output in terms of OSNR and linewidth is investigated [2]. In a communication network these two parameters specify which modulation format can be used with the CoWDM carriers source. Moreover, the linewidth has a key role because it qualifies the coherence of the carriers. Since the coherence of the input signals is excellent (Sec. 5.2.1), the noise contribution of the UL-SOA is characterised in this subsection.

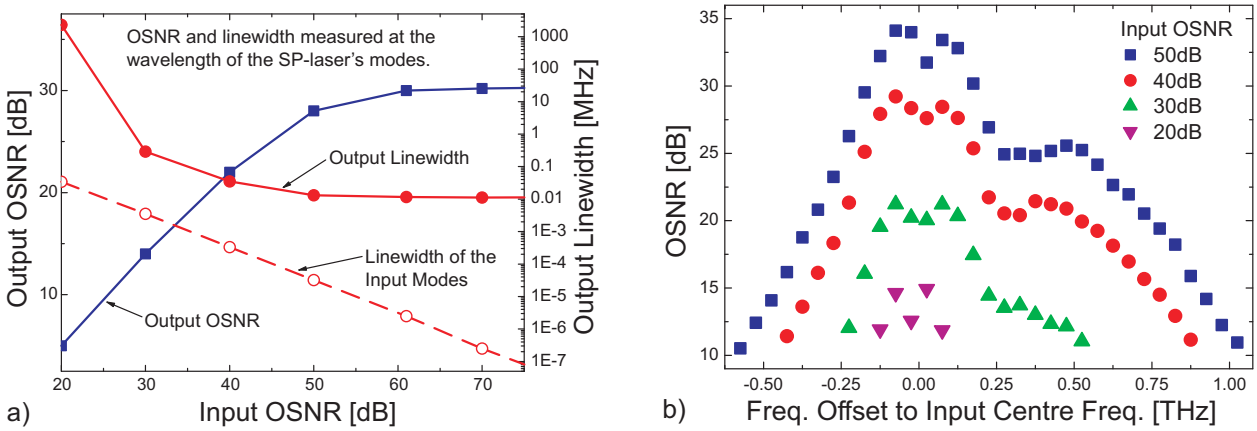


Figure 5.12.: Simulated OSNR and linewidth of the generated carriers for different noise levels of the SP-laser's input modes a); simulated OSNR of each generated carrier after the UL-SOA for different noise levels of the SP-laser's input modes b); the two input modes entered the UL-SOA around 0 THz frequency offset with a channel spacing of 50 GHz

Fig. 5.12a) shows the dependence of the OSNR and the linewidth at the UL-SOA's output on the input signals' noise level. With increasing input OSNR, the linewidth decreases and the output OSNR increases. At about 40 dB input OSNR, the linewidth and the output OSNR saturate because the noise contribution of the UL-SOA dominates the output noise behaviour while below 40 dB, the noise of the SP-laser dominates. Since the SP-laser from Sec. 5.2.1 has an OSNR of approximately 45 dB, the main contribution of the noise in the CoWDM carriers is generated by the UL-SOA. Furthermore, Fig. 5.12b) shows that with increasing noise level of the input modes, the number of generated carriers decreases. The effect can be ascribed to the deep saturation of the UL-SOA, since the overall optical power inside the device is limited by the saturation power. With an increasing noise level, larger amount of ASE contributes to the saturation power so less signal power contributes to the FWM generation reducing the FWM efficiency. Moreover, the best OSNR can be achieved around the wavelengths of the input modes.

Since the presented scheme allows larger channel spacings, Fig. 5.13 presents how the OSNR and the linewidth of the generated carriers depend on the channel spacing. A correlation between the OSNR and the linewidth can be observed so with decreasing OSNR, the linewidth increases. As a result, the coherence of the carriers reduces the farther the generated modes are away from the input modes. Moreover, with increasing channel spacing, the linewidth decreases and the OSNR increases. Again, the increasing OSNR can be ascribed to the limited saturation power of the UL-SOA. In this case, the total ASE power can be assumed to be independent of the channel spacings but the overall number of generated modes is dependent on the channel spacing since for smaller channel spacings the FWM efficiency increases. For this reason, the cascaded FWM processes can better generate new FWM products resulting in more generated modes (12.5 GHz ≡ 49 modes, 25 GHz ≡ 40 modes, 50 GHz ≡ 33 modes and 100 GHz ≡ 28 modes). Hence, the limited signal power splits over more generated modes for smaller channel spacings resulting in a lower OSNR of each generated carrier.

The presented scheme shows better performance in generating CoWDM carriers with larger channel

[2] To obtain the linewidth from a simulated spectrum the length of the simulated signal has to be increased in order to improve the spectral resolution. To calculate linewidths in the kilohertz-regime, the computation capacity is not sufficient. For this reason, the linewidth of the simulated signal has been obtained from the phase noise spectrum [108].

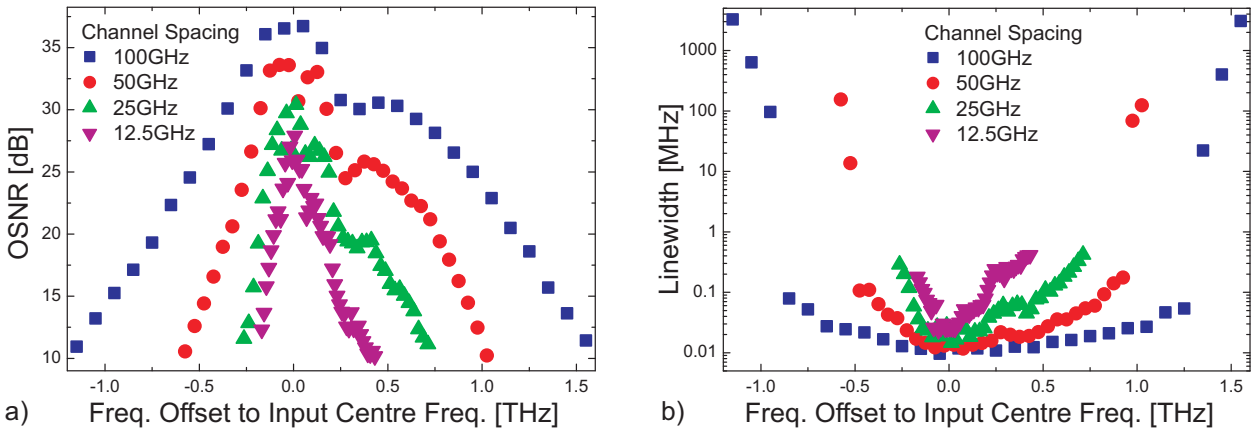


Figure 5.13.: Simulated OSNR a) and linewidth b) of each generated carrier after the UL-SOA for different channel spacing of the SP-laser input modes; the two input modes entered the UL-SOA around 0 THz frequency offset with an OSNR of 60 dB

spacing. Due to the concept of driving the SP-laser with a sub-harmonic RF signal of the channel spacing, the scheme should provide coherent carrier combs with large channel spacing without the need of high-bandwidth components. In general, larger channel spacings offer potential cost savings due to the reduced number of parallel channels to be transmitted. They also allow higher baud rates and thus more relaxed requirements concerning the linewidth of coherent transmission systems. However, as mentioned in Sec. 1.1, the trend is going to WDM systems with higher order modulation formats and baud rates of approximately 25 GBaud. Hence, only channel spacings of approximately 25 GHz are required. Moreover, the trend of low channel spacings is supported by CO-OFDM where coherent channels with a channel spacing of approximately 10 GHz are needed [59, 109]. In [110, 111], demands for the carrier quality for various modulation formats have been presented which are not reached by the CoWDM carrier source, presented here, for channel spacings of 25 GHz and below. The performance could be improved if the UL-SOA is optimised in terms of increased saturation photon density. Low coupling losses and higher optical input power also reduce the noise figure in the device and therefore increase the OSNR and reduce the linewidth.

# 6. Conclusion

The presented work discusses the important properties of ultralong semiconductor optical amplifiers (UL-SOAs) and some of their possible applications in optical communication systems.

At the beginning of this thesis the mathematical framework for the optical properties of UL-SOAs is presented. Based on this theoretical description, a simulation model is derived. The simulation model is an extension of an semiconductor optical amplifier (SOA) model [37–39] including some important properties of UL-SOAs.

E.g., the main part of the UL-SOA is saturated. Hence, the gain approximation has also to be exact for carrier densities close to the net transparency. Moreover, the bandwidth of the gain model is an important issue because the gain peak shifts due to the different carrier densities in the UL-SOA's amplifying and saturated section. For this reason, a gain approximation that properly represents the gain for various carrier densities over a broad bandwidth ($\sim$50 nm) is implemented in the simulation model.

Another important aspect of modelling UL-SOAs is its tremendous four-wave mixing (FWM) efficiency. UL-SOAs create broad FWM spectra up to a width of 30 nm because of the fast intraband effects in the saturated section. Although the FWM interactions in UL-SOAs are very complex the implementation can be simple if the simulation model is a full time-domain model. Due to the full time-domain modelling the dynamic gain and index gratings are implemented inherently. When modelling the nonlinear gain with the help of dynamic rate equations, the bandwidth of these effects will be implemented inherently too.

In the second part of the thesis some possible applications of UL-SOAs in optical communication systems have been investigated with the self-developed simulation tool. One of these possible applications is the generation of short pulses using the tremendous FWM efficiency of UL-SOAs. The concept is based on two co-polarised phase-locked continuous wave (CW) laser sources injecting light into an UL-SOA. If the CW laser sources are tuneable, the generated pulses at the output of the UL-SOA are also tuneable in the repetition rate and the carrier frequency of the pulses. According to calculations, a strong dependence of the pulsewidth on the CW signals mode spacing could be observed. With increasing mode spacing the repetition rate of the pulses increases and also the pulsewidth shortens.

The investigations yielded that the total mode spectrum, due to complex FWM interactions, has a nonlinear phase signature in the regime with high optical power. Therefore, no proper pulses can be obtained at the output of the UL-SOA. When mainly filtering the FWM modes with a linear phase signature from the combs shorter wavelength side, short pulses with full width half maximum (FWHM) of approximately 5 ps and a pulse repetition rate of 20 GHz have been generated. Moreover, even shorter pulses with FWHM less than 2 ps and a pulse repetition rate of 20 GHz can be obtained when the filter's slope is used to equalise the FWM modes making the modes from the linear phase regime more dominate. For shorter repetition rates of the pulses, even pulses in the sub-picosecond regime can be obtained.

When considering the propagation of short pulses in matter, the influence of chromatic dispersion has to be investigated. Compared to the waveguide dispersion, composite material dispersion (CMD) dominates the chromatic dispersion in SOAs over a wavelength region of 400 nm around the band gap. In turn, CMD itself is dominated by the material dispersion of the active region. For this reason, the mode confinement of the active region is an important parameter for the chromatic dispersion. Since the mode confinement is larger for a transverse electric (TE) mode than for a transverse magnetic (TM) mode,

CMD is also worse for a TE mode. The estimated chromatic dispersion of $30\,^{\mathrm{fs}}/_{\mathrm{mm\,nm}}$ around the band gap wavelength is in contrary to most estimations found in literature because of an inverse sign and its 10-times larger value [34,88]. The dependence of a carrier density change and a lattice temperature change on the chromatic dispersion has also been investigated. Although for both dependences the change of the material dispersion dominates, a strong dependence on the active region's mode confinement can be observed for a carrier density change, affecting CMD.

Another possible application of UL-SOAs is high-speed all-optical wavelength conversion (AOWC) with extinction ratio (ER) improvement. Due to the dominant fast intraband effects in the UL-SOA's saturated section and a co-polarised additional CW signal propagating with the data signal in the UL-SOA, the capability for all-optical signal processing with $100\,^{\mathrm{Gbit}}/_{\mathrm{s}}$ on-off keying (OOK) return to zero (RZ)-50% pseudo random bit sequence (PRBS) signals has been demonstrated. With an optimised device under proper driving conditions, bit pattern effects are negligible compared to the degradation due to amplified spontaneous emission (ASE). The suppression of the bit pattern effects can be ascribed to the additional CW signal operating as a holding beam.

Due to self-gain modulation (SGM) the ER of the data signal decreased after passing the UL-SOA making it useless for further transmission. Investigations of the UL-SOA's driving condition showed that the data signal's ER can be regenerated if the two input signals are co-polarised and the data signal has a shorter wavelength than the CW signal. These two and other driving conditions have indicated, that parametric amplification due to FWM (Bogatov-like effect) is the reason for the ER improvement. Due to simulations, preconditions for the analytic description of the Bogatov-like effect in the UL-SOA's saturated section could be obtained. With the help of this analytic description and further simulations, the mechanism of the ER improvement could be revealed: Due to the cross-gain modulated CW signal and the dependence of the Bogatov-like effect's intensity on this CW signal, the data signal's levels are amplified differently resulting in an ER improvement.

Moreover, due to the additional CW signal, AOWC is possible which can be combined with the ER improvement and the ability for high-speed signal processing to high-speed AOWC with ER improvement. The AOWC can be achieved with the help of cross-gain modulation (XGM) and FWM. Numerically, with the help of XGM as conversion mechanism, an ER improvement of 7 dB could be demonstrated while the signal has been converted over 4 nm to a shorter wavelength. Unfortunately, this wavelength conversion with ER improvement scheme is limited to down conversion, but when using FWM as conversion mechanism, up conversion is also possible. In this case, however, the ER improvement efficiency decreases and mainly compensates degrading effects.

In the proposed schemes, small fluctuations of the input power levels increase, since the ER improvement is realised with a steep slope of the nonlinear transfer characteristic. For this reason, 2R-regeneration can only be achieved if noise compression is done afterwards. Thus, at the present state the scheme should be regarded as AOWC due to XGM without degradation because of SGM. Furthermore, when just compensating this degradation with the Bogatov-like effect, the optical power of the wavelength converted signal is higher. As a result, slight noise compression is achieved because of SGM. Another problem with this scheme is the dependence on the signals polarisation. If a signal is transmitted over fibre its polarisation is unknown. However, to achieve the ER improvement the data signal and the CW signal have to be co-polarised. Typical polarisation division schemes can only be applied for the case where the AOWC with ER improvement is due to FWM and not due to XGM.

All in all, bulk UL-SOAs have some interesting properties that have the potential for applications in optical communication systems. Although the trend for short SOAs is towards multi-quantum well (MQW) devices, the possible applications presented here should be more pronounced in bulk UL-SOAs than in MQW UL-SOAs.

A major advantage of UL-SOAs is the ability for integration in combination with tuning the operation point. Compared to other integrated solutions that are typically based on Mach-Zehnder interferometers

(MZIs) and mode-locked lasers (MLLs), the operation point of UL-SOAs does not depend on their geometry. Of course, UL-SOAs also have disadvantages. E.g., the power consumption is high because of the device length. Estimating the electrical power consumption with 1 W for an optimised device plus another Watt for the cooling results in 20 pJ/bit for the 100 Gbit/s AOWC with ER improvement scheme excluding the power consumption of the additional CW laser source. Referring to [17], the value is about 10-times larger compared to typically electrical signal processing solutions.

Nevertheless, although UL-SOAs might not be used in commercial optical communication systems, within this work some analytic fundamentals with general benefit for the InGaAsP semiconductor community have been estimated. Moreover, some of the presented concepts might find their way into commercial applications in similar devices (e.g., quantum dot-devices) which do not suffer from the disadvantages of the bulk UL-SOAs.

# Bibliography

[1] L. Occhi, "Semiconductor Optical Amplifiers made of Ridge Waveguide Bulk InGaAsP/InP: Experimental Characterisation and Numerical Modelling of Gain, Phase, and Noise", Ph.D. thesis, ETH Zürich, 2002

[2] T. Durhuus, B. Mikkelsen, C. Joergensen, S. Lykke Danielsen and K. Stubkjaer, "All-optical wavelength conversion by semiconductor optical amplifiers", *J. Lightwave Technol.*, Vol. 14, No. 6, pp. 942-954, 1996

[3] C. Joergensen, S. Danielsen, K. Stubkjaer, M. Schilling, K. Daub, P. Doussiere, F. Pommerau, P. Hansen, H. Poulsen, A. Kloch, M. Vaa, B. Mikkelsen, E. Lach, G. Laube, W. Idler and K. Wunstel, "All-Optical Wavelength Conversion at Bit Rates Above 10 Gb/s Using Semiconductor Optical Amplifiers", *IEEE J. Sel. Top. Quantum Electron.*, Vol. 3, No. 5, pp. 1168-1180, 1997

[4] D. Wolfson, A. Kloch, T. Fjelde, C. Janz, B. Dagens and M. Renaud, "40 Gb/s All-Optical Wavelength Conversion, Regeneration and Demultiplexing in an SOA-Based All-Active Mach-Zehnder Interferometer", *IEEE Photon. Technol. Lett.*, Vol. 12, No. 3, pp. 332-334, 2000

[5] S. Diez, C. Schmidt, R. Ludwig, H.G. Weber, K. Obermann, S. Kindt, I. Koltchanov and K. Petermann, "Four-Wave Mixing in Semiconductor Optical Amplifiers for Frequency Conversion and Fast Optical Switching", *IEEE J. Sel. Top. Quantum Electron.*, Vol. 3, No. 5, pp. 1131-1145, 1997

[6] S. Fischer, M. Dülk, E. Gamper, W. Vogt, W. Hunziker, E. Gini, H. Melchior, A.Bxens, H.N. Poulsen and A.T. Clausen, "All-optical regenerative OTDM add/drop multiplexer at 40 Gb/s using a monolithic InP Mach-Zehnder interferometer", *IEEE Photon. Technol. Lett.*, Vol. 12, No. 3, pp. 335-337, 2000

[7] C. Schubert, J. Berger, U. Feiste, R. Ludwig, C. Schmidt and H.-G. Weber, "160 Gb/s polarization insensitive all-optical demultiplexing using a gain-transparent ultrafast-nonlinear interferometer (GT-UNI)", *Proc. OAA*, paper OWA4, Stresa, 2001

[8] H.-G. Weber, R. Ludwig, S. Ferber, C. Schmidt-Langhorst, M. Kroh, V. Marembert, C. Boerner and C. Schubert, "Ultrahigh-Speed OTDM-Transmission Technology", *IEEE J. Lightwave Technol.*, Vol. 24, No. 12, pp. 4616-4627, 2006

[9] A. Viglienzoni, "Evolution of Products and Enabling Technologies for Optical Networks", *Proc. Photonics in Switching '08*, Plenary 2, Sapporo, 2008

[10] J. Leuthold, B. Mikkelsen, R.E. Behringer, G. Raybon, J.L. Pleumeekers, C.H. Joyner and P.A. Besse, "Novel 3R regenerator based on semiconductor optical amplifier delayed-interference configuration", *Proc. OAA*, paper PD8, Stresa, 2001

[11] B. Sartorius, J. Slovak, C. Bornholdt and H.-P. Nolting, "Novel 3R Regenerator Architecture with Wavelength Flexible Output", *Proc. ECOC*, paper 6.3.3, Copenhagen, 2002

[12] G. Contestabile, R. Proietti, N. Calabretta and E. Ciaramella, "Cross-Gain Compression in Semiconductor Optical Amplifiers", *IEEE J. Lightwave Technol.*, Vol. 25, No. 3, pp. 915-921, 2007

[13] T. Fjelde, D. Wolfson, A. Kloch, C. Janz, A. Coquelin, I. Guillemot, F. Gaborit, F. Poingt, B. Dagens and M. Renaud, "10 Gb/s all-optical logic OR in monolithically integrated interferometric wavelength converter", *Electron. Lett.*, Vol. 36, No. 9, pp. 813-815, 2000

[14] K.E. Stubkjaer, "Semiconductor optical amplifier-based all-optical gates for high-speed optical processing", *IEEE J. Sel. Top. Quantum Electron.*, Vol. 6, No. 6, pp. 1428-1435, 2000

[15] S. Randel, A.M. Melo, K. Petermann, V. Marembert and C. Schubert, "Novel scheme for ultrafast all-optical XOR operation", *IEEE J. Lightwave Technol.*, Vol. 22, No. 12, pp. 2808-2815, 2004

[16] S.J. Savory, A. Napoli, B. Thomsen, P. Bayvel, and R.I. Killey, "Robust optical systems using maximum likelihood sequence estimators", *IEE Seminar on Optical Fibre Communications and Electronic Signal Processing*, 2005

[17] R.S. Tucker, "Energy and Switching", *Proc. Photonics in Switching '09*, Plenary 3, Pisa, 2009

[18] M.A. Summerfield and R.S. Tucker, "Frequency-Domain Model of Multiwave Mixing in Bulk Semiconductor Optical Amplifiers", *IEEE J. Sel. Top. Quantum Electron.*, Vol. 5, No. 3, pp. 839-849, 1999

[19] T. Silveira, A. Ferreira, A. Teixeira and P. Monteiro, "40 Gb/s Multichannel NRZ to CSRZ Format Conversion Using an SOA", *IEEE Photon. Technol. Lett.*, Vol. 20, No. 19, pp. 1597-1599, 2008

[20] K. Obermann, T. Liu, K. Petermann, F. Girardin and G. Guekos, "Saturation of semiconductor optical amplifiers due to amplified spontaneous emission", *Proc. CLEO*, paper CThN1, 1998

[21] F. Girardin, G. Guekos and A. Houbavlis, "Gain Recovery of Bulk Semiconductor Optical Amplifiers", *IEEE Photon. Technol. Lett.*, Vol. 10, No. 6, pp. 784-786, 1998

[22] C. Schmidt-Langhorst, C. Meuer, R. Ludwig, D. Puris, R. Bonk, T. Vallaitis, D. Bimberg, K. Petermann, J. Leuthold and C. Schubert, "Quantum-Dot Semiconductor Optical Booster Amplifier with Ultrafast Gain Recovery for Pattern-Effect Free Amplification of 80 Gb/s RZ-OOK Data Signals", *Proc. ECOC*, paper 6.2.1, Vienna, 2009

[23] H. Nolting, "All-optical signal processing using ultra-long SOAs", *Proc. OAA*, paper OTuB1, San Francisco, 2004

[24] M. Willatzen, A. Uskov J. Mørk, H. Olesen, B. Tromborg and A. Jauho, "Nonlinear gain suppression in semiconductor lasers due to carrier heating", *IEEE Photon. Technol. Lett.*, Vol. 3, No. 7, pp. 606-609, 1991

[25] A. Mecozzi and J. Mørk, "Saturation Effects in Nondegenerate Four-Wave Mixing Between Short Optical Pulses in Semiconductor Laser Amplifiers", *IEEE J. Sel. Top. Quantum Electron.*, Vol. 3, No. 5, pp. 1190-1207, 1997

[26] J.L. Pleumeekers, "POSEIDON: A simulator for optoelectronic semiconductor devices", Ph.D. thesis, Delft University of Technology, 1997

[27] M.J. Connelly, "Wide-Band Steady-State Numerical Model and Parameter Extraction of a Tensile-Strained Bulk Semiconductor Optical Amplifier", *IEEE J. Quantum Electron.*, Vol. 43, No. 1, pp. 47-56, 2007

[28] J. Leuthold, M. Mayer, J. Eckner, G. Guekos, H. Melchior and Ch. Zellweger, "Material gain of bulk 1.55 μm InGaAsP/InP semiconductor optical amplifiers approximated by a polynomial model", *J. Appl. Phys.*, Vol. 87, No. 1, pp. 618-620, 2000

[29] K. Obermann, "All-Optical Wavelength Conversion based on Cross-Gain Modulation and Four-Wave Mixing in Semiconductor-Optical Amplifiers", Ph.D. thesis, Wissenschaft & Technik Verlag, Berlin, 1998

[30] M. Marcuse, "Computer Model of an Injection Laser Amplifiers", *IEEE J. Quantum Electron.*, Vol. 19, No. 1, pp. 63-73, 1983

[31] J.M. Tang and K.A. Shore, "Active Picosecond Optical Pulse Compression in Semiconductor Optical Amplifiers", *IEEE J. Quantum Electron.*, Vol. 35, No. 1, pp. 93-100, 1999

[32] M. Radziunas, H.-J. Wünsche, B. Sartorius, O. Brox, D. Hoffmann, K.R. Schneider and D. Marcenac, "Modeling Self-Pulsating DFB Lasers with an Integrated Phase Tuning Section", *IEEE J. Quantum Electron.*, Vol. 36, No. 9, pp. 1026-1034, 2000

[33] J. Wang, A. Maitra, C. Poulton, W. Freude and J. Leuthold, "Temporal Dynamics of the Alpha Factor in Semiconductor Optical Amplifiers", *IEEE J. Lightwave Technol.*, Vol. 25, No. 3, pp. 891-900, 2007

[34] M.Y. Hong, Y.H. Chang, A. Dienes, J.P. Heritage, P.J. Delfyett, S. Dijaili and F.G. Patterson, "Femtosecond Self- and Cross-Phase Modulation in Semiconductor Laser Amplifiers", *IEEE J. Sel. Top. Quantum Electron.*, Vol. 2, No. 3, pp. 523-539, 1996

[35] N.K. Das, Y. Yamayoshi and H. Kawaguchi, "Analysis of Basic Four-Wave Mixing Characteristics in a Semiconductor Optical Amplifier by the Finite-Difference Beam Propagation Method", *IEEE J. Quantum Electron.*, Vol. 36, No. 10, pp. 1184-1192, 2000

[36] M. Razaghi, V. Ahmadi and M.J. Connelly, "Comprehensive Finite-Difference Time-Dependent Beam Propagation Model of Counterpropagating Picosecond Pulses in a Semiconductor Optical Amplifier", *IEEE J. Lightwave Technol.*, Vol. 27, No. 15, pp. 3162-3174, 2009

[37] M. Schell, "Erzeugung ultrakurzer Lichtpulse mit Halbleiterlasern: Theorie und Experiment", Ph.D. thesis, Technische Universität Berlin, 1994

[38] G. Toptchiyski, S. Kindt, K. Petermann, E. Hilliger, S. Diez and H.G. Weber, "Time-domain modeling of semiconductor optical amplifiers for OTDM applications", *IEEE J. Lightwave Technol.*, Vol. 17, No. 12, pp. 2577-2583, 1999

[39] A.M. Melo and K. Petermann, "Time-domain Amplified Spontaneous Emission Noise Model of Semiconductor Optical Amplifiers", *Proc. NUSOD*, paper ThC3, 2005

[40] S. Ben Yoo, "Optical Packet and Burst Switching Technologies for the Future Photonic Internet", *IEEE J. Lightwave Technol.*, Vol. 24, No. 12, pp. 4468-4492, 2006

[41] A. Kelly, A. Ellis, D. Nesset, R. Kashyap and D. Moodie, "1OO Gb/s wavelength conversion using FWM in an MQW semiconductor optical amplifier", *Electron. Lett.*, Vol. 34, No. 20, pp. 1955-1956, 1998

[42] H. Chayet, S. Ben Ezra, N. Shachar, S. Tzadok, S. Tsadka and J. Leuthold, "Regenerative all-optical wavelength converter based on semiconductor optical amplifier and sharp frequency response filter", *Proc. OFC*, paper ThS2, 2004

[43] J. Leuthold, L. Möller, J. Jaques, S. Cabot, L. Zhang, P. Bernasconi, M. Cappuzzo, L. Gomez, E. Laskowski, E. Chen, A. Wong-Foy and A. Griffin, "160 Gbit/s SOA all-optical wavelength converter and assessment of its regenerative properties", *Electron. Lett.*, Vol. 40, No. 9, pp. 554-555, 2004

[44] R.J. Manning, X. Yang, R.P. Webb, R. Giller, F.C. Garcia Gunning and A.D. Ellis, "The 'Turbo-Switch' – a Novel Technique to Increase the High-speed Response of SOAs for Wavelength Conversion", *Proc. OFC*, paper OWS8, 2006

[45] J. Leuthold, W. Freude, G. Boettger, J. Wang, P. Vorreau and A. Marculescu, "Trends in the field of all-optical wavelength conversion and regeneration for communication up to 160 Gb/s", *Proc. ECOC*, paper Tu.3.3.6, 2005

[46] U. Busolt, G. Bramann, H.-J. Wünsche, C. Schmidt, B. Sartorius, H.-P. Nolting and T. Rosin, "Two-Wave Competition for All-Optical Signal Processing: First Experimental Verification in Ultra-Long SOAs", *Proc. ECOC*, paper Th3.5.1, pp. 1060-1061, 2003

[47] G. Bramann, H.-J. Wünsche, U. Busolt, C. Schmidt, M. Schlak, B. Sartorius, H.-P. Nolting, "Two-Wave Competition in Ultralong Semiconductor Optical Amplifiers", *IEEE J. Quantum Electron.*, Vol. 41, No. 10, pp. 1260-1267, 2005

[48] H. Takara, T. Ohara, K. Mori, K. Sato, E. Yamada, Y. Inoue, T. Shibata, M. Abe, T. Morioka and K.-I. Sato, "More than 1000 channel optical frequency chain generation from single supercontinuum source with 12.5 GHz channel spacing", *Electron. Lett.*, Vol. 36, No. 25, pp. 2089-2090, 2000

[49] T. Inoue, N. Kumano, M. Takahashi, T. Yagi and M. Sakano, "Generation of 80 nm Wavelength-Tunable 100 fs Pulse Based on Comblike Profiled Fiber Comprised of HNLF and Zero Dispersion-Slope NZDSF", *IEEE J. Lightwave Technol.*, Vol. 25, No. 1, pp. 165-169, 2007

[50] H.A. Haus, K. Tamura, L. E. Nelson and E.P. Ippen, "Stretched-pulse additive pulse mode-locking in fiber ring lasers: theory and experiment", *IEEE J. Quantum Electron.*, Vol. 31, No. 3, pp. 591-598, 1995

[51] R. Kaiser, B. Hüttl, H. Heidrich, S. Fidorra, W. Rehbein, H. Stolpe, R. Stenzel, W. Ebert and G. Sahin, "Tunable Monolithic Mode-Locked Lasers on InP With Low Timing Jitter", *IEEE Photon. Technol. Lett.*, Vol. 15, No. 5, pp. 634-636, 2003

[52] K. Sato, K. Wakita, L. Kotaka, Y. Kondo and M. Yamamoto, "Monolithic strained-InGaAsP multiple-quantum-well lasers with integrated electroabsorption modulators for active mode locking", *Appl. Phys. Lett.*, Vol. 65, No. 1, pp. 1-3, 1994

[53] R.M. Woodward, B.E. Cole, V.P. Wallace, R.J. Pye, D.D. Arnone, E.H. Linfield and M. Pepper, "Terahertz pulse imaging in reflection geometry of human skin cancer and skin tNo.", *J. Phys. Med. Biol.*, Vol. 47, pp. 3853-3863, 2002

[54] D.M. Mittleman, R.H. Jacobsen and M.C. Nuss, "T-Ray Imaging", *IEEE J. Sel. Top. Quantum Electron.*, Vol. 2, No. 3, pp. 679-692, 1996

[55] C. Bornholdt, J. Slovak, B. Sartorius, M.Schlak and Ch. Schmidt, "Optical Comb Generator Using Pulse Compression in Ultra-Long Semiconductor Amplifiers", *Proc. ECOC*, paper Tu.1.5.5, 2005

[56] A.D. Ellis, F.C. Garcia Gunning and T. Healy, "Coherent WDM: The Achievement of High Information Spectral Density through Phase Control within the Transmitter", *Proc. OFC*, paper OThR4, 2006

[57] F. Inuzuka, K. Yonenaga, S. Yamamoto, E. Yamazaki and A. Takada, "Reduction of Nonlinear Interchannel Crosstalk Penalty for DQPSK signal in Carrier Phase Locked WDM", *Proc. ECOC*, paper 2.3.5, 2009

[58] F.C. Garcia Gunning, and A.D. Ellis, "Generation of a widely spaced optical frequency comb using an amplitude modulator pair", *Proc. SPIE OPTO-Ireland Symposium*, paper 5825B-74, 2005

[59] Y. Ma, Q. Yang, Y. Tang, S. Chen and W. Shieh, "1 Tb/s per Channel Coherent Optical OFDM Transmission with Subwavelength Bandwidth Access", *Proc. OFC*, paper PDPC1, 2009

[60] W. Shieh, H. Bao and Y. Tang, "Coherent optical OFDM: theory and design", *Opt. Exp.*, Vol. 16, No. 2, pp. 841-859, 2008

[61] W. Shieh, X. Yi, Y. Ma and Q. Yang, "Coherent optical OFDM: has its time come?", *J. Optical Net.*, Vol. 7, No. 3, pp. 234-255, 2008

[62] K.J. Ebeling, "Integrierte Optoelektronik", *Springer Verlag*, Berlin, 1989

[63] W.W. Chow and S.W. Koch, "Semiconductor – Laser Fundamentals", *Springer Verlag*, Berlin, 1999

[64] W.E. Lamb, "Theory of an Optical Maser", *Phys. Rev.*, Vol. 134, No. 6, pp. 1429-1450, 1964

[65] M. Asada and Y. Suematzu, "Density-Matrix Theory of Semiconductor Lasers with Relaxation Broadening Model – Gain and Gain-Suppression in Semiconductor Lasers", *IEEE J. Quantum Electron.*, Vol. 21, No. 5, pp. 434-442, 1985

[66] M. Osinski and M.J. Adams, "Gain spectra of quaternary semiconductors", *IEE Proc. Solid-State Electron Devices*, Vol. 129, pp. 229-236, 1982

[67] P.A. Wolff, "Theory of the band structure of very degenerate semiconductors", *Phys. Rev.*, Vol. 126, No. 2, pp. 405-412, 1962

[68] S. Adachi, "Physical Properties of III-V Semiconductor Compounds", *Wiley & Son*, New York, 1992

[69] J. Mark and J. Mørk, "Subpicosecond gain dynamics in InGaAsP optical amplifiers: Experiment and theory", *Appl. Phys. Lett.*, Vol. 61, No. 19, pp. 2281-2283, 1992

[70] K.L. Hall, G. Lenz, A.M. Darwish and E.P. Ippen, "Subpicosecond gain and index nonlinearities in InGaAsP diode lasers", *Optics Comm.*, Vol. 111, pp. 589-612, 1994

[71] A. Haug, "Free-carrier absorption in semiconductor lasers", *Semicond. Sci. Technol.*, Vol. 7, No. 19, pp. 373-378, 1992

[72] J. Mørk, J. Mark and C. Seltzer, "Carrier heating in InGaAsP laser amplifiers due to two-photon absorption", *Appl. Phys. Lett.*, Vol. 64, Issue 17, pp. 2206-2208, 1994

[73] A. Mecozzi and J. Mørk, "Saturation induced by picosecond pulses in semiconductor optical amplifiers", *J. Opt. Soc. America B*, Vol. 14, No. 4, pp. 761-770, 1997

[74] R. de L. Kronig, "On the theory of the dispersion of X-rays", *J. Opt. Soc. Am.*, Vol. 12, No. 6, pp. 547-557, 1926

[75] F. Stern, "Dispersion of the Index of Refraction Near the Absorbtion Edge of Semiconductors", *Phys. Rev. A*, Vol. 133, No. 6, pp. 1653-1664, 1964

[76] D.C. Hutchings, M. Sheik-Bahae, D.J. Hagan and E.W. Van Stryland, "Kramers-Krönig relations in nonlinear optics", *Opt. and Quantum Electron*, Vol. 24, pp. 1-30, 1992

[77] C.H. Henry, "Theory of the Linewidth of Semiconductor Lasers", *IEEE J. Quantum Electron.*, Vol. 18, No. 2, pp. 259-264, 1982

[78] L. Occhi, L. Schares and G. Guekos, "Phase Modeling Based on the $\alpha$-Factor in Bulk Semiconductor Optical Amplifiers", *IEEE J. Sel. Top. Quantum Electron.*, Vol. 9, No. 3, pp. 788-797, 2003

[79] B.R. Bennett, R.A. Soref and J.A. Del Alamo, "Carrier-Induced Change in Refractive Index of InP, GaAs and InGaAsP", *IEEE J. Quantum Electron.*, Vol. 26, No. 1, pp. 113-122, 1990

[80] J. Leuthold, "Advanced Indium-Phosphide Waveguide Mach-Zehnder Interferometer All-Optical Switches and Wavelength Converters", Series in Quantum Electronics Vol. 12, Hartung-Gorre Verlag, Konstanz, 1999

[81] N. Ogasawara and R. Ito, "Longitudinal Mode Competition and Asymmetric Gain Saturation in Semiconductor Injection Lasers. II. Theory", *Jpn. J. Appl. Phys.*, Vol. 27, pp. 615-626, 1988

[82] G.P. Agrawal and N.K. Dutta, "Long-Wavelength Semiconductor Laser", *van Nostrand Reinhold*, New York, 1986

[83] G.P. Agrawal and N.A. Olsson, "Self-Phase Modulation and Spectral Broadening of Optical Pulses in Semiconductor Laser Amplifiers", *IEEE J. Quantum Electron.*, Vol. 25, No. 11, pp. 2297-2306, 1989

[84] A. Kumar, K. Thyagarajan and A.K. Ghatak, "Analysis of rectangular-core dielectric waveguides: an accurate perturbation approach", *Opt. Lett.*, Vol. 8, No. 1, pp. 63-65, 1983

[85] C. Pollock and M. Lipson, "Integrated Photonics", *Kluwer Academic Publisher*, Boston, 2003

[86] C.H. Henry, "Determination of the Refractive Index of InGaAsP Epitaxial Layers Mode Line Luminescence Spectroscopy", *IEEE J. Quantum Electron.*, Vol. 21, No. 12, pp. 1887-1892, 1985

[87] H. Burkhard, H.W. Dinges and E. Kuphal, "Optical Properties of $In_{1-x}Ga_xP_{1-y}As_y$, InP, GaAs, and GaP Determined by Ellipsometry", *J. Appl. Phys.*, Vol. 53, No. 1, pp. 655-662, 1982

[88] K.L. Hall, G. Lenz and E.P. Ippen, "Femtosecond Time Domain Measurements of Group Velocity Dispersion in Diode Lasers at 1.5 μm", *IEEE J. Lightwave Technol.*, Vol. 10, No. 5, pp. 616–619, 1992

[89] A. Uskov, J. Mørk and J. Mark, "Wave Mixing in Semiconductor Laser Amplifiers Due to Carrier Heating and Spectral-Hole Burning", *IEEE J. Quantum Electron.*, Vol. 30, No. 8, pp. 1769-1781, 1994

[90] A. Melo, S. Randel and K. Petermann, "Mach-Zehnder Interferometer-Based High-Speed OTDM Add-Drop Multiplexing", *J. Lightwave Technol.*, Vol. 25, No. 4, pp. 1017-1026, 2007

[91] K. Inoue, "Technique to compensate waveform distortion in a gain-saturated semiconductor optical amplifier using a semiconductor saturable absorber", *Electron. Lett.*, Vol. 34, No. 4, pp. 376-378, 1998

[92] F. Öhman, S. Bischoff, B. Tromborg and J. Mørk, "Wave Mixing in Semiconductor Laser Amplifiers Due to Carrier Heating and Spectral-Hole Burning", *IEEE J. Quantum Electron.*, Vol. 40, No. 3, pp. 245-255, 2004

[93] A.D. Ellis, A.E. Kelly, D. Nesset, D. Pitcher, D.G. Moodie and R. Kashyap, "Error free 100 Gbit/s wavelength conversion using grating assisted cross-gain modulation in 2 mm long semiconductor amplifier", *Electron. Lett.*, Vol. 34, No. 20, pp. 1958-1959, 1998

[94] T. Watanabe, N. Sakaida, H. Yasaka, F. Kano and M. Koga, "Transmission performance of chirp-controlled signal by using semiconductor optical amplifier", *IEEE J. Lightwave Technol.*, Vol. 18, No. 8, pp. 1069-1077, 2000

[95] Y.R. Shen, "The Principles of Nonlinear Optics", *Wiley & Son*, New York, 1984

[96] K.Obermann, A. Mecozzi and J. Mørk, "Theory of four-wave mixing" in "Photonic Devices for Telecommunications", *Springer Verlag*, Berlin, 1998

[97] A. Bogatov, P. Eliseev and B. Sverdlov, "Anomalous interaction of spectral modes in a semiconductor laser", *IEEE J. Quantum Electron.*, Vol. 11, No. 7, pp. 510-515, 1975

[98] J.L. Pleumeekers, M. Kauer, K. Dreyer, C. Burrus, A.G. Dentai, S. Shunk, J. Leuthold and C.H. Joyner, "Acceleration of Gain Recovery in Semiconductor Optical Amplifiers by Optical Injection Near Transparency Wavelength", *IEEE Photon. Technol. Lett.*, Vol. 14, No. 1, pp. 12-14, 2002

[99] A. Matsumoto, K. Nishimura, K. Utaka and M. Usami, "Operational Design on High-Speed Semiconductor Optical Amplifier With Assist Light for Application to Wavelength Converters Using Cross-Phase Modulation", *IEEE J. Quantum Electron.*, Vol. 42, No. 3, pp. 313-323, 2006

[100] A. Capua, V. Mikhelashvili, G. Eisenstein, J. Reithmaier, A. Somers, A. Forchel, M. Calligaro, O. Parillaud, and M. Krakowski, "Direct observation of the coherent spectral hole in the noise spectrum of a saturated InAs/InP quantum dash amplifier operating near 1550 nm", *Opt. Exp.*, Vol. 16, No. 3, pp. 2141-2146, 2008

[101] P. Runge, R. Elschner, C.-A. Bunge, K. Petermann, M. Schlak, W. Brinker and B. Sartorius, "Operational Conditions for the Extinction Ratio Improvement in Ultralong SOAs", *IEEE Photon. Technol. Lett.*, Vol. 21, No. 2, pp. 106-108, 2009

[102] J. Leuthold, D.M. Marom, S. Cabot, J.J. Jaques, R. Ryf and C.R. Giles, "All-Optical Wavelength Conversion Using a Pulse Reformatting Optical Filter", *IEEE J. Lightwave Technol.*, Vol. 22, No. 1, pp. 186-192, 2004

[103] P. Noll, "Signale und Systeme", lecture notes, TU Berlin, 1999

[104] F. Kerbstadt and K. Petermann, "Analysis of adaptive dispersion compensators with double-AWG structures", *IEEE J. Lightwave Technol.*, Vol. 23, No. 3, pp. 1468-1477, 2005

[105] Y. Miyamoto, A. Hirano, K. Yonenaga, A. Sano, H. Toba, K. Murata and O. Mitomi, "320 Gbit/s (8×40 Gbit/s) WDM transmission over 367 km with 120 km repeater spacing using carrier-suppressed return-to-zero format", *Electron. Lett.*, Vol. 35, No. 23, pp. 2041-2042, 1999

[106] U. Bandelow, M. Radziunas, J. Sieber and M. Wolfrum, "Impact of Gain Dispersion on the Spatio-Temporal Dynamics of Multisection Lasers", *IEEE J. Quantum Electron.*, Vol. 37, No. 2, pp. 183-188, 2001

[107] M. Gotoda, S. Nishikawa, T. Nishimura and Y. Tokuda, "Successful demonstration of subharmonic injection locking for phase shifted self-pulsating DFB lasers at 168 GHz and beyond", *Proc. OFC 04*, paper MF54, 2004

[108] N. Schunk and K. Petermann, "Minimum Bit Rate of DPSK Transmission for Semiconductor Laser with a Long External Cavity and Strong Linewidth Reduction", *IEEEJ. Lightwave Technol.*, Vol. 5, No. 9, pp. 1309-1314, 1987

[109] S. Chandrasekhar, X. Liu, B. Zhu and D.W. Peckham, "Transmission of a 1.2-Tb/s 24-Carrier No-Guard-Interval Coherent OFDM Superchannel over 7200-km of Ultra-Large-Area Fiber", *Proc. ECOC*, paper PD2.6, 2009

[110] E. Ip, A. Pak Tao Lau, D.J.F. Barros and J.M. Kahn, "Coherent detection in optical fiber systems", *Opt. Exp.*, Vol. 16, pp. 753-791, 2008

[111] I. Fatadin, D. Ives and S.J. Savory, "Laser Linewidth Tolerance for 16-QAM Coherent Optical Systems Using QPSK Partitioning", *IEEE Photon. Technol. Lett.*, Vol. 22, No. 9, pp. 631-633, 2010

[112] R.E. Nahory, M.A. Pollack, W.D. Johnston, and R.L. Barns, "Band gap versus composition and demonstration of Vegard's law for $In_{1-x}Ga_xAs_yP_{1-y}$ lattice matched to InP", *Appl. Phys. Lett.*, Vol. 33, Issue 7, pp. 659-661, 1978

[113] N.G. Nilsson, "Empirical approximation for the Fermi energy in a semiconductor with parabolic bands", *Appl. Phys. Lett.*, Vol. 33, Issue 7, pp. 653-654, 1978

[114] D. Bimberg and J. Mycielski, "Recombination-induced heating of free carriers in a semiconductor", *Phys. Rev. B*, Vol. 31, Issue 8, pp. 2363-2373, 1985

[115] B. Gomatam and A. DeFonzo, "Theory of Hot Carrier Effects on Nonlinear Gain in GaAs-GaAlAs Lasers and Amplifiers", *IEEE J. Quantum Electron.*, Vol. 26, Issue 10, pp. 1689-1704, 1990

[116] J. Tang and K. Shore, "Strong picosecond optical pulse propagation in semiconductor optical amplifiers at transparency", *IEEE J. Quantum Electron.*, Vol. 34, Issue 7, pp. 1263-1269, 1998

[117] J. Mørk and J. Mark, "Time-resolved spectroscopy of semiconductor laser devices: Experiments and modelling", *SPIE Inter. Soc. Opt. Engineering*, Vol. 2399, pp. 146-159, 1995

[118] A.B. Djurišić, A.D. Rakić, P.C.K. Kwok, E.H. Li and M.L. Majewski, "Modeling the optical constants of GaP, InP, and InAs", *J. Appl. Phys.*, Vol. 85, Issue 7, pp. 3638-3642, 1999

[119] M.A. Afromowitz, "Refractive index of $Ga_{1-x}Al_xAs$", *Solid State Commun.*, Vol. 15, Issue 10, pp. 59-63, 1974

[120] C. Tanguy, "Refractive Index of Direct Bandgap Semiconductors near the Absorption Threshold: Influence of Excitonic Effects", *IEEE J. Quantum Electron.*, Vol. 32, Issue 10, pp. 1746-1751, 1996

[121] H.C. Casey, D.D. Sell and M.B. Panish, "Refractive index of $Al_xGa_{1-x}As$ between 1.2 and 1.8 eV", *Appl. Phys. Lett.*, Vol. 24, Issue 2, pp. 63-65, 1974

[122] Y. Kokuboa and I. Ohta, "Refractive index as a function of photon energy for AlGaAs between 1.2 and 1.8 eV", *J. Appl. Phys.*, Vol. 81, Issue 4, pp. 2042-2043, 1997

[123] K. Petermann, "Laser diode modulation and noise", *Kluwer Academic Publishers*, Dordrecht, 1988

[124] G. Agrawal, "Population pulsations and nondegenerate four-wave mixing in semiconductor lasers and amplifiers", *J. Opt. Soc. Amer. B*, Vol. 5, Issue 1, pp. 147-159, 1988

# A. List of Acronyms

**2R** re-amplification, re-shaping

**AOWC** all-optical wavelength conversion

**ASE** amplified spontaneous emission

**AWG** arrayed waveguide grating

**CMD** composite material dispersion

**CDP** carrier density pulsation

**CH** carrier heating

**CO-OFDM** coherent optical orthogonal frequency division multiplexing

**CoWDM** coherent wavelength division multiplexing

**CW** continuous wave

**DFB** distributed feedback

**ECL** external cavity laser

**EDFA** erbium doped fibre amplifier

**ER** extinction ratio

**FCA** free carrier absorption

**FIR** finite impulse response

**FWM** four-wave mixing

**FWHM** full width half maximum

**HNLF** highly nonlinear fibre

**MLL** mode-locked laser

**MQW** multi-quantum well

**MWM** multi-wave mixing

**MZI** Mach-Zehnder interferometer

**MZM** Mach-Zehnder modulator

**OOK** on-off keying

**OSA** optical spectrum analyser

**OSNR** optical signal to noise ratio

**OSO** optical sampling oscilloscope

**OTDM** optical time-division multiplexing

**PRBS** pseudo random bit sequence

**QD** quantum dot

**RF** radio frequency

**RZ** return to zero

**SE** spontaneous emission

**SGM** self-gain modulation

**SHB** spectral hole burning

**SLA** semiconductor laser amplifier

**SNR** signal to noise ratio

**SOA** semiconductor optical amplifier

**SP** self pulsating

**SPM** self-phase modulation

**TE** transverse electric

**TM** transverse magnetic

**TPA** two-photon absorption

**TSML** tuneable single mode laser

**UL-SOA** ultralong semiconductor optical amplifier

**WDM** wavelength division multiplexing

**XGM** cross-gain modulation

**XPM** cross-phase modulation

# B. UL-SOA's Simulation Parameters

## B.1. Physical Constants

| Symbol | Value | Description |
|---|---|---|
| $c_0$ | 299792458 m/s | speed of light in vacuum |
| $h$ | 6.626069311 $10^{-34}$ J s | Planck constant ($\hbar = h/2\pi$) |
| $e$ | 1.60217733 $10^{19}$ C | electron charge |
| $m_0$ | 9.1093897 $10^{-12}$ kg | electron rest mass |
| $\varepsilon_0$ | 8.854187817 $10^{-12}$ F/m | permittivity in vacuum |
| $\mu_0$ | 1.256637 $10^{-6}$ H/m | permeability in vacuum |
| $k_B$ | 1.380658 $10^{-23}$ J/K | Boltzmann constant |

Table B.1.: Physical constants used within this work

## B.2. Material Parameters

The operating wavelength of the semiconductor depends on the band gap wavelength. With the help of the material composition of $In_{1-x}Ga_xAs_yP_{1-y}$, the band gap energy can be tuned [112]

$$E_{\text{gap}\,0} = e\left(1.35 - 0.72y + 0.12y^2\right) \text{ at } 300\,\text{K}. \tag{B.1}$$

Furthermore, fine-tuning while operation is due to the lattice temperature [1] and the carrier density possible [67, 68]

$$E_{\text{gap}\,T_L} = E_{\text{gap}\,0} + e\frac{-0.4 + 0.03y}{1000}\Delta T_L \tag{B.2a}$$

$$E_{\text{gap}} = E_{\text{gap}\,T} + e\frac{\mathrm{d}E_{\text{gap}}}{\mathrm{d}N}N^{1/3} \tag{B.2b}$$

with $\frac{\mathrm{d}E_{\text{gap}}}{\mathrm{d}N} = -0.910^{-10}\,\text{eVm}$.

When designing semiconductor devices it is important that the material is unstrained in order to avoid tension inside the material [2]. Since the substrate wafer is made of InP, all $In_{1-x}Ga_xAs_yP_{1-y}$ layers being grown on this substrate should fulfil the lattice match condition

$$x = \frac{0.4562y}{1 - 0.031y}. \tag{B.3}$$

[1] In Eq. B.2a the band gap wavelength changes with approximately 1 nm/K being about 10-times more than the value obtained from measurements. For this reason, the denominator of Eq. B.2a is multiplied with 10 for the investigations of this thesis.

[2] On the other hand the stress can be used in thin device structures like MQW-devices to change optical properties like polarisation dependence.

Depending on the material composition the effective mass of the carriers in the conduction and the valence band also vary

$$m_e = m_0\,(0.08 - 0.039y) \tag{B.4a}$$
$$m_{hh} = m_0\,\{(1-y)(0.79x + 0.45(1-x)) + y\,(0.45x + 0.4(1-x))\} \tag{B.4b}$$
$$m_{lh} = m_0\,\{(1-y)(0.14x + 0.12(1-x)) + y\,(0.08x + 0.026(1-x))\}\,. \tag{B.4c}$$

The Fermi-levels in the conduction and the valence band can be calculated [113]

$$\mu_c(N) = \left\{\ln\delta + \delta\left(64 + 0.05524\delta\left(64 + \sqrt{\delta}\right)\right)^{-1/4}\right\} kT + E_{\text{gap}} \tag{B.5a}$$
$$\mu_v(P) = -\left\{\ln\varepsilon + \varepsilon\left(64 + 0.05524\varepsilon\left(64 + \sqrt{\varepsilon}\right)\right)^{-1/4}\right\} kT \tag{B.5b}$$

where $\rho = \frac{N}{n_c}$ and $\varepsilon = \frac{P}{n_v}$. $n_c$ and $n_v$ are the effective density of states for the conduction and valence band respectively given by

$$n_c = 2\left(\frac{m_e k T_L}{2\pi\hbar^2}\right)^{3/2} \qquad \text{and} \qquad n_v = 2\left(\frac{m_{dh} k T_L}{2\pi\hbar^2}\right)^{3/2} \tag{B.6}$$

and $m_{dh} = \left(m_{hh}^{3/2} + m_{lh}^{3/2}\right)^{2/3}$. The semiconductor, investigated in this thesis, is an intrinsic semiconductors ($N = P$).

To calculated the wavelength dependent gain (Eq. 2.8), the enrgy of the split-off band and the squared dipole matrix element are needed [26]

$$\Delta_{\text{s.o.}} = e\,\left(0.119 + 0.3\,y + 0.107\,y^2\right) \tag{B.7a}$$
$$\left|M_{\text{avg}}\right|^2 = \frac{m_0}{6}\,\frac{m_0 - m_e}{m_e}\,\frac{E_{\text{gap}}\left(E_{\text{gap}} + \Delta_{\text{s.o.}}\right)}{E_{\text{gap}} + \frac{2}{3}\Delta_{\text{s.o.}}}. \tag{B.7b}$$

## B.3. Simulation Parameters

The simulation parameters (Tab. B.2) are chosen to match with the 8 mm-long UL-SOA fabricated at the Heinrich-Hertz-Institut (Fig. B.1) because some of the simulations presented in this thesis are verified by experiments done with this device. The presented experiments were also performed at the Heinrich-Hertz-Institut.


Figure B.1.: Packaged 8 mm-long UL-SOA module (left) fabricated and assembled at the Heinrich-Hertz-Institut; the 8 mm-long UL-SOA chip is mounted on a heat sink (right) and is connected electrically from the top with wire bonds and optically from the left and right due to fibre coupling

| Symbol | Value | Description |
|---|---|---|
| $\Delta t$ | 25 $10^{-15}$ s | sampling interval |
| $\frac{dg}{dN}$ | 3.0 $10^{-20}$ $m^2$ | differential gain |
| $N_{tr}$ | 0.9 $10^{24}$ $m^{-3}$ | material transparent carrier density |
| $\bar{a}$ | 0.5 | linear gain fitting coefficient |
| $\omega_{gap}$ | 1.205 $10^{15}$ 1/s | band gap wavelength ($\lambda_{gap}$ = 1.565 $10^{-6}$ m) |
| $\omega_0$ | 1.207 $10^{15}$ 1/s | reference wavelength ($\lambda_0$ = 1.560 $10^{-6}$ m) |
| $C_\omega$ | 2.5 $10^{-11}$ $m^3$/s | peak frequency shift coefficient |
| $\omega_{z0}$ | 1.168 $10^{15}$ 1/s | begin of zero gain region ($\lambda_{z0}$ = 1.615 $10^{-6}$ m) |
| $z_0$ | -1.935 $10^{-12}$ 1/s | zero gain frequency shift coefficient |
| $\omega_{shift}$ | 1.548 $10^{15}$ 1/s | correction of gain peak |
| $\bar{b}$ | 0.65 | gain peak shift fitting coefficient |
| $n_G$ | 3.56 | group index |
| $\alpha_{int}$ | 2250 1/m | internal loss |
| $w$ | 1.2 $10^{-6}$ m | active region width |
| $d$ | 0.2 $10^{-6}$ m | active region height |
| $\Gamma$ | 0.38 | mode confinement factor |
| $\Gamma_{TPA}$ | 1.2 | TPA confinement factor |
| $A_{nr}$ | 1.25 $10^8$ 1/s | unimolecular non-radiative recombination coefficient |
| $B_{sp}$ | 2.5 $10^{-16}$ $m^3$/s | bimolecular spontaneous radiative recombination coefficient |
| $C_{Auger}$ | 0.9 $10^{-40}$ $m^6$/s | Auger recombination coefficient |
| $\tau_{CH}$ | 850 $10^{-15}$ s | carrier heating time constant |
| $\tau_{SHB}$ | 125 $10^{-15}$ s | spectral hole burning time Constant |
| $\epsilon_{CH}$ | 0.6 $10^{-23}$ $m^3$ | gain-suppression coefficient (CH) |
| $\epsilon_{SHB}$ | 0.5 $10^{-23}$ $m^3$ | gain-suppression coefficient (SHB) |
| $\epsilon_{FCA}$ | 0.1 $10^{-24}$ $m^3$ | gain-suppression coefficient (FCA) |
| $\epsilon_{TPA}$ | 1.25 $10^{-23}$ $m^3$ | gain-suppression coefficient (TPA) |
| $\beta_{TPA}$ | 3.5 $10^{-10}$ m/W | TPA coefficient |
| $\alpha_{CH}$ | 3.5 | linewidth enhancement factor (CH) |
| $\alpha_{SHB}$ | 0.1 | linewidth enhancement factor (SHB) |
| $\alpha_{FCA}$ | 0.1 | linewidth enhancement factor (FCA) |
| $\alpha_{TPA}$ | -2.25 | linewidth enhancement factor (TPA) |
| $\alpha_{CDP}$ | 5 | linewidth enhancement factor (CDP) |
| $L_{coup}$ | 8 dB | coupling losses |
| $I/l$ | 300 mA/mm | current per length |

Table B.2.: Default simulation parameters of the UL-SOAs; the parameters have been taken from [25, 28, 38, 47]

# C. Derivation of the Intrabands' Rate Equations

For modelling SOAs, the semiconductor's gain is an important parameter because the signal's amplitude change and even the signal's phase change can be calculated with the help of the $\alpha$-factor (Sec. 2.1.4) from the amplitude change. The gain variation of the gain peak's wavelength due to CDP can already be described due to Eq. 2.13 and a rate equation (Eq. 2.12). Having similar rate equations for the gain of CH and SHB reduces the calculation complexity of the simulation model significantly.

In quasi-equilibrium the carrier density distribution of a semiconductor's band can be easily described with the Fermi-Dirac distribution (Sec. 2.1). This quais-equilibrium can be distorted by stimulated emission and absorption causing SHB, CH and CDP (Sec. 2.1.2). SHB is a distortion of the carrier density distribution from the Fermi-Dirac distribution. The change of the carrier density distribution due to CH can be calculated with an increased temperature in the Fermi-Dirac distribution and for CDP with a change of the carrier density in the Fermi-Dirac distribution [24, 69]. For this reason, the inner energy $U$ is introduced

$$U_c = \int_0^\infty E_c^{xh} D_c f_c \, \mathrm{d}E_c^{xh} \tag{C.1a}$$

$$U_v = \int_{-\infty}^0 \left(D_v^{hh} + D_v^{lh}\right) E_v^{xh} f_v \, \mathrm{d}E_v^{xh} \tag{C.1b}$$

being the first moment of the carrier distribution.

The carrier dynamics in Eqs. C.2 are given by [69, 72] with $E_{1,\beta}$ and $E_{2,\beta}$ being the energy levels for one and two photons, respectively and $\omega_1$ is the frequency related to $E_{1,\beta}$. The descriptions of the other variables are given in Table B.2.

$$\frac{\partial U_\beta}{\partial t} = (\underbrace{\sigma_\beta N \hbar \omega_0}_{\text{FCA}} - \underbrace{g E_{\beta,0}}_{\substack{\text{stim. emission} \\ \& \text{ absorption}}} ) v_\mathrm{G} S + \underbrace{\frac{\Gamma_\mathrm{TPA}}{w\,d} v_\mathrm{G} \kappa \beta_\mathrm{TPA} E_{2,\beta} S^2}_{\text{TPA}} - \underbrace{\frac{U_\beta - U_{L\beta}}{\tau_{\mathrm{CH},\beta}}}_{\text{CH}} \tag{C.2a}$$

$$\frac{\partial \rho_\beta}{\partial t} = -\frac{\rho_\beta - \bar{\rho}_\beta}{\tau_{\mathrm{SHB},\beta}} - v_\mathrm{G} g S \tag{C.2b}$$

The index $\beta$ can be replaced by $c$ and $v$ representing the conduction and valence band, respectively. All effects are dominated by the slower conduction band electrons due to their smaller mass. For this reason, the calculations only have to be done for the conduction band.

Eq. C.3 is the linear expansion of the energy density $U$ with respect to the carrier density $N$ and the carrier temperature $T$ [114].

$$\frac{\partial U}{\partial t} = \left(\frac{\partial U}{\partial N}\right)_T \frac{\partial N}{\partial t} + \left(\frac{\partial U}{\partial T}\right)_N \frac{\partial T}{\partial t} \tag{C.3}$$

According to [115] the cooling rate can be derived from Eq. C.2a and Eq. C.3 [116]:

$$\frac{\partial T}{\partial t} = \left(\frac{\partial U}{\partial T}\right)_N^{-1} \left(\frac{\sigma N \hbar \omega_0}{g} - E_0 + \left(\frac{\partial U}{\partial N}\right)_T\right) v_G g S + \left(E_2 - \left(\frac{\partial U}{\partial N}\right)_T\right) \frac{\Gamma_{TPA}}{w d} \kappa \beta_{TPA} v_G S^2 - \frac{T - T_L}{\tau_{CH}} \tag{C.4}$$

Usually, when modelling SOAs, the contribution of TPA to CH is negligible because in short SOAs, TPA has a mentionable influence only for very high photon densities. At these high photon densities the carrier temperature is significantly increased and the Fermi-distribution approach breaks down. Hence, Eq. C.4 is no longer valid [117]. However, due to the long interaction length in UL-SOAs, TPA does have an impact for moderate carrier temperatures. In this case, Eq. C.4 can be used.

In the style of [25] the gain dynamics in Eqs. 2.14 are derived for the wavelength at the gain peak. Different from [25], the actual carrier density should be used in Eq. 2.14b since the carrier density in UL-SOAs varies significantly along the propagation direction. The corresponding gain suppression factors are given in Eqs. C.5.

$$\epsilon_{CH} = -v_G \tau_{CH} \frac{\partial g}{\partial T} \left(\frac{\partial U}{\partial T}\right)_N^{-1} \left(\left(\frac{\partial U}{\partial N}\right)_T - E_0\right) \tag{C.5a}$$

$$\epsilon_{FCA} = -v_G \tau_{CH} \frac{\partial g}{\partial T} \left(\frac{\partial U}{\partial T}\right)_N^{-1} \sigma \hbar \omega_0 \left(\frac{dg}{dN}\right)^{-1} \tag{C.5b}$$

$$\epsilon_{TPA} = -v_G \tau_{CH} \frac{\partial g}{\partial T} \left(\frac{\partial U}{\partial T}\right)_N^{-1} \left(E_2 - \left(\frac{\partial U}{\partial N}\right)_T\right) \tag{C.5c}$$

$$\epsilon_{SHB} = v_G \tau_{SHB} \frac{dg}{dN} \tag{C.5d}$$

# D. Calculation of the Refractive Index of InGaAsP

The refractive index of every $In_{1-x}Ga_xAs_yP_{1-y}$ composition can be calculated from the refractive indices of the binary constituents and Vegard's rule

$$\begin{aligned} X_{In_{1-x}Ga_xAs_yP_{1-y}} = &(1-x)(1-y)X_{InP} + (1-x)y\,X_{InAs} \\ &+ x(1-y)X_{GaP} + xy\,X_{GaAs}. \end{aligned} \tag{D.1}$$

[87] states that taking $(\varepsilon-1)/(\varepsilon+2)$ as a quantity for $X$ yields the best results. The permittivity $\varepsilon$ used in the calculations for GaP and InP has been taken from [118] and for GaAs from [119, 120]. Since in literature no approximation for the permittivity of InAs could be found that is accurate around the direct band gap energy, the refractive index of InAs has been fitted to the measured data in [87]

$$n_{InAs}(E) = 3.44 - 0.065\,E + 0.14\,E^2 + 0.038\,E^3 + \frac{0.00025}{(E-0.35)^2 + 0.0022} \tag{D.2}$$

where the photon energy $E$ has the unit eV. The formula has been taken from [122] (Eq. (11)) and creates a smoother shape of the refractive index around the band gap energy like in [121]. The smoothing seems to be appropriate because the refractive index of InAs in [87] is spiky due to missing data. From the refractive index of InAs the permittivity can be calculated with $\varepsilon \approx n^2$. Fig. D.1 shows the refractive index of the binary constitutes and the calculated refractive index of $In_{1-x}Ga_xAs_yP_{1-y}$ with the method of [87] where $y = 0.88$ and $x = 0.41$.

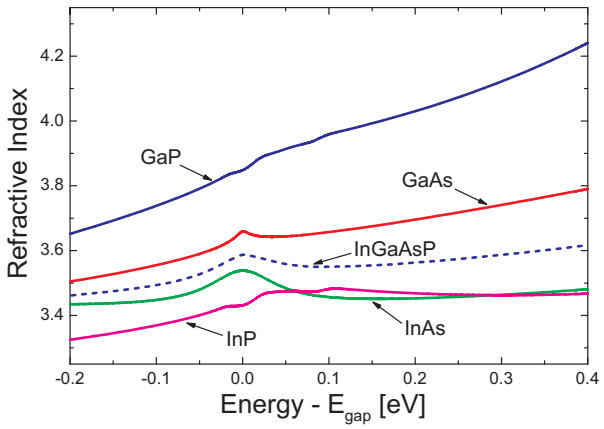


Figure D.1.: Refractive indices of the four binaries InGaAsP consists of; the dashed line indicates the calculated refractive index of $In_{1-x}Ga_xAs_yP_{1-y}$ with the method of [87] where $y = 0.88$ and $x = 0.41$; 0.1 eV correspond approximately 200 nm around the wavelength of 1550 nm

# E. Derivation of the Simulation Model's FIR Coefficients

In this subsection the complex FIR filter coefficients, that are needed for the propagation equation (Eq. 2.28), are derived.

Applying the Fourier transformation on the time-domain propagation equation (Eq. 2.28) yields the propagation equation in the frequency domain:

$$E^{\pm}_{x,y}(z \pm \Delta z, \omega) e^{-i\omega\Delta t} = G\left(z \pm \frac{\Delta z}{2}, \omega\right) \cdot E^{\pm}_{x,y}(z, \omega) + E^{\pm}_{\mathrm{SE}\,x,y}\left(z \pm \frac{\Delta z}{2}, \omega\right) \tag{E.1}$$

For further derivation only one segment of the SOA is regarded exemplary so the spatial dependence of the variables can be excluded in order to simplify the equations. The same calculation can be done in each segment with the corresponding variables of the segment. The FIR filter's gain function for the field is written as

$$G(\omega) = (c_1 + c_2 \exp(i\,(\omega - \omega_0)\,\Delta t)) \exp(i\Delta\phi) \tag{E.2}$$

where the filter coefficient $c_2$ is a complex value and $c_1$ is assumed to be real. Relating the FIR filter's gain function (Eq. E.2) to the power, the following equation can be obtained:

$$\begin{aligned} |G(\omega)|^2 = {} & c_1^2 + \mathrm{Re}(c_2)^2 + \mathrm{Im}(c_2)^2 + 2c_1\mathrm{Re}(c_2) \\ & \cdot \cos(\Delta\omega\,\Delta t) + 2c_1\mathrm{Im}(c_2)\sin(\Delta\omega\,\Delta t) \end{aligned} \tag{E.3}$$

The advanced cubic material gain approximation is given in Eq. 3.7. Due to the difference frequency concept, the cubic gain model has to be related to $\Delta\omega$. The advanced cubic material gain is needed in order to calculate the power related net gain of the propagating signals:

$$|G(\omega)|^2 = \exp\left(\left(\Gamma g_{\mathrm{cub}}(\Delta\omega) - \alpha_{\mathrm{int}}\right)\Delta z\right) \tag{E.4}$$

The equation for the net gain is a result of the differential equation 2.28. Equating Eq. E.4 and Eq. E.3 and expanding both sides with the help of the Taylor series around $\omega_0$, a polynomial comparison can be done. After some calculations the FIR coefficients can be obtained:

$$c_1 = \sqrt{\frac{a}{2} + d + \sqrt{\frac{a^2}{4} - b^2 + ad}} \tag{E.5a}$$

$$c_2 = -\frac{d}{c_1} - j\frac{b}{c_1} \tag{E.5b}$$

with $a$, $b$ and $d$ are defined as follows:

$$a = 1 + \Delta z \left(\Gamma\Delta\omega_z^2 \left(\frac{3\,g_{\mathrm{peak}\,2}}{\left(\Delta\omega_z - \Delta\omega_{\mathrm{peak}\,2}\right)^2} - \frac{2\,g_{\mathrm{peak}\,3}\,\Delta\omega_z}{\left(\Delta\omega_z - \Delta\omega_{\mathrm{peak}\,3}\right)^3}\right) - \alpha_{\mathrm{int}}\right) \tag{E.6a}$$

$$b = 3\Gamma\frac{\Delta z}{\Delta t}\Delta\omega_z \left(\frac{g_{\mathrm{peak}\,2}}{\left(\Delta\omega_z - \Delta\omega_{\mathrm{peak}\,2}\right)^2} - \frac{g_{\mathrm{peak}\,3}\,\Delta\omega_z}{\left(\Delta\omega_z - \Delta\omega_{\mathrm{peak}\,3}\right)^3}\right) \tag{E.6b}$$

$$d = 3\Gamma\frac{\Delta z}{\Delta t^2}\left(\frac{g_{\text{peak}\,2}}{\left(\Delta\omega_z - \Delta\omega_{\text{peak}\,2}\right)^2} - \frac{2\,g_{\text{peak}\,3}\,\Delta\omega_z}{\left(\Delta\omega_z - \Delta\omega_{\text{peak}\,3}\right)^3}\right) \tag{E.6c}$$

Fig. E.1 shows the gain dispersion created by the FIR filters (Eq. E.3) compared to the reference gain from Eq. E.4. Depending on the sampling interval, the FIR filter creates a periodicity in frequency do-

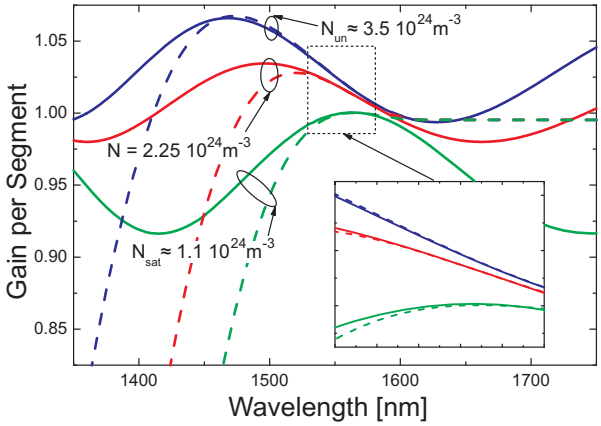


Figure E.1.: Wavelength dependent net gain of one segment of the UL-SOA for different carrier densities; solid lines - implementation with the FIR filters, dashed lines - reference gain according to Eq. 3.7; due to the first order FIR filter the spectral gain has a periodic shape and does not approximate well the reference gain model for $|\lambda - \lambda_0| > 30\,\text{nm}$; the inset shows the spectral gain of interest (70 nm around $\lambda_0$) where the FIR very well approximate the gain model

main. For a sampling interval of 25 fs, the periodicity has a spectral repetition rate of approximately 325 nm. For modelling applications, it is important that the gain approximation is accurate in a bandwidth of 30 nm around the reference wavelength. The inset of Fig. E.1 gives a detailed view on this bandwidth and an excellent match can be observed.

The gain suppressing effects from Eqs.2.14 have also to be included to the calculations of the filter coefficients. According to [33] also the wavelength dependence of SHB can be implemented:

$$a = 1 + \Delta z\left(\Gamma\Delta\omega_z^2\left(g_{\text{CH}} + g_{\text{FCA}} + g_{\text{TPA}} + \frac{3\,g_{\text{peak}\,2}}{\left(\Delta\omega_z - \Delta\omega_{\text{peak}\,2}\right)^2} - \frac{2\,g_{\text{peak}\,3}\,\Delta\omega_z}{\left(\Delta\omega_z - \Delta\omega_{\text{peak}\,3}\right)^3}\right)\left(1 + \frac{g_{\text{SHB}}}{g_{\text{peak}\,2}}\right) - \alpha_{\text{int}}\right) \tag{E.7a}$$

$$b = 3\Gamma\frac{\Delta z}{\Delta t}\Delta\omega_z\left(\frac{g_{\text{peak}\,2}}{\left(\Delta\omega_z - \Delta\omega_{\text{peak}\,2}\right)^2} - \frac{g_{\text{peak}\,3}\,\Delta\omega_z}{\left(\Delta\omega_z - \Delta\omega_{\text{peak}\,3}\right)^3}\right)\left(1 + \frac{g_{\text{SHB}}}{g_{\text{peak}\,2}}\right) \tag{E.7b}$$

$$d = 3\Gamma\frac{\Delta z}{\Delta t^2}\left(\frac{g_{\text{peak}\,2}}{\left(\Delta\omega_z - \Delta\omega_{\text{peak}\,2}\right)^2} - \frac{2\,g_{\text{peak}\,3}\,\Delta\omega_z}{\left(\Delta\omega_z - \Delta\omega_{\text{peak}\,3}\right)^3}\right)\left(1 + \frac{g_{\text{SHB}}}{g_{\text{peak}\,2}}\right) \tag{E.7c}$$

# F. Derivation of the Bogatov-like Effect

In this subsection, an analytic description of the Bogatov-like effect caused by the fast intraband effects in the UL-SOA's saturated section is derived.

The derivation of the Bogatov-like effect will be done in the style of [123] and [124]. For simplification, both input signals are assumed to be co-polarised CW signals (Eq. 3.10). To figure out how the two CW signals interact, the electric polarisation caused by the resonant nonlinearities has to be calculated with the help of $\chi_{\mathrm{NL}}$ (Eq. 2.22). For this reason, the rate equations of the fast intraband effects (Eqs. 2.14) have to be solved. In order to solve the differential equations, the last term of Eq. 2.14d) has to be excluded. This assumption can be made because the gain derivatives on the right-hand side are negligeable compared to the SHB's derivative due to bigger time constants. The simplified rate equations for the saturated section are:

$$\frac{\partial g_{\mathrm{CH}}}{\partial t} = -\frac{g_{\mathrm{CH}}}{\tau_{\mathrm{CH}}} - \frac{\epsilon_{\mathrm{CH}}}{\tau_{\mathrm{CH}}} g_{\mathrm{sat}} S \tag{F.1a}$$

$$\frac{\partial g_{\mathrm{FCA}}}{\partial t} = -\frac{g_{\mathrm{FCA}}}{\tau_{\mathrm{CH}}} - \frac{\epsilon_{\mathrm{FCA}}}{\tau_{\mathrm{CH}}} \frac{\mathrm{d}g}{\mathrm{d}N} N S \tag{F.1b}$$

$$\frac{\partial g_{\mathrm{SHB}}}{\partial t} = -\frac{g_{\mathrm{SHB}}}{\tau_{\mathrm{SHB}}} - \frac{\epsilon_{\mathrm{SHB}}}{\tau_{\mathrm{SHB}}} g_{\mathrm{sat}} S \tag{F.1c}$$

with $g_{\mathrm{sat}} = \frac{\alpha_{\mathrm{int}}}{\Gamma}$ (Eq. 3.9). Since the beating of the electric field is the reason for the Bogatov-like effect, only the dynamic term of Eq. 3.10 is of interest for the calculation of the nonlinear electric polarisation

$$\chi_{\mathrm{NL}} = \underbrace{\chi_{\mathrm{NL},0}}_{\text{static}} + \underbrace{\Delta\chi_{\mathrm{NL}}(\Omega)}_{\text{dynamic}} \qquad \text{and} \qquad P_{\mathrm{NL}} = \underbrace{P_{\mathrm{NL},0}}_{\text{static}} + \underbrace{\Delta P_{\mathrm{NL}}(\Omega)}_{\text{dynamic}} \tag{F.2}$$

Hence, the approach for solving the differential equations in Eqs. F.1 is:

$$\Delta g_{\mathrm{SHB}} = g'_{\mathrm{SHB}} \exp(i\Omega t) + c.c. \tag{F.3a}$$

$$\Delta g_{\mathrm{CH}} = g'_{\mathrm{CH}} \exp(i\Omega t) + c.c. \tag{F.3b}$$

$$\Delta g_{\mathrm{FCA}} = g'_{\mathrm{FCA}} \exp(i\Omega t) + c.c. \tag{F.3c}$$

Inserting Eqs. F.3 and the dynamic part of Eq. 3.10 into Eqs. F.1 leads to the solutions of the rate equations for the nonlinear gain due to the photon density pulsation:

$$\Delta g_{\mathrm{SHB}} = -g_{\mathrm{sat}}\, \epsilon_{\mathrm{SHB}} \frac{E_{\mathrm{pump}} E^*_{\mathrm{probe}}}{\kappa\left(i\,\tau_{\mathrm{SHB}}\Omega + 1\right)} \exp(i\Omega t) + c.c. \tag{F.4a}$$

$$\Delta g_{\mathrm{CH}} = -g_{\mathrm{sat}}\, \epsilon_{\mathrm{CH}} \frac{E_{\mathrm{pump}} E^*_{\mathrm{probe}}}{\kappa\left(i\,\tau_{\mathrm{CH}}\Omega + 1\right)} \exp(i\Omega t) + c.c. \tag{F.4b}$$

$$\Delta g_{\mathrm{FCA}} = -\frac{\mathrm{d}g}{\mathrm{d}N} N_{\mathrm{sat}}\, \epsilon_{\mathrm{FCA}} \frac{E_{\mathrm{pump}} E^*_{\mathrm{probe}}}{\kappa\left(i\,\tau_{\mathrm{CH}}\Omega + 1\right)} \exp(i\Omega t) + c.c. \tag{F.4c}$$

With help of these solutions and Eq. 2.21 the dynamic part of the nonlinear electric polarisation $\Delta P_{\mathrm{NL}}$ from Eq. F.2 can be obtained. For the electric field in Eq. 2.21 the superposition of the two signals has

to be taken ($E = E_{\text{pump}} \exp(i\omega_{\text{pump}} t) + E_{\text{probe}} \exp(i\omega_{\text{probe}} t) + c.c.$). When expanding the equation and only retaining terms which are either proportional to $\exp(\pm i\,\omega_{\text{pump}} t)$ or $\exp(\pm i\,\omega_{\text{probe}} t)$ the dynamic electric polarisation $\Delta P_{\text{NL}}$ due to the nonlinear gain and index pulsation can be obtained:

$$\begin{aligned}
\Delta P_{\text{NL}} = \varepsilon_0 \frac{c_0 n_{\text{G}}}{\omega} \Bigg\{ & - \Bigg[ \frac{(i-\alpha_{\text{SHB}})\, g_{\text{sat}}\, \epsilon_{\text{SHB}}}{1 - i\,\tau_{\text{SHB}}\Omega} + \frac{(i-\alpha_{\text{CH}})\, g_{\text{sat}}\, \epsilon_{\text{CH}}}{1 - i\,\tau_{\text{CH}}\Omega} \\
& + \frac{(i-\alpha_{\text{FCA}})\, \frac{\mathrm{d}g}{\mathrm{d}N} \epsilon_{\text{FCA}}\, N_{\text{sat}}}{1 - i\,\tau_{\text{CH}}\Omega} \Bigg] \frac{|E_{\text{pump}}|^2}{\kappa} E_{\text{probe}} \exp\left(i\omega_{\text{probe}} t\right) \\
& - \Bigg[ \frac{(i-\alpha_{\text{SHB}})\, g_{\text{sat}}\, \epsilon_{\text{SHB}}}{i\,\tau_{\text{SHB}}\Omega + 1} + \frac{(i-\alpha_{\text{CH}})\, g_{\text{sat}}\, \epsilon_{\text{CH}}}{i\,\tau_{\text{CH}}\Omega + 1} \\
& + \frac{(i-\alpha_{\text{FCA}})\, \frac{\mathrm{d}g}{\mathrm{d}N} \epsilon_{\text{FCA}}\, N_{\text{sat}}}{i\,\tau_{\text{CH}}\Omega + 1} \Bigg] \frac{|E_{\text{probe}}|^2}{\kappa} E_{\text{pump}} \exp\left(i\omega_{\text{pump}} t\right) \Bigg\} + c.c. \\
= \varepsilon_0 & \left( \Delta\chi_{\text{NL}}^{\text{probe}} E_{\text{probe}} \exp\left(i\omega_{\text{probe}} t\right) + \Delta\chi_{\text{NL}}^{\text{pump}} E_{\text{pump}} \exp\left(i\omega_{\text{pump}} t\right) \right) + c.c.
\end{aligned} \tag{F.5}$$

Since $|E_{\text{pump}}|^2 \gg |E_{\text{probe}}|^2$, only the first term in the braces of Eq. F.5 will be further investigated. Consequently only the influence of the dynamic nonlinear polarisation on the probe signal is considered. Hence, the effective probe gain due to the nonlinear polarisation is

$$\Delta g^{\text{probe}} = \frac{\omega}{c_0 n} \text{Im}\left(\Delta\chi_{\text{NL}}^{\text{probe}}\right) = \Delta g_{\text{SHB}}^{\text{probe}} + \Delta g_{\text{CH}}^{\text{probe}} + \Delta g_{\text{FCA}}^{\text{probe}} \tag{F.6}$$

where Im( ) denotes the imaginary part. Using Eq. F.6 and $\Delta\chi_{\text{NL}}^{\text{pump}}$ as defined in Eq. F.5, yields the probe signal's gain coefficients in Eq. 3.14 due to the various nonlinear gain and index gratings. Similar to the gain, the effective probe signal's phase due to the nonlinear polarisation can be calculated

$$\Delta\phi^{\text{probe}} = \frac{\omega}{c_0 n} \text{Re}\left(\Delta\chi_{\text{NL}}^{\text{probe}}\right) = \Delta\phi_{\text{SHB}}^{\text{probe}} + \Delta\phi_{\text{CH}}^{\text{probe}} + \Delta\phi_{\text{FCA}}^{\text{probe}} \tag{F.7}$$

where Re( ) denotes the real part. As a result, the probe signal's phase coefficients in Eq. 3.16 can be obtained.

# G. Generation of Critical Bit Sequences

To investigate the impact of bit pattern effects on the presented scheme, critical bit sequences are used because of lower computational effort compared to true PRBSs. Fig. G.1 shows the flowchart how these critical bit sequences are created. As an example the 4th order critical bit sequence is: *000010001010000111101110101111*.

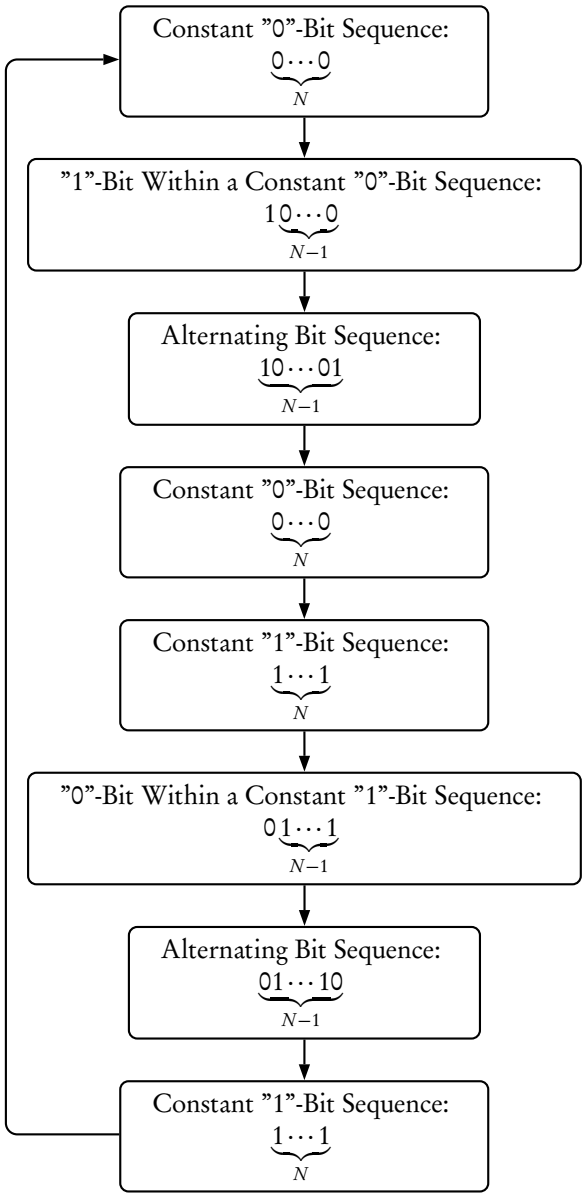


Figure G.1.: Flowchart for generating a critical bit sequence of the N*th* PRBS order; the generation rule can be applied for even PRBS orders; for odd PRBS orders the alternating bit sequences have to be extended or shortened by one bit in order to avoid bit subsequences of the same consecutive bits longer than the PRBS order

For the simulation in this thesis, the flowchart has run through until sequences of different PRBS orders had a length of 263 bits.

# H. Author's Publications

## Journals & Letters

P. Runge, C.-A. Bunge and K. Petermann, "All-Optical Wavelength Conversion with Extinction Ratio Improvement of 100 Gb/s RZ-Signals in Ultralong Bulk Semiconductor Optical Amplifiers", *IEEE J. Quantum Electron.*, Vol. 46, No. 6, pp. 937-944, 2010

P. Runge, R. Elschner and K. Petermann, "Chromatic Dispersion in InGaAsP Semiconductor Optical Amplifiers", *IEEE J. Quantum Electron.*, Vol. 46, No. 5, pp. 644-649, 2010

P. Runge, C.-A. Bunge, K. Petermann, W. Brinker, M. Schlak and B. Sartorius, "Widely Tuneable Short Pulse Generation with Ultralong Semiconductor Optical Amplifiers", *IEEE J. Lightwave Technol.*, Vol. 28, No. 5, pp. 754-760, 2010

P. Runge, R. Elschner and K. Petermann, "Time-Domain Modelling of Ultralong Semiconductor Optical Amplifiers", *IEEE J. Quantum Electron.*, Vol. 46, No. 4, pp. 484-491, 2010

P. Runge, R. Elschner, C.-A. Bunge and K. Petermann, "Extinction Ratio Improvement in Ultralong Semiconductor Optical Amplifiers", *IEEE J. Quantum Electron.*, Vol. 45, No. 6, pp. 578-585, 2009

P. Runge, R. Elschner, C.-A. Bunge, K. Petermann, M. Schlak, W. Brinker and B. Sartorius, "Operational Conditions for the Extinction Ratio Improvement in Ultralong SOAs", *IEEE Photon. Technol. Lett.*, Vol. 21, No. 2, pp. 106-108, 2009

## Conferences & Workshops

P. Runge, K. Petermann, W. Brinker, M. Schlak and B. Sartorius, "Supercontinuum Generation in Ultralong SOAs – Theory and Experiment", *Proc. European Conference on Optical Communication (ECOC 2009)*, paper 6.2.4, Vienna, Austria, 2009

P. Runge, R. Elschner and K. Petermann, "Optimising Four-Wave Mixing in Ultralong SOAs", *Proc. Numerical Simulation of Optoelectronic Devices (NUSOD 2009)*, paper TuB2, Gwangju, South Korea, 2009

P. Runge, C.-A. Bunge and K. Petermann, "All-Optical Wavelength Conversion with Extinction Ratio Improvement of 100Gb/s RZ-Signals in Ultralong Bulk SOAs", *Proc. Photonics in Switching (PS 2009)*, paper PT7, Pisa, Italy, 2009

P. Runge and K. Petermann, "Supercontinuum Generation in Ultralong Semiconductor Optical Amplifiers", *Nonlinear Optics in Guided Geometries (WIAS)*, Berlin, Germany, 2009 (invited talk)

P. Runge and K. Petermann, "All-Optical Signal Processing with Ultralong Bulk Semiconductor Optical Amplifiers for Data Rates above 100 Gb/s", *Proc. Conference on Lasers and Electro-Optics (CLEO Europe*

*2009)*, paper CD9.2, München, Germany, 2009

C.-A. Bunge, R. Elschner, P. Runge and K. Petermann, "All-optical wavelength conversion of D(Q)PSK signals in transparent optical networks", *Proc. 9th International Conference on Transparent Optical Networks (ICTON 2008)*, Vol. 1, pp. 117-120 , Athens, Greece, June 2008 (invited paper)

P. Runge, R. Elschner, C.-A. Bunge, K. Petermann, M. Schlak, W. Brinker, B. Sartorius and M. Schell, "Extinction Ratio Improvement in Ultralong Semiconductor Optical Amplifiers – Two Wave Competition for Regenerative Applications", *Proc. Photonics in Switching (PS 2008)*, paper D-05-3, Hokkaido, Japan, 2008

P. Runge, R. Elschner, C.-A. Bunge and K. Petermann, "Extinction Ratio Improvement due to a Bogatov-like Effect in Ultralong Semiconductor Optical Amplifiers", *COST 288 Summer School*, Cetraro, Italy, 2008

A. Kilian, R. Hauffe, M. Winter, P. Runge, J. Kuhmann, C.G. Greisen, S. Weichel, L. Shiv and M. Heschel, "Silicon micro-machined hermetic packaging technology for optical subassemblies", *Annual Meeting of the IEEE Lasers and Electro-Optics Society (LEOS)*, paper MJ4, Montreal, Canada, 2006

M. Winter, R. Hauffe, A. Kilian, P. Runge, D. Reznik, C.G. Greisen, S. Weichel, L. Shiv and M. Heschel, "Application and RF performance of integrated resistor structures on non-planar topologies in micro-machined silicon packages for transmitter optical subassemblies", *Proc. Electronic Components and Technology Conference (ECTC 2006)*, pp. 1560-1566, San Diego, CA, 2006

# I. Acknowledgements

First of all, I would like to thank Prof. Petermann for giving me the opportunity to do my Ph.D. thesis under his supervision at his institute. He gave me tremendous scientific freedom and provided continuous technical and administrative support throughout the years. I would also like to acknowledge my other supervisor Prof. Bunge for teaching me to work in an academic way and motivating me to publish my results. For the good teamwork I would like to thank our project partners, namely the group of Dr. Sartorius from the Fraunhofer Institute for Telecommunications – Heinrich Hertz Institute. Especially, from this group, I would like to thank Walter Brinker for supporting my theories with experiments. For the project funding I would like to thank the Deutsche Forschungsgemeinschaft (DFG).

Furthermore, I would like to acknowledge my colleague Robert Elschner for the good introduction to the topic of SOAs and the fruitful discussions within the first year leading to multiple publications. Also, I would like to thank my colleague Christian Weber for the discussion about optical communication systems during lunch leading to interesting thoughts for applications of UL-SOAs.

I like to acknowledge Xin-ru Wang for proof-reading my thesis and helping me with my english.

Last but not least, I would like to thank my parents for supporting me while doing my Ph.D. degree, especially my mother for pushing me since elementary school to get a high level education.